To

Zheng, Yitong, Yiqian and My Parents

Theoretical Study of the Coherent Brillouin Scattering Based Fiber Sensor

by
Yidun Wan

Thesis submitted to the
Faculty of Graduate and Postdoctoral Studies
In partial fulfilment of the Requirements
For the MSc degree in physics

Department of Physics
Faculty of Science
University of Ottawa

Road to Unification

This work contains no material which has been accepted for the award of any other degree or diploma in any University or other tertiary institution and, to the best of my knowledge and belief, contains no material previously published or written by another person, except where due reference has been made in the text.

I give consent to this copy of my thesis, when deposited in the University Library, being available for loan and photocopying.

SIGNED: .....

DATE: .....

Supervisors: Prof. Xiaoyi Bao and Prof. Liang Chen

Acknowledgments

It is my pleasure to take this opportunity to thank all the people who have supported and influenced this Master of Science.

First of all, I specially thank my supervisors, Prof. Xiaoyi Bao and Liang Chen for providing me such an opportunity in doing research in fiber optics. Their critical and thoughtful approach towards problems was always instructive. I owe them for lots of delicate points that they taught me. Their care about me was beyond their roles as supervisors and I will never forget.

I like to thank Zheng, my wife. No words can describe my feelings, gratitude and appreciation to her. Her continual love, support, encouragement, bearing, tolerance and patience made this work possible. She was with me whenever I got confused, lost and disappointed. I would like to express my hearty appreciation to Zheng. What she has sacrificed and contributed during these years is invaluable.

My gratefulness also goes to my family in China, especially my parents for their endless support, encouragement and consideration even when I decided to switch to physics from computer science which was hot in the job market. I also thank my son, who is to be born in this August, since he brought a lot of happiness and hope.

Many thanks to my friend and colleague Dr. Lufan Zou for his invaluable discussion and help within and beyond my research and study. Lots of thanks to my friend and colleague Dr. Shahraam Afshar for his priceless advice and help in my theoretical research work. Special thanks to my friend and colleague Ou Chen who was always there to help me and for his cooperation in building the 1550-sensor. My appreciation also goes to my friend and colleague Dr. Shiquan Yang for his discussion with me about many related problems. I enjoyed working and discussing with them.

Thanks to the rest of the optics group who made the optics group a very pleasant and interesting place to work.

I like to appreciate with all my heart Prof. Richard Hodgson, Prof. Robin Williams and Prof. John Armitage for their detailed comments and corrections.

Thanks to NSERC and ISIS Canada for their support.

I also need to thank the members of the Physics Department for their support.

Abstract

This Thesis includes theoretical and experimental studies on the distributed fiber-optic sensor based on Brillouin loss. A numerical method (introduced by Chu *et al.*[1]) to solve the 3 coupled wave equations for Brillouin scattering in the transient regime is adopted to simulate our sensing system (based on two 1310 nm Nd:YAG lasers). Sub-peaks in the Brillouin spectra are found to be caused by: 1) off-resonance oscillation (at frequency $|\nu - \nu_B|$), i.e. the temporal damping oscillation of the cw pump intensity when the beat frequency ν of the cw pump and pulsed probe beams does not match the local Brillouin frequency ν_B; and 2) convolution of the gain profile and the Fourier spectrum of the pulsed probe. Features of the sub-peaks are discussed. Such effects can be eliminated by subtracting the reference Brillouin spectrum (obtained for loose fiber and reference temperature) from the one including variable strain/temperature information.

A new model of the pulsed probe field, which is the output optical field of the electro-optic modulator (EOM), is introduced. This model includes a time-dependent phase for the pulsed probe field and a combination of phase modulation (PM) and amplitude modulation (AM) due to imperfectly balanced field amplitudes and a voltage induced phase in the two modulation arms of the EOM. With this model, the calculated Brillouin spectra match well with the experimental spectra. This provides theoretical support for centimeter spatial resolution, narrow spectrum bandwidth (˜50MHz) and high SNR (˜37dB) of our 1310nm sensor system. Two other effects of the combination of PM and AM are also predicted: the asymmetric Brillouin spectrum and main Brillouin frequency shift.

List of Figures

Contents

Chapter 1

Introduction

Over the past decades, fiber optic sensors have been developed and widely applied to health monitoring in various civil structures like pipe lines, bridges and nuclear reactors. These sensors are mainly based on the following fiber optic effects: fiber Bragg grating[4, 5, 6, 7], Stimulated Raman Scattering (SRS)[8] and Stimulated Brillouin Scattering (SBS)[9, 10, 11, 12]. Although Bragg grating based sensors have very high strain and temperature resolution ($< 1\mu\varepsilon$[13] and 0.4 °C[14] respectively) they are in practice not distributed. Sensors based on SRS employ a technique called optical time-domain reflectometry (OTDR)[15]. Among those sensors based on Brillouin scattering, some use only one laser source[12, 16] while others utilize a technique called Brillouin optical-fiber time domain analysis (BOTDA) in which two counter-propagating lasers, one pulsed and one cw laser, are used to amplify the Brillouin gain/loss effects of the cw pump beam inside the fiber. The former type is limited in applications due to its non-distributed nature and lack of long-range sensing capability. The latter type, based on BOTDA, which originated from a common distributed sensing technique named optical time-domain reflectometry (OTDR)[15], was first introduced by Horiguchi *et al.*[9] and then extensively improved by Kurashima *et al.*[10, 17], and Bao *et al.*[11, 18, 19].

SBS is a 3rd order inelastic nonlinear effect in the optical fields exchange part of their energy with the dielectrics. In a simple quantum picture, the annihilation of a photon of the injected field (normally called the pump) generates a photon at the downshifted Stokes frequency and a phonon with the proper energy and momentum to conserve the total energy and momentum.

On the other hand, a so-called anti-Stokes photon at higher energy can be created as well upon the absorption of a phonon with proper energy and momentum. In a classical picture, SBS is a parametric process between the pump and Stokes through an acoustic wave induced by electrostriction due to the existence of electrical fields. The acoustic wave results in a periodic modulation of the refractive index of the dielectric. This refractive index grating scatters the pump wave through Bragg diffraction Since the index varies with time and position, the scattered light experiences a Doppler frequency shift with a magnitude of the acoustic frequency. According to the conservation of total energy and momentum, the Stokes/anti-Stokes wave is found to be back scattered from the incident light wave. The difference between the frequencies of the incident light and the scattered light is called the Brillouin frequency ν_B, which is found to be linear with the temperature and strain over a wide range along optical fibers. This linearity qualifies the Brillouin scattering to be a powerful distributed fiber sensing technique for strain/temperature measurements.

This thesis focuses on contributions to an ongoing research project on distributed Brillouin based fiber sensing at the University of Ottawa. The project was started by Bao *et al.* at the University of New Brunswick and then continued at the University of Ottawa, is to study, apply and improve a distributed fiber-optic Brillouin sensor based on two 1310 nm Nd: YAG lasers (1310-sensor). The 1310-sensor has been applied to various field tests. With this sensor, the highest spatial resolution (order of centimeter) in the world for distributed strain/temperature sensing has been achieved[20].

This thesis includes a theoretical study of distributed fiber Brillouin sensing. Due to the non-uniform strain/temperature distributed along fibers under test, multi-peak Brillouin spectra can be observed. These multi-peak Brillouin spectra contain the real strain/temperature distribution along sensing fibers. However, in the experimental results from the 1310-sensor, a type of peaks, namely sub-peaks, appear in the Brillouin spectra[2] even when sensing fibers are under uniform strain/temperature. Therefore, it is quite practical and important, especially in distributed fiber sensing, to clarify the origins of those sub-peaks so that they can be distinguished from those peaks caused by nonuniform strain or temperature distribution. This thesis presents two origins of the sub-peaks: one is the Fourier spectrum of the pulse; the other is temporal off-resonance oscillation, which is a phenomenon newly predicted by us,

denoting the periodic damping oscillation of the cw pump intensity in the time domain when the beat frequency ν of the two counter-propagating laser beams does not match the Brillouin frequency ν_B of the sensing fiber, i.e. off-resonance. This off-resonance oscillation, with a frequency identical to $|\nu - \nu_B|$, is the dominating reason for generation of the sub-peaks. Since pulse widths normally used for the sensor are around 1.5 ns, the sub-peaks due to the Fourier spectrum of the pulse are far from the central Brillouin peak so that they are not recognizable in experimental frequency windows. However, the two origins compete with each other, so that when using wider pulses (> 3 ns), effecting due to the Fourier spectrum become more dominant than the off-resonance oscillation. Features of the sub-peaks are described in this thesis.

The centimeter spatial resolution with Brillouin spectrum linewidths (˜50MHz) and high SNR (˜37dB) achieved by our research group[20, 21] is much better than those (1 meter, hundreds of MHz linewidth) claimed by others[22, 23]. Nevertheless, little theoretical work has been done on the Brillouin loss/gain spectrum shape and line width at the centimeter spatial resolution and no prediction exists for the minimum detectable strain/temperature length. In this context, we have derived a general model of the output field of the electro-optic modulator (EOM), which introduces the phase modulation (PM) to account for the power and phase imbalance between two arms of the EOM. Using this new model, we have obtained simulation results matching our experiments. The power ratio between the two arms of the interferometer is 1 for the ideal amplitude modulation (AM). However such a ratio is in practice between 0.95-0.98 due to power imbalance. As a result, we have combined AM and PM. Due to this feature, the Brillouin loss spectrum has a Lorentzian dominated shape, and is not significantly changed between the Gaussian and super Gaussian pulses. The broad background is suppressed for increased sensing lengths. This feature is important in detecting multiple Brillouin peaks with low power density due to the short stress/temperature length (<spatial resolution). Therefore, the minimum detectable stress/temperature length can be reduced to 1/3 of the spatial resolution, i.e. 3cm strain length for 1ns pulse widths. In addition, two other effects of the optical phase are described; the asymmetric Brillouin spectra and resonance frequency shift due to the residual phase caused by power and phase imbalance between the two modulation arms of the EOM.

Chapter 2 introduces the principles of SBS and fiber sensing based on Brillouin gain/loss,

and presents theoretical models of distributed Brillouin fiber-optic sensors. Chapter 3 not only illustrates the working principles of the 1310-sensor and several optical components critical to the sensing system but also derives the new model of the output field of the EOM. Chapter 4 describes numerical solutions of the 3-wave coupling model of SBS and discusses key points of the simulation based on these numerical solutions. Chapter 5 discusses the origins of the sub-peaks in Brillouin spectra from the distributed Brillouin sensors and fully characterizes them. Chapter 6 focuses on the impact of the optical phase on the Brillouin spectra. Chapter 7 concludes all the work we have done and presents some possible future directions.

Chapter 2

Principles of Stimulated Brillouin Scattering

Stimulated Brillouin Scattering, as a nonlinear effect in optical fibers, has been widely studied since 1964 when it was first observed. Although it is harmful to communication systems based on optical fibers, it was found to be a very successful mechanism on which to base a kind of fiber-optic sensor for health monitoring[9, 24, 25] and as such it has been intensively developed in the past decade[9, 10, 11, 18, 19, 20, 22, 23, 26]. The distributed fiber-optic sensor we are currently using is based on Brillouin loss and was developed by Bao *et al.*[11]. In this chapter, we introduce SBS by starting with a brief review of nonlinear optical effects. This is followed by a sketch of the working principles of our sensing system. Next we give a description of the related mathematical models. Finally, an explanation of Brillouin Optical Time Domain Analysis (BOTDA) and a description of the related mathematical models are given.

2.1 Inelastic nonlinear process

As is well known, the two inelastic scattering processes, SBS and Stimulated Raman Scattering (SRS), are important nonlinear effects in optical fibers. They are inelastic in that the optical fields exchange part of their energy with the dielectrics. Nonlinear effects in dielectrics such as optical fibers, originate from the anharmonic oscillation of bound electrons under the influence

of high intensity electromagnetic fields. As a consequence, the electric polarization vector $\vec{P}$ of the electric dipoles is nonlinearly related to the electric field $\vec{E}$ as described by[27]

$$\vec{P} = \epsilon_0 \left(\chi^{(1)} \cdot \vec{E} + \chi^{(2)} \cdot \vec{E}\vec{E} + \chi^{(3)} \cdot \vec{E}\vec{E}\vec{E} + \cdots \right), \tag{2.1}$$

where ϵ_0 is the vacuum permittivity and $\chi^{(j)}$ is a tensor of $(j+1)$th order representing the jth order electric susceptibility. The linear susceptibility $\chi^{(1)}$ is the main contribution to $\vec{P}$. Silica fibers have an inversion symmetry of molecular structure, so normally the second order nonlinear effect is zero. Hence, the lowest order nonlinear effects in silica fibers are represented by $\chi^{(3)}$ and in more detail are actually caused by the imaginary part of $\chi^{(3)}$, since it is associated with nonlinear gain/loss[28, 29]. Therefore, SBS and SRS are both 3rd order nonlinear effects related to the excited vibrational states of the silica. A simple quantum mechanical picture is suitable for both effects; the annihilation of a photon of the injected field (normally called the pump) generates a photon with the downshifted Stokes frequency and a phonon with proper energy and momentum to satisfy the total energy and momentum conservation. On the other hand, a so-called anti-Stokes photon at higher energy can be created as well upon the absorption of a phonon with proper energy and momentum. The fundamental distinction between these two effects is that SRS involves optical phonons, whereas SBS involves acoustic phonons. This leads to more detailed differences: SRS in optical fibers can produce both forward and backward Stokes waves but SBS produces only the backward one; the Stokes frequency shift in SBS (around 12 GHz) is lower than that in SRS (about 13 THz).

2.2 Stimulated Brillouin Scattering

SBS can be equivalently viewed classically as a parametric process between the pump and Stokes fields. Through electrostriction, the pump wave induces an acoustic wave[30] inside the fiber which results in a periodic modulation of the refractive index of the dielectric. This refractive index grating scatters the pump wave through Bragg diffraction. The index varies with time and position and the scattered light experiences a Doppler frequency shift with a magnitude of the acoustic frequency. The total energy and momentum during the whole process must be

conserved, so in a general case, applicable to both Stokes and anti-Stokes interaction, we have

$$E_p = E_S \pm E_a, \qquad \vec{p}_p = \vec{p}_S \pm \vec{p}_a, \tag{2.2}$$

where the subscripts p, S and a represent the pump, Stokes/anti-Stokes and acoustic waves respectively; the plus and minus signs are used respectively in Stokes and anti-Stokes processes. Knowing that $E = \hbar\omega$ and $\vec{p} = \hbar\vec{k}$ where ω and $\vec{k}$ denote the angular frequency and wave vectors respectively, Eq. (2.2) can be simply written as

$$\omega_p = \omega_S \pm \omega_a, \qquad \vec{k}_p = \vec{k}_S \pm \vec{k}_a. \tag{2.3}$$

Moving $\vec{k}_S$ in Eq. (2.3) to the left hand side and taking the inner product of both sides of the equation yields

$$\begin{aligned} k_p^2 + k_S^2 - 2k_p k_S \cos\theta_{p,S} &= k_a^2 \\ \Rightarrow k_p^2 + k_S^2 - 2k_p k_S + 4k_p k_S \sin^2\frac{\theta_{p,S}}{2} &= k_a^2 \end{aligned} \tag{2.4}$$

where $\theta_{p,S}$ denotes the angle between $\vec{k}_p$ and $\vec{k}_S$. The relation among wave velocity, angular frequency and wave vector is $\omega = vk$ for acoustic phonons, which characterizes the proportionality between the angular frequency and wave number. Since $\omega_a \ll \omega_p, \omega_S$, we can take the approximation of $k_p \approx k_S$ so that together with $\omega_a = v_a k_a$ where v_a is the sound velocity, Eq. (2.4) becomes

$$\begin{aligned} 4k_p k_S \sin^2\frac{\theta_{p,S}}{2} &= k_a^2 \\ \Rightarrow 4k_p^2 v_a^2 \sin^2\frac{\theta_{p,S}}{2} &= \omega_a^2 \\ \Rightarrow \frac{2nv_a}{\lambda_p}\sin\frac{\theta_{p,S}}{2} &= \nu_a \end{aligned} \tag{2.5}$$

where the common relation $\frac{\omega_P}{c} = \frac{2\pi}{\lambda_p}$ (λ_p is the wavelength of the pump), $\omega_a = 2\pi\nu_a$ (ν_a is the sound frequency) and the light velocity in fiber $\frac{c}{n}$ are applied to get the last step in the above equation. Eq. (2.5) tells us that the maximum frequency shift (i.e. ν_a) happens where $\theta_{p,S} = \pi$,

which means that the scattered light is in the opposite direction to the injected pump. The maximum frequency shift, which is named the Brillouin frequency ν_B after L. Brillouin, is then naturally defined as

$$\nu_B = \frac{2nv_a}{\lambda_p}. \tag{2.6}$$

Fibers with different dopants in their cores have different Brillouin frequencies. A typical value of ν_B is about 12800 MHz for a silica fiber at room temperature, $\lambda_p = 1310$ nm, $n = 1.4675$ and $v_a = 5750$ m/s[31, 32]. This Brillouin frequency was found to be linear with strain[9] and temperature[17] over a wide range, as specified in the following equations[23]:

$$\begin{aligned} \nu_B(\varepsilon) &= \nu_B(0) + C_\varepsilon \varepsilon \\ \nu_B(T) &= \nu_B(T_r) + C_T(T - T_r), \end{aligned} \tag{2.7a}$$

where ε, T and T_r denote the longitudinal strain along the fiber, temperature and reference temperature respectively. C_ε, C_T are two coefficients depending on the medium properties. Although the strain coefficient does not change significantly with strain[24] and the temperature coefficient is also believed not to change significantly with temperature[23], the determination of these two coefficients through appropriate laboratory temperature and strain calibrations is suggested. This linearity appears naturally as a powerful sensing mechanism for strain and temperature detection[9, 33]. By measuring the Brillouin frequency shift $\Delta\nu_B$, the corresponding strain/temperature change can be obtained through Eqs. (2.7).

The threshold pump power for SBS is found by Smith[34] to be:

$$P_{th} = \frac{21 A_{eff}}{g_B L_{eff}} \left(1 + \frac{\Delta\nu_{\text{fwhm}}}{(\Delta\nu_B)_{\text{fwhm}}}\right),$$

where A_{eff} and L_{eff} $(= \left(1 + e^{-\alpha L}\right)/\alpha$ for cw beam and $= c\tau_p/2n$ for pulse), in which α is the fiber loss and L is the fiber length, are respectively the effective core area and effective length; g_B is the peak gain coefficient; $\Delta\nu_{\text{fwhm}}$ is the laser bandwidth and $(\Delta\nu_B)_{\text{fwhm}}$ is the Brillouin gain bandwidth. Since normally $\Delta\nu_{\text{fwhm}} \ll (\Delta\nu_B)_{\text{fwhm}}$, $\Delta\nu_{\text{fwhm}}/(\Delta\nu_B)_{\text{fwhm}}$ can be neglected

so that the above equation becomes $P_{th} \approx 21 A_{eff}/g_B L_{eff}$[35]. When the incident intensity is lower than the SBS threshold power, spontaneous Brillouin scattering, which results from the scattering of the incident light by lattice thermal vibrations, can also happen.

2.3 Brillouin Optical Time Domain Analysis (BOTDA) based on Brillouin loss amplification

From the last section, we know that SBS appears to be a possible fiber sensing technique. Nevertheless, such a fiber sensor, based on SBS, is undesirable for long range since when SBS happens (provided that the incident power is above the SBS threshold), almost 100% of the incident light beam is scattered into the backward Stokes beam over a short interaction length so that the SBS effect cannot continue over a long distances. Therefore, the power of the incident laser must be lower than the SBS threshold[34]. But then, how could a sensor utilizing the Brillouin process be realized? Fortunately, a technique (namely Brillouin loss amplification)[36] which can amplify the Brillouin effect in optical fibers is achieved by using two counter-propagating laser beams with powers below the SBS threshold. Consider two laser beams at frequencies with a slight difference (˜12 GHz), namely ν_p and ν_s, counter-propagating in an optical fiber. Due to the electrostriction they will generate a mechanical wave effect with a beat frequency $|\nu_p - \nu_s|$ denoting the slow modulation of the optical amplitudes. This composite electromagnetic field varying at frequency $|\nu_p - \nu_s|$ induces an acoustic field at the same frequency through the effect of electrostriction. If we view this beat laser field as a kind of driving force for the acoustic field, then it follows that when $|\nu_p - \nu_s| = \nu_B$, which is the Brillouin frequency of the fiber, this interaction is at the so-called resonant state, in which energy loss from the pump is at a maximum. Because it is the acoustic phonon which is involved in the whole process, the loss in the pump beam intensity is called Brillouin loss. This Brillouin loss is enhanced by the existence of the probe beam via their beat amplitude. Based on this procedure, a technique for distributed sensing called Brillouin Optical Time Domain Analysis (BOTDA) was developed by Horiguchi *et al.*[9]. A laser is placed on each end of the sensing fiber. One emits a pulsed light (call it a probe or Stokes light at frequency ν_s)

launching at $z = 0$ while the other emits a cw light (call it pump light at frequency $\nu_p > \nu_s$) incident at the opposite end $z = L$. The probe and pump counter-propagate inside the sensing fiber and interact through Brillouin loss amplification, which results in an amplification of the pulse but a depletion in the cw pump wave. The depleted cw pump is detected at $z = 0$. The cw light, which is depleted at some spatial position z due to the interaction with the pulse, arrives at $z = 0$ at time $t = 2z/v_g$ where $t = 0$ is identified when the pulse is injected. v_g is the group velocity of light in the fiber. Therefore, the depleted cw pump carries distributed interaction information along the whole fiber length L over a time period $2L/v_g$. The spatial resolution immediately follows as $\delta z = \tau_p v_g/2$ where τ_p is the pulse width. If the beat frequency $\nu = \nu_p - \nu_s$ of the two lasers is scanned within some range of frequencies, one can obtain the so-called Brillouin spectrum at some time t. This Brillouin spectrum contains interaction information at $z = tv_g/2$. Since when $\nu = \nu_B(z)$, which is the Brillouin frequency at position z, the interaction is at resonance which means a maximum depletion in the cw pump intensity, a peak, hereafter called the Brillouin peak, appears in the corresponding Brillouin spectrum. By measuring the shift of this peak, $\Delta\nu_B$, which is actually the Brillouin frequency shift from the value of ν_B at a reference temperature or zero strain, one can determine the temperature or strain change at this position of the fiber according to the linear relations in Eqs. (2.7).

Our current sensor developed by Bao *et al.* is based on BOTDA but with many practical concerns and new developments. This sensor will be described in Section 3.1.

2.4 Theoretical model of Brillouin based fiber sensing

In Brillouin-based fiber sensor, two counter-propagating photon fields are coupled with an induced acoustic phonon field. An understanding of the time-dependent evolution of these three fields is very important for a better understanding of the sensing process. By starting with Maxwell's equations and by considering the material density variation due to the applied electric fields, a theoretical model of the effect has been obtained[37, 38]. This model is established in the case of resonance, as mentioned in the last section. A model considering a varying beat frequency of the pump and Stokes waves was introduced by Chow *et al.*[39] and then discussed by Lecoeuche *et al.*[40] and Rae *et al.*[41]. The most general model which also includes GVD

(group velocity dispersion), SPM (self phase modulation) and XPM (cross phase modulation) is summarized in *Nonlinear Fiber Optics* by Agrawal[27].

2.4.1 3-Wave equations

Since the pulse width of the pulsed Stokes wave is of the order of a nanosecond, and the spectral width is correspondingly small, GVD effects are negligible. In addition, SPM and XPM can also be neglected because the peak power of the pulsed Stokes wave is relatively low[27] (˜50 mW for our sensor). With these assumptions, a practical model of SBS can be summarized by the following 3-wave coupled PDE's:

$$\left(\frac{\partial}{\partial z} - \frac{n}{c}\frac{\partial}{\partial t}\right) E_p = \mathrm{i}g_1 Q E_s + \frac{1}{2}\alpha E_p \tag{2.8a}$$

$$\left(\frac{\partial}{\partial z} + \frac{n}{c}\frac{\partial}{\partial t}\right) E_s = -\mathrm{i}g_1 Q^* E_p - \frac{1}{2}\alpha E_s \tag{2.8b}$$

$$\left(\frac{\partial}{\partial t} + \Gamma\right) Q = -\mathrm{i}g_2 E_p E_s^* \tag{2.8c}$$

where E_p, E_s and Q denote the fields of the cw pump, pulsed Stokes and sound respectively, g_1 and g_2 are the photon-phonon coupling coefficients[38, 42] and α is the attenuation factor of the fiber. By letting $\mathrm{i}g_1 Q = \bar{Q}$, then $-\mathrm{i}g_1 Q^* = \bar{Q}^*$, multiplying both sides of Eq. (2.8c) by $\mathrm{i}g_1$ and recognizing that $\frac{n}{c} = \frac{1}{v_g}$, we get a more compact form:

$$\left(\frac{\partial}{\partial z} - \frac{1}{v_g}\frac{\partial}{\partial t} - \frac{1}{2}\alpha\right) E_p = \bar{Q} E_s \tag{2.9a}$$

$$\left(\frac{\partial}{\partial z} + \frac{1}{v_g}\frac{\partial}{\partial t} + \frac{1}{2}\alpha\right) E_s = \bar{Q}^* E_p \tag{2.9b}$$

$$\left(\frac{\partial}{\partial t} + \Gamma\right) \bar{Q} = \frac{1}{2}\Gamma_1 g_B E_p E_s^*, \tag{2.9c}$$

where $g_B = \frac{2g_1 g_2}{\Gamma_1}$ is the Brillouin gain factor. Here $\Gamma = \Gamma_1 + \mathrm{i}\Gamma_2$ with $\Gamma_1 = \frac{1}{2\tau}$ which is the damping rate with the phonon life time $\tau \sim 10$ ns for silica fibres, $\Gamma_2 = 2\pi(\nu - \nu_B) = \omega - \omega_B$ which denotes the detuning frequency in which ν is the beat frequency being scanned. In our sensor, the pulse width of the pulsed Stokes wave is normally less than the phonon lifetime,

which defines the transient regime. Thus Eqs. (2.9) are very applicable to the case of fiber sensing. They will be solved in Chapter 4 for the simulation of our distributed Brillouin sensor. Closed form analytical solutions of Eqs. (2.9) do not exist.

2.4.2 Steady state equations

When considering the case of a steady state, where the intensities I_p and I_s are time independent, and assuming the cw pump and pulsed stokes waves are polarized in the same direction, two coupled steady state equations can be obtained. In so doing, by discarding the $\partial/\partial t$ terms in Eqs. (2.9), substituting for $\bar{Q}$ from Eq. (2.9c) into Eqs. (2.9a and 2.9b), and after some manipulation, one obtains the so-called steady-state equations

$$\frac{\mathtt{d}}{\mathtt{d}z} I_p = g_B(\nu) I_p I_s + \alpha I_p \tag{2.10a}$$

$$\frac{\mathtt{d}}{\mathtt{d}z} I_s = g_B(\nu) I_p I_s - \alpha I_s, \tag{2.10b}$$

where $g_B(\nu) = \frac{\Gamma_1^2}{\Gamma_1^2+\Gamma_2^2} g_B$ which shows that the Brillouin spectrum has a Lorentzian profile. These two equations have been solved analytically by Chen *et al.*[43]. If the attenuation is neglected, Eqs. (2.10) become

$$\frac{\mathtt{d}}{\mathtt{d}z}(I_p - I_s) = 0$$

which ensures the constancy of $I_p - I_s$.

Chapter 3

Distributed fiber-optic Brillouin sensor based on two 1310 nm Nd:YAG lasers

In this chapter we first introduce the working principles of the distributed fiber-optic Brillouin sensor based on two 1310 nm Nd:YAG lasers, then we briefly discuss the mechanism of the Electro-optic modulator (EOM) which modulates the probe laser beam into a pulsed optical signal. We describe the modulation procedure and derive its output laser field and extinction ratio in detail. Lastly, we will talk about the optical isolator and circulator, since they are important in stabilizing the sensing system and data collecting.

3.1 Sensor setup and working principles

As shown in Fig. 3.1[2], the distributed Brillouin sensor currently employed in our lab, which was developed by Bao *et al*, is based on two 1310 nm Nd:YAG lasers designated as 'probe' and 'pump'. The pump and probe laser beams counter-propagate in the sensing system. Because Brillouin scattering is a polarization-dependent effect, when using polarization maintaining fibers the polarization state can be maintained for a long distance provided that the initial polarization is oriented along the fast or slow axis of the fiber, when using single mode fibres, the polarization states are random along the fiber (due to the random fluctuations of the fiber birefringence caused by the fluctuations in the core shape and the nonuniform stress acting on

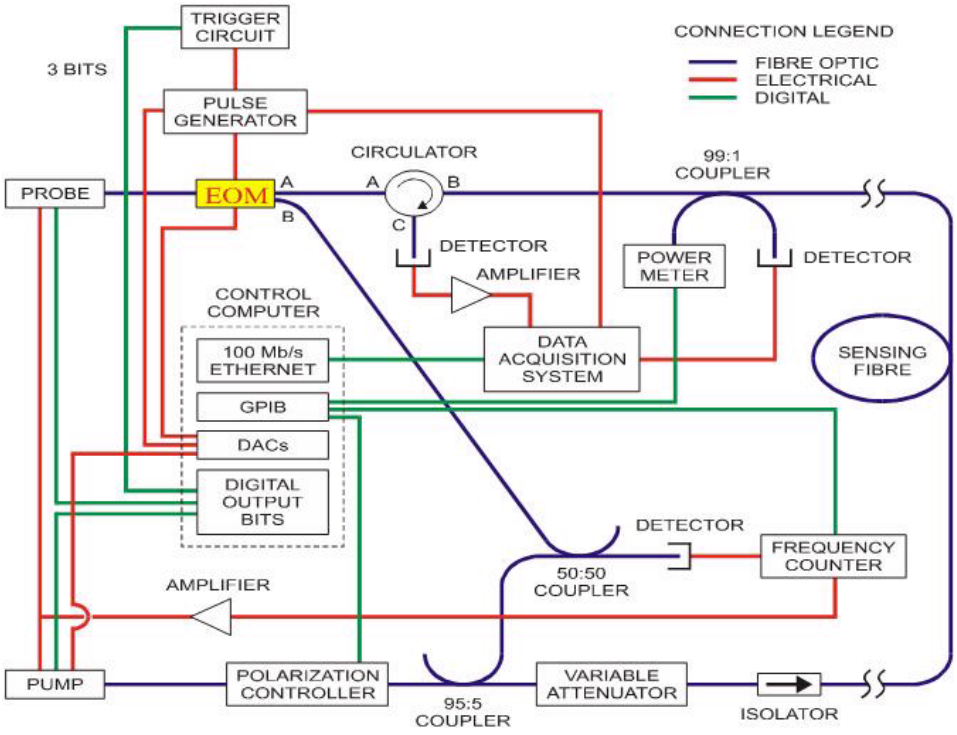

Figure 3.1: System configuration of the distributed Brillouin sensor based on two 1310 nm Nd:YAG lasers. (This figure was drawn by A. Brown in his thesis[2].)

the core[35, 44]) thereby averaging of the Brillouin effect over all polarization states is required. Thus, a polarization controller is used to fix the initial polarization state of the cw pump in the former case and to scramble the polarization states of the cw pump in the latter case. After passing the polarization controller, the cw pump is split by a 13dB coupler into a 5% part for monitoring the beat frequency of the two lasers and a 95% part for sensing. Not all of the 95% of the cw pump enters the sensing fiber, but the amounts are controlled by a variable attenuator, which ensures that the interaction occurs below the SBS threshold. The attenuated cw pump finally passes an optical isolator which protects the stability of the pump laser by blocking any counter-propagating light.

The probe laser beam is first modulated by an EOM into a pulsed Stokes wave. The EOM emits a reference signal for monitoring the beat frequency of the two lasers and also sends the pulsed beam into port A of a 3-port optical circulator. This pulsed laser beam exits from port B of the circulator and is then split by a 20dB coupler into a 1% part for monitoring the pulse

via a digitizer and a 99% part which enters the sensing fiber for interaction with the cw pump.

Propagating along the sensing fiber, the pulsed Stokes wave interacts with the cw pump via the induced phonon field. Through this interaction, the cw pump passes part of its energy to the pulsed Stokes beam. This depleted cw pump then enters port B of the circulator and exits from port C. A photodetector converts the depleted cw pump signal, into an electric signal which is then acquired by the digitizer passing the collected data into a computer for data analysis based on BOTDA. The whole procedure is controlled by a computer program.

3.2 Electro-optic Modulator (EOM)

The EOM is a key component in our sensor. It modulates the input laser signal using a pulsed electrical modulation signal to produce the output of a pulsed light signal which is the pulsed Stokes beam (the probe beam). Over the past several decades, several types of external optical intensity modulators have been developed. These include Lithium Niobate ($LiNbO_3$) modulators, semiconductor electroabsorption modulators (EAMs), semiconductor Mach-Zehnder modulators (MZMs), and polymer modulators[45]. Most of the modern wide-bandwidth modulators are based on two types of physical effect: one is the linear electro-optic (EO) effect and the other is the electroabsorption (EA) effect, which is non-linear.

3.2.1 Working principles of our EOM

The EOM employed in our system is a balanced push-pull $LiNbO_3$ MZM based on the linear EO effect, which denotes the refractive index change in optical crystals due to an applied electric field. Fig. 3.2 is a schematic drawing of this EOM. The input light is divided into two equal parts by the 3dB coupler, which then passes into two arms made of $LiNbO_3$. The total applied voltage V, including bias voltage V_{bias} and modulation voltage V_{m}, modifies the refractive indices in both of the two arms and hence modulates the optical phases of the light beams traveling in the two arms so that there is a phase difference $\Delta\Phi$ between them when they enter the 3dB coupler on the output side. The coupler combines the two beams as the output. When the two laser beams are in phase, i.e. $\Delta\Phi = 0$, their combination is coherent and produce

a maximum optical intensity output. When they are out of phase, i.e. $\Delta\Phi = \pi$, a minimum output intensity is reached. If $\Delta\Phi = \pi$ is not reached, there will be a DC component in the output. Therefore, a definition of extinction ratio naturally follows to describe the relative magnitude of the DC component to the peak output intensity: $R_x = 10\lg\left[\left(I_{\mathtt{out}}\right)_{\max} / \left(I_{\mathtt{out}}\right)_{\min}\right]$ (dB). In reality, even when $\Delta\Phi$ is adjusted to be π, there is still a DC component in the output, since the optical amplitudes in the two arms cannot be ideally balanced. In the next section, we derive the general form of extinction ratio taking both of these two factors into account. Practically, even when no voltage is applied, there exists a small phase difference $\Delta\Phi_0$ due to an imperfect match of the two arm lengths. This is why a bias voltage V_{bias} is needed not only to compensate this $\Delta\Phi_0$ but also to choose the preferred initial phase difference.

The following equations relate the phase difference $\Delta\Phi$, applied voltage V and some material related parameters (from [45] with some modification):

$$\begin{aligned} \Delta\Phi &= \Delta\Phi_0 + \pi\frac{V}{V_\pi} = \Delta\Phi_0 + \pi\frac{V_{\text{bias}}}{V_\pi} + \pi\frac{V_{\text{m}}}{V_\pi} = \Delta\Phi_{\text{bias}} + \pi\frac{V_{\text{m}}}{V_\pi} \\ V_\pi &= \frac{\lambda}{n_0^3 r_{ij}} \cdot \frac{d}{\gamma L}, \end{aligned} \tag{3.1}$$

where n_0 is the index of the active layer of the crystal at zero applied voltage, d is the spatial gap between the electrodes across which the voltage is applied[45]. λ is the optical wavelength, r_{ij} is the relevant EO coefficient of the material, γ is the optical confinement factor defined as the portion of the optical mode that is confined in the active layer[46], L is the modulation length, V_π denotes the voltage required to produce a π phase difference, and $\Delta\Phi_{\text{bias}} = \Delta\Phi_0 + \pi\frac{V_{\text{bias}}}{V_\pi}$ is the bias point of modulation prepared by the bias voltage. The choice of $\Delta\Phi_{\text{bias}}$ needs some discussion. Taking the cosinusoidal modulation curve as an example, when choosing $\Delta\Phi_{\text{bias}} = 0$, one normally obtains a reversed signal with a doubled frequency of the modulation signal if allowing V_{m} to vary from negative to positive values. When choosing $\Delta\Phi_{\text{bias}} = \pi$, one obtains an unreversed optical signal. One can also choose other quadrature points like $\frac{\pi}{2}$ and $\frac{3\pi}{2}$ where the transfer from modulation signal to output signal is almost linear. In any case, except for special purposes one does not expect $\Delta\Phi_{\text{bias}} + \pi\frac{V_{\text{m}}}{V_\pi}$ to exceed the turning points closest to $\Delta\Phi_{\text{bias}}$ since otherwise a change in the output pulse shape from that of the modulation signal

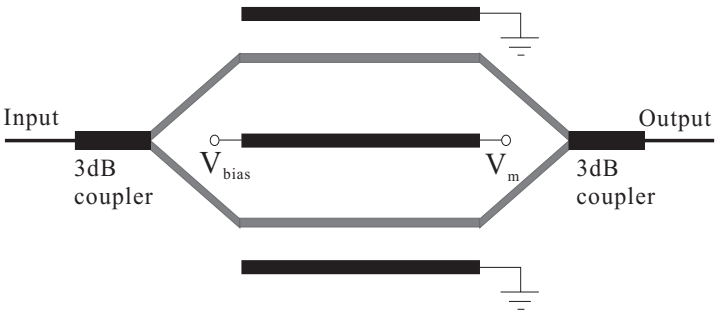

Figure 3.2: Structure of a balanced push-pull MZM

will happen.

3.2.2 Output laser field of our EOM

We now derive the output field of our EOM, since this is very important to the simulation of the sensing mechanism. To generate the pulsed laser beam using the EOM, a pulsed microwave modulation signal is employed to change the applied voltage on the EOM. Thus, the phase difference between the optical waves in the two arms can be abstracted into a time dependent function $\phi(t)$ containing the modulation information. For example, to produce an optical mth-order super Gaussian pulse centered at t_0 with a width of τ_p, $\phi(t)$ can be written as

$$\phi(t) = \phi_0 + \phi_{\max} \mathrm{e}^{-\ln 2\left(\frac{t-t_0}{\tau_p/2}\right)^m},$$

where $\phi_{\max}$ denotes the maximum possible phase difference produced by V_{m}; ϕ_0 is actually $\Delta\Phi_{\mathrm{bias}}$. Now consider the general case, in which the two arms are not perfectly balanced so that the optical waves in them have amplitudes A_1 and A_2 respectively; and the induced phases in the two arms are not perfectly opposite to each other. Then, for a MZM, the output optical field can be written as

$$E_{\mathtt{out}} = \frac{\sqrt{2}}{2}\left[A_1 \mathtt{e}^{\mathtt{i}[\omega t + \eta\phi(t)]} + A_2 \mathtt{e}^{\mathtt{i}[\omega t - (1-\eta)\phi(t)]}\right], \tag{3.2}$$

where ω is the optical frequency and the $\frac{\sqrt{2}}{2}$ comes from the 3dB coupler at the exit of the EOM. It is more convenient to use the ratio, A_2/A_1, since $\sqrt{A_1^2+A_2^2}=I_{\text{in}}$. η ($\in[0,1]$) denotes the ratio of the voltage induced phase in the upper arm to the total phase $\phi(t)$. Hence Eq. (3.2) can be written as

$$\begin{aligned} E_{\texttt{out}} &= \frac{\sqrt{2}}{2}\sqrt{A_1^2+A_2^2}\mathsf{e}^{\mathtt{i}\omega t}\left[\frac{A_1}{\sqrt{A_1^2+A_2^2}}\mathsf{e}^{\mathtt{i}\eta\phi(t)}+\frac{A_2}{\sqrt{A_1^2+A_2^2}}\mathsf{e}^{-\mathtt{i}(1-\eta)\phi(t)}\right] \\ &= A_{\texttt{out}}\left[\cos\theta\mathsf{e}^{\mathtt{i}\eta\phi(t)}+\sin\theta\mathsf{e}^{-\mathtt{i}(1-\eta)\phi(t)}\right], \end{aligned} \tag{3.3}$$

where $A_{\texttt{out}}=\frac{\sqrt{2}}{2}\sqrt{A_1^2+A_2^2}\mathsf{e}^{\mathtt{i}\omega t}=\sqrt{\frac{I_{\text{in}}}{2}}\mathsf{e}^{\mathtt{i}\omega t}$ and $\theta=\arctan\frac{A2}{A1}\in\left[0,\frac{\pi}{2}\right]$. When $\theta=\frac{\pi}{4}$ and $\eta=0.5$, Eq. (3.3) represents the output field of a balanced push-pull MZM, while it reduces to the output field of a single arm modulated MZM when $\eta=0$ or 1. The output intensity is

$$\begin{aligned} I_{\texttt{out}} &= \left|E_{\texttt{out}}\right|^2 \\ &= A_{\texttt{out}}^2\left|\cos\theta\mathsf{e}^{\mathtt{i}\phi(t)/2}+\sin\theta\mathsf{e}^{-\mathtt{i}\phi(t)/2}\right|^2 \\ &= A_{\texttt{out}}^2\left[1+\sin 2\theta\cos\phi(t)\right]. \end{aligned} \tag{3.4}$$

This equation is the transfer function for the Mach-Zehnder EOM. Therefore, the general form of extinction ratio is defined by:

$$\begin{aligned} R_x &= 10\lg\frac{\left(I_{\texttt{out}}\right)_{\max}}{\left(I_{\texttt{out}}\right)_{\min}} \\ &= 10\lg\frac{1+\sin 2\theta\cos\left(\phi_0+\phi_{\max}\right)}{1+\sin 2\theta\cos\phi_0}. \end{aligned} \tag{3.5}$$

As indicated by the specifications of our EOM, the bias point is adjustable between π and $\frac{3\pi}{2}$ (or equivalently the counterpart region in the next period of the cosinusoidal transfer curve), the modulation voltage V_{m} is required to vary in a region such that the phase difference induced by this voltage will never exceed $\frac{\pi}{2}$, since we do not want a substantial deformation of the output optical pulse. This is illustrated in Fig. 3.3. Therefore, one can assume $\phi_0=\pi+\Delta\phi$ with $\Delta\phi\in[0,\pi/2]$ and $\phi_{\max}=\frac{\pi}{2}$ without any loss of generality. The extinction ratio is now

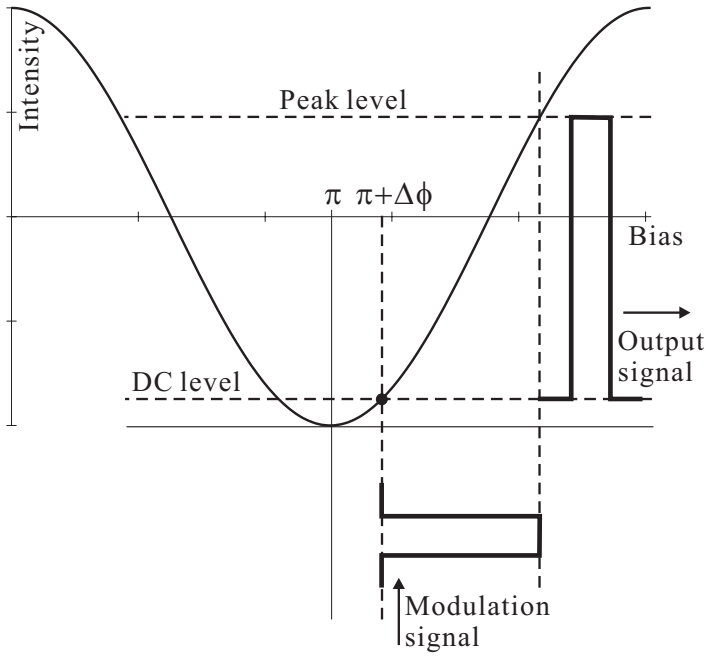

Figure 3.3: Transfer function and modulation range of the push-pull MZM used in our sensor.

determined only by $\Delta\phi$ when θ is fixed.

$$\begin{aligned} R_x &= 10\lg\frac{1+\sin 2\theta\cos\left(\pi+\frac{\pi}{2}+\Delta\phi\right)}{1+\sin 2\theta\cos\left(\pi+\Delta\phi\right)} \\ &= 10\lg\frac{1+\sin 2\theta\sin\Delta\phi}{1-\sin 2\theta\cos\Delta\phi}. \end{aligned} \tag{3.6}$$

3.3 Optical Isolator

During transmission, a beam of light is passing through many different optical interfaces which reflect the light. This backward reflected beam will go back to the light source through their original paths. When the intensity of the backward light is accumulated beyond a certain amount, many optical components, especially the light source, become unstable and generate problems such as frequency shifts and amplitude variation. No doubt this feedback beam must be suppressed. Optical isolators are the components widely used to isolate the backward light.

The optical isolator used in our sensor blocks not only the reflected cw pump beams but also the pulsed Stokes beam incident at the other end of fiber from impacting the stability of the sensing system. There are mainly two types of optical isolator, one is polarization-dependent while the other one is polarization-independent. The central part of both of the two types is a Faraday rotator[47] (a magnetic garnet crystal having a large Faraday effect[48]). However, the working principles of the first kind is simpler than that of the second. So we are going to introduce the first kind then the second kind.

3.3.1 Polarization-dependent optical isolator

This type of isolator is normally composed of a polarizer and an analyzer with a Faraday rotator between them. As shown in Fig. 3.4, the polarizer and analyzer have a 45° difference in the direction of their light transmission axes. The Faraday rotator rotates the polarization of the light passing through it by 45°. As shown in Fig. 3.4(a), the forward light, after transmission through the polarizer, is turned into linearly polarized beam in the same direction as the that of the light transmission axis of the polarizer. This linearly polarized light is rotated by the Faraday rotator 45° so that its polarization is now in the same direction as that of the light transmission axis of the analyzer. Thus, this light will completely pass the analyzer without any loss. On the other hand, as shown in Fig. 3.4(b), backward beam passing the analyzer becomes linearly polarized with an angle of 45° between the transmission axis of the polarizer. However, the Faraday rotator, by its non-reciprocality[47], only rotates the polarization of light in the same direction as it does to the forward light, regardless of whether the light is forward or backward. Thus, after the Faraday rotator, the polarization of the backward light is totally perpendicular to the transmission axis of the polarizer. As a consequence, the backward light is completely blocked by the polarizer. Therefore, light beams can only go through the isolator in the defined forward direction. Reflected light beams and any other light incident from downstream optical fiber are not allowed to transmit.

Nevertheless, this type of isolator has a major drawback; when the incident light is not polarized in the direction of the transmission axis of the polarizer, it suffers a loss described by

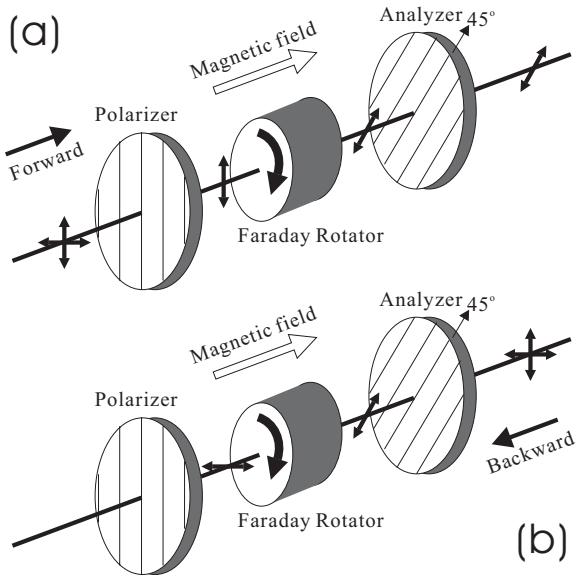

Figure 3.4: Structure and working principles of a polarization-dependent optical isolator. (a) shows how the isolator transmits forward light. (b) illustrates how the isolator blocks backward light. This figure is redrawn and modified from the figure by Hikariai[3].

Malus's law (after E. L. Malus):

$$I_1 = I_0 \cos^2 \alpha,$$

where I_0, I_1 and α denote respectively the incident intensity, transmitted intensity and the angle between the polarization of the incident light and the transmission axis of the polarizer. In our sensor setup, in order to average the effects of polarization, a polarization scrambler is used to scan all polarization states of the cw pump beam. Consequently, we demand that the isolator be polarization-independent so that the cw pump does not have an unpredicted loss after passing through the isolator. This leads to the polarization-independent optical isolator introduced in the following.

3.3.2 Polarization-independent optical isolator

The configuration of a polarization-independent optical isolator is depicted in Fig. 3.5 where the Faraday rotator is still the key in the middle but the polarizer and analyzer are replaced by two specialized birefringent plates and a convergent lens is placed at both ends of the isolator

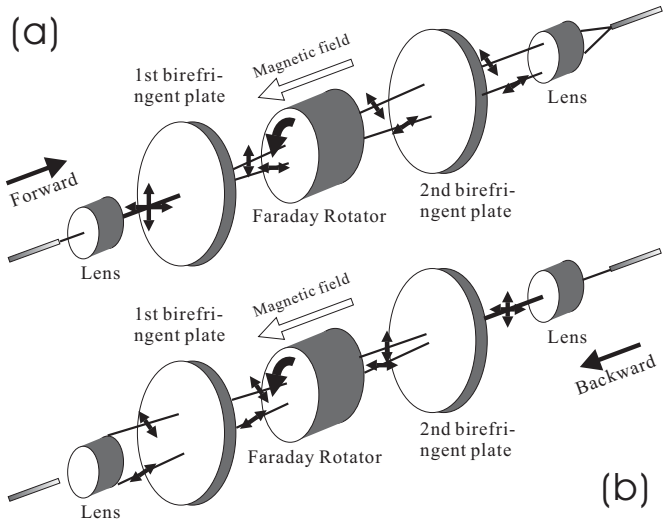

Figure 3.5: Structure and working principles of a polarization-independent optical isolator. (a) shows how the isolator transmits forward light. (b) illustrates how the isolator blocks backward light. This figure is redrawn and modified from the figure by Hikariai[3].

for coupling with optical fibers. As shown in Fig. 3.5(a), a forward incident light undergoes the following: (1) it is separated into ordinary (o) and extraordinary (e) rays by the first birefringent plate; (2) polarization planes of both of the two rays are rotated 45° by the Faraday rotator; (3) the second birefringent plate, which has an optic axis maintaining the relation between the incident ordinary and extraordinary rays, refracts the two rays so that they become parallel when exiting from this birefringent plate; (4) these two parallel beams are then converged into the downstream optical fiber by the lens at the end of the isolator. While in Fig. 3.5(b), a backward light incident from the downstream fiber on the same isolator is blocked in the following way: (a) it is also separated into an o-ray and an e-ray by the second birefringent plate; (b) again by the non-reciprocity of the Faraday rotator, the two rays are rotated 45° in the same direction indicated in the figure so that their relation is completely reversed; (c) these two reversely-related rays will not become parallel after exiting from the first birefringent plate and neither converge into a single beam as a result. Rutile single crystals (TiO_2) are mostly used as birefringent plates due to their superior extinction ratios and wide differences between the refraction indexes of the o-ray and e-ray[3]. Non-spherical lenses with a focal length of several millimeters are employed to link the isolator with optical fibers[3].

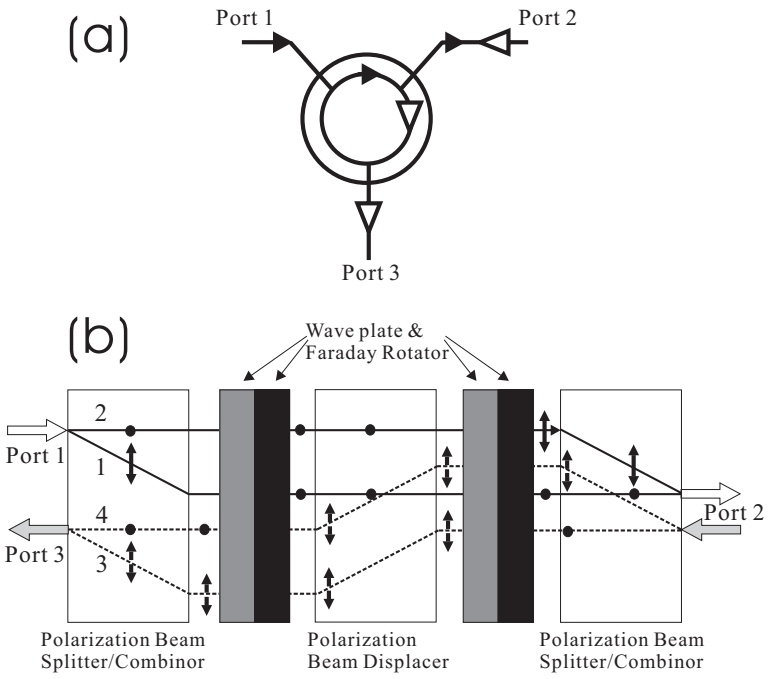

Figure 3.6: (a) sketches the function of a 3-port optical circulator. (b) illustrates the working principle of a 3-port optical circulator

3.4 Optical Circulator

In our sensor configuration, the pulsed Stokes beam is injected into the sensing fiber at the same position where the depleted counter-propagating cw pump beam is detected, so a kind of optical component is needed to guide the cw pump beam into the detector without any impact on the pulsed Stokes beam. That is, the cw pump beam must be kept from entering the portion of fiber in which the pulsed Stokes is transmitting before going into the sensing fiber. Otherwise the EOM and laser source will be severely impacted by this counter-propagating cw pump beam. 3-port optical circulators meet our demand. The function of a 3-port optical circulator is sketched in Fig. 3.6(a) where the light incident in port 1 can only exit the circulator from port 2 while the light incident in port 2 exits only from port 3; all other directions are blocked.

Fig. 3.6(b) illustrates the working principles of a 3-port optical circulator. A polarization beam splitter/combiner is placed on both ends of the circulator while a polarization beam

displacer is located in the middle. Between each beam splitter/combiner and the beam displacer there is a combination of a wave plate and a Faraday rotator. the light incident through port 1 undergoes the following: (1) when passing through the left polarization splitter/combiner on the left, it is separated into two perpendicularly polarized rays, one vertically polarized ray 1 (represented by a vertical double arrow) and one horizontally polarized ray 2 (represented by a black dot); (2)when passing through the left wave plate and Faraday rotator designed so that ray 1 is rotated by 90° and ray 2 is not rotated, both of the two rays become horizontally polarized; (3) the two rays are still horizontally polarized after exiting from the beam displacer with an optic axis so that horizontally polarized light is not displaced; (4) the right combination of wave plate and Faraday rotator rotates ray 2 by 90° so that it becomes vertically polarized; (5) the splitter/combiner on the right thereby combines ray 1 and ray 2 into a single light beam which exits the circulator from port 2. On the other hand, the light incident through port 2 is split again into two rays (ray 3 and ray 4) with orthogonal polarizations. Both are vertically polarized after the first wave plate and rotator on the right side since the polarization of ray 3 is rotated by 90°. As a consequence, they are displaced (actually refracted) by the displacer. The wave plate and rotator on the left side turns ray 4 into a horizontally polarized beam. Therefore the left splitter/combiner combines them back into a single light beam exiting through port 3.

Chapter 4

Sensor simulation based on the 3-wave transient model

As mentioned in Chapter 1, phenomena such as the sub-peaks in Brillouin spectra and the high spatial resolution with narrow spectral bandwidth and high SNR obtained from experiments on the 1310-sensor have not been explained theoretically. A theoretical study is highly desirable to solve these problems. The simulation of the distributed Brillouin sensing system is the best way to achieve this goal and may bring out significant predictions for future applications. This chapter aims at providing the numerical solutions of the 3-wave transient model described by Eqs. (2.9) and discusses key points of the simulation based on these numerical solutions.

4.1 Numerical solution of the model

Eqs. (2.9) can be solved by applying a numerical method introduced by Chu *et al.*[1]. Since Eq. (2.9c) is a first order non-homogeneous linear equation, the general solution is simply

$$\begin{aligned} \bar{Q}(z,t) &= \frac{1}{2}\Gamma_1 g_B \mathrm{e}^{-\Gamma t}\int_0^t E_p(z,t')\,E_s^*(z,t')\,\mathrm{e}^{\Gamma t'}\mathrm{d}t' \\ &= \frac{1}{2}\Gamma_1 g_B \int_0^t E_p E_s^* \mathrm{e}^{-\Gamma(t-t')}\mathrm{d}t' + \bar{Q}_0(z,t). \end{aligned} \tag{4.1}$$

$\bar{Q}_0(z,t)$ is the initial white noise of the phonon field. Substituting Eq. (4.1) into (2.9a) and (2.9b) yields

$$\left(\frac{\partial}{\partial z}-\frac{1}{v_g}\frac{\partial}{\partial t}-\frac{1}{2}\alpha\right)E_p = \frac{1}{2}\Gamma_1 g_B E_s\int_0^t E_p E_s^* \mathrm{e}^{-\Gamma(t-t')}\mathrm{d}t' + \bar{Q}_0 E_s \tag{4.2a}$$

$$\left(\frac{\partial}{\partial z}+\frac{1}{v_g}\frac{\partial}{\partial t}+\frac{1}{2}\alpha\right)E_s = \frac{1}{2}\Gamma_1 g_B E_p\int_0^t E_p^* E_s \mathrm{e}^{-\Gamma^*(t-t')}\mathrm{d}t' + \bar{Q}_0^* E_p. \tag{4.2b}$$

Applying fully implicit finite differencing in time and backward differencing in space[49, 50] to Eqs. (4.2), we find

$$\frac{E_{p_{n+1}}^{m+1}-E_{p_n}^{m+1}}{\Delta z}-a\frac{E_{p_n}^{m+1}-E_{p_n}^{m}}{\Delta t}-bE_{p_n}^{m+1} = \frac{1}{2}\Gamma_1 g_B E_{s_n}^{m+1}\times \int_0^{t_{m+1}} E_p E_s^* \mathrm{e}^{-\Gamma(t_{m+1}-t')}\mathrm{d}t' + \bar{Q}_{0_n}^{m+1}E_{s_n}^{m+1}$$

$$\frac{E_{s_{n+1}}^{m+1}-E_{s_n}^{m+1}}{\Delta z}+a\frac{E_{s_n}^{m+1}-E_{s_n}^{m}}{\Delta t}+bE_{s_n}^{m+1} = \frac{1}{2}\Gamma_1 g_B E_{p_n}^{m+1}\times \int_0^{t_{m+1}} E_p^* E_s \mathrm{e}^{-\Gamma^*(t_{m+1}-t')}\mathrm{d}t' + \bar{Q}_{0_n}^{*m+1}E_{p_n}^{m+1},$$

where $a=\frac{1}{v_g}$, $b=\frac{1}{2}\alpha$,

$$\begin{aligned} m &= 0,1,2,\cdots M \text{ are time indices and } t_m = m\Delta t,\\ n &= 0,1,2,\cdots N \text{ are space indices and } z_n = n\Delta z; \end{aligned}$$

$E_{p_n}^m$ and $E_{s_n}^m$ are the pump and stokes fields at position z_n and time t_m respectively. That is,

$$E_{p_{n+1}}^{m+1}-E_{p_n}^{m+1}-\frac{a\Delta z}{\Delta t}\left(E_{p_n}^{m+1}-E_{p_n}^{m}\right)-b\Delta z E_{p_n}^{m+1}-\Delta z\bar{Q}_{0_n}^{m+1}E_{s_n}^{m+1} \tag{4.3a}$$

$$= \frac{\Delta z}{2}\Gamma_1 g_B E_{s_n}^{m+1}\int_0^{t_{m+1}} E_p E_s^* \mathrm{e}^{-\Gamma(t_{m+1}-t')}\mathrm{d}t'$$

$$E_{s_{n+1}}^{m+1}-E_{s_n}^{m+1}+\frac{a\Delta z}{\Delta t}\left(E_{s_n}^{m+1}-E_{s_n}^{m}\right)+b\Delta z E_{s_n}^{m+1}-\Delta z\bar{Q}_{0_n}^{*m+1}E_{p_n}^{m+1} \tag{4.3b}$$

$$= \frac{\Delta z}{2}\Gamma_1 g_B E_{p_n}^{m+1}\int_0^{t_{m+1}} E_p^* E_s \mathrm{e}^{-\Gamma^*(t_{m+1}-t')}\mathrm{d}t'$$

The integrals on the RHS of Eqs. (4.3) can be evaluated by Simpson's rule. For Eq. (4.3a),

$$\begin{aligned}
&\int_0^{t_{m+1}} E_p E_s^* \mathrm{e}^{-\Gamma(t_{m+1}-t')}\mathrm{d}t' \\
= \;& \frac{\Delta t}{2} E_{p_n}^0 E_{s_n}^{*0} \mathrm{e}^{-\Gamma(m+1)\Delta t} + \Delta t E_{p_n}^1 E_{s_n}^{*1} \mathrm{e}^{-\Gamma m \Delta t} + \cdots + \Delta t E_{p_n}^m E_{s_n}^{*m} \mathrm{e}^{-\Gamma \Delta t} + \frac{\Delta t}{2} E_{p_n}^{m+1} E_{s_n}^{*m+1} \\
= \;& \frac{\Delta t}{2} \left(E_{p_n}^0 E_{s_n}^{*0} \mathrm{e}^{-\Gamma(m+1)\Delta t} + 2E_{p_n}^1 E_{s_n}^{*1} \mathrm{e}^{-\Gamma m \Delta t} + \cdots + 2E_{p_n}^m E_{s_n}^{*m} \mathrm{e}^{-\Gamma \Delta t} + E_{p_n}^{m+1} E_{s_n}^{*m+1} \right) \\
= \;& \frac{\Delta t}{2} \left\{ \left\{ \left[\left(E_{p_n}^0 E_{s_n}^{*0} \mathrm{e}^{-\Gamma \Delta t} + 2E_{p_n}^1 E_{s_n}^{*1} \right) \mathrm{e}^{-\Gamma \Delta t} + 2E_{p_n}^2 E_{s_n}^{*2} \right] \mathrm{e}^{-\Gamma \Delta t} + \cdots + 2E_{p_n}^m E_{s_n}^{*m} \right\} \mathrm{e}^{-\Gamma \Delta t} \right. \\
& \qquad \left. + E_{p_n}^{m+1} E_{s_n}^{*m+1} \right\} \\
= \;& \frac{\Delta t}{2} \left(\phi_n^m + E_{p_n}^{m+1} E_{s_n}^{*m+1} \right), \qquad (4.4)
\end{aligned}$$

where ϕ_n^m is recursively defined as

$$\phi_n^m = \begin{cases} \left(\phi_n^{m-1} + 2E_{p_n}^m E_{s_n}^{*m} \right) \mathrm{e}^{-\Gamma \Delta t} & m \geq 1 \\ E_{p_n}^0 E_{s_n}^{*0} \mathrm{e}^{-\Gamma \Delta t} & m = 0 \end{cases}. \qquad (4.5)$$

For the integral of (4.3b), in a similar manner we find

$$\int_0^{t_{m+1}} E_p^* E_s \mathrm{e}^{-\Gamma^*(t_{m+1}-t')}\mathrm{d}t' = \frac{\Delta t}{2} \left(\psi_n^m + E_{p_n}^{*m+1} E_{s_n}^{m+1} \right) \qquad (4.6)$$

by defining

$$\psi_n^m = \begin{cases} \left(\psi_n^{m-1} + 2E_{p_n}^{*m} E_{s_n}^m \right) \mathrm{e}^{-\Gamma^* \Delta t} & m \geq 1 \\ E_{p_n}^{*0} E_{s_n}^0 \mathrm{e}^{-\Gamma^* \Delta t} & m = 0 \end{cases}. \qquad (4.7)$$

Substituting Eqs. (4.4) and (4.6) into (4.3a & 4.3b), we get

$$\begin{aligned}
& E_{p_{n+1}}^{m+1} - E_{p_n}^{m+1} - \frac{a\Delta z}{\Delta t} \left(E_{p_n}^{m+1} - E_{p_n}^m \right) - b\Delta z E_{p_n}^{m+1} - \Delta z \bar{Q}_0 E_{s_n}^{m+1} \\
= \;& \chi \left(\phi_n^m E_{s_n}^{m+1} + E_{p_n}^{m+1} \left| E_{s_n}^{m+1} \right|^2 \right), \qquad (4.8a) \\
& E_{s_{n+1}}^{m+1} - E_{s_n}^{m+1} + \frac{a\Delta z}{\Delta t} \left(E_{s_n}^{m+1} - E_{s_n}^m \right) + b\Delta z E_{s_n}^{m+1} - \Delta z \bar{Q}_{0_n}^{*m+1} E_{p_n}^{m+1} \\
= \;& \chi \left(\psi_n^m E_{p_n}^{m+1} + \left| E_{p_n}^{m+1} \right|^2 E_{s_n}^{m+1} \right), \qquad (4.8b)
\end{aligned}$$

where $\chi = \frac{\Gamma_1 g_B}{4}\Delta z \Delta t$. The above two equations are actually nonlinear because the coefficients of $E_{p_n}^{m+1}$ and $E_{s_n}^{m+1}$ in their RHS are unknown. However, linearization can be accomplished by replacing these unknowns by their values at the previous time slot m[1]. We then have

$$\begin{aligned} & E_{p_{n+1}}^{m+1} - E_{p_n}^{m+1} - \frac{a\Delta z}{\Delta t}\left(E_{p_n}^{m+1} - E_{p_n}^{m}\right) - b\Delta z E_{p_n}^{m+1} - \Delta z \bar{Q}_{0_n}^{m+1} E_{s_n}^{m+1} \qquad (4.9a) \\ = \;& \chi\left(\phi_n^m E_{s_n}^{m+1} + \left|E_{s_n}^m\right|^2 E_{p_n}^{m+1}\right), \\ & E_{s_{n+1}}^{m+1} - E_{s_n}^{m+1} + \frac{a\Delta z}{\Delta t}\left(E_{s_n}^{m+1} - E_{s_n}^{m}\right) + b\Delta z E_{s_n}^{m+1} - \Delta z \bar{Q}_{0_n}^{*m+1} E_{p_n}^{m+1} \qquad (4.9b) \\ = \;& \chi\left(\psi_n^m E_{p_n}^{m+1} + \left|E_{p_n}^m\right|^2 E_{s_n}^{m+1}\right). \end{aligned}$$

Since we know that the pump wave is injected at $z = L$, while the Stokes wave is injected at $z = 0$, $E_{p_N}^{m+1}$ and E_{s0}^{m+1} can be considered as their boundary conditions at time $t = (m+1)\,\Delta t$ respectively. Therefore, we can group the unknown values of E_p and E_s in positions other than $z = L$ and $z = 0$ respectively together into vectors as

$$\mathbf{E}_p^{m+1} = \left(\; E_{p_0}^{m+1},\;\; E_{p_1}^{m+1},\;\; \cdots,\;\; E_{p_{N-1}}^{m+1} \;\right)^T \text{ and } \mathbf{E}_s^{m+1} = \left(\; E_{s_1}^{m+1},\;\; E_{s_2}^{m+1},\;\; \cdots,\;\; E_{s_N}^{m+1} \;\right)^T. \qquad (4.10)$$

Accordingly, we can write Eq. (4.9a) as a series from $n = 0$ to $n = N-1$ as

$$\begin{cases} E_{p_1}^{m+1} - E_{p_0}^{m+1} - \frac{a\Delta z}{\Delta t}\left(E_{p_0}^{m+1} - E_{p_0}^{m}\right) - b\Delta z E_{p_0}^{m+1} - \Delta z \bar{Q}_{0_0}^{m+1} E_{s_0}^{m+1} \\ = \chi\left(\phi_0^m E_{s_0}^{m+1} + \left|E_{s_0}^m\right|^2 E_{p_0}^{m+1}\right) \\ E_{p_2}^{m+1} - E_{p_1}^{m+1} - \frac{a\Delta z}{\Delta t}\left(E_{p_1}^{m+1} - E_{p_1}^{m}\right) - b\Delta z E_{p_1}^{m+1} - \Delta z \bar{Q}_{0_1}^{m+1} E_{s_1}^{m+1} \\ = \chi\left(\phi_1^m E_{s_1}^{m+1} + \left|E_{s_1}^m\right|^2 E_{p_1}^{m+1}\right) \\ \vdots \\ E_{p_{N-1}}^{m+1} - E_{p_{N-2}}^{m+1} - \frac{a\Delta z}{\Delta t}\left(E_{p_{N-2}}^{m+1} - E_{p_{N-2}}^{m}\right) - b\Delta z E_{p_{N-2}}^{m+1} - \Delta z \bar{Q}_{0_{N-2}}^{m+1} E_{s_{N-2}}^{m+1} \\ = \chi\left(\phi_{N-2}^m E_{s_{N-2}}^{m+1} + \left|E_{s_{N-2}}^m\right|^2 E_{p_{N-2}}^{m+1}\right) \\ E_{p_N}^{m+1} - E_{p_{N-1}}^{m+1} - \frac{a\Delta z}{\Delta t}\left(E_{p_{N-1}}^{m+1} - E_{p_{N-1}}^{m}\right) - b\Delta z E_{p_{N-1}}^{m+1} - \Delta z \bar{Q}_{0_{N-1}}^{m+1} E_{s_{N-1}}^{m+1} \\ = \chi\left(\phi_{N-1}^m E_{s_{N-1}}^{m+1} + \left|E_{s_{N-1}}^m\right|^2 E_{p_{N-1}}^{m+1}\right) \end{cases}.$$

After some manipulation, we have

$$\begin{cases} -\left(1+\frac{a\Delta z}{\Delta t}+b\Delta z+\chi\left|E_{s_0}^m\right|^2\right)E_{p_0}^{m+1}+E_{p_1}^{m+1}=\left(\chi\phi_0^m+\Delta z\bar{Q}_{0_0}^{m+1}\right)E_{s_0}^{m+1}-\frac{a\Delta z}{\Delta t}E_{p_0}^m \\ -\left(1+\frac{a\Delta z}{\Delta t}+b\Delta z+\chi\left|E_{s_1}^m\right|^2\right)E_{p_1}^{m+1}+E_{p_2}^{m+1}-\left(\chi\phi_1^m+\Delta z\bar{Q}_{0_1}^{m+1}\right)E_{s_1}^{m+1}=-\frac{a\Delta z}{\Delta t}E_{p_1}^m \\ \vdots \\ -\left(1+\frac{a\Delta z}{\Delta t}+b\Delta z+\chi\left|E_{s_{N-2}}^m\right|^2\right)E_{p_{N-2}}^{m+1}+E_{p_{N-1}}^{m+1}-\left(\chi\phi_{N-2}^m+\bar{Q}_{0_{N-2}}^{m+1}\right)E_{s_{N-2}}^{m+1}=-\frac{a\Delta z}{\Delta t}E_{p_{N-2}}^m \\ -\left(1+\frac{a\Delta z}{\Delta t}+b\Delta z+\chi\left|E_{s_{N-1}}^m\right|^2\right)E_{p_{N-1}}^{m+1}-\left(\chi\phi_{N-1}^m+\Delta z\bar{Q}_{0_{N-1}}^{m+1}\right)E_{s_{N-1}}^{m+1}=-\frac{a\Delta z}{\Delta t}E_{p_{N-1}}^m-E_{p_N}^{m+1} \end{cases}.$$

By defining $h_n^m=-\left(1+\frac{a\Delta z}{\Delta t}+b\Delta z+\chi\left|E_{s_n}^m\right|^2\right)$, the matrix form of the above equations is:

$$-\begin{pmatrix} 0 & & & & 0 \\ \left(\chi\phi_1^m+\Delta z\bar{Q}_{0_1}^{m+1}\right) & & & & \\ & \left(\chi\phi_2^m+\Delta z\bar{Q}_{0_2}^{m+1}\right) & & & \\ & & & \ddots & \\ 0 & & & & \left(\chi\phi_{N-1}^m+\Delta z\bar{Q}_{0_{N-1}}^{m+1}\right) \quad 0 \end{pmatrix}\begin{pmatrix} E_{s_1}^{m+1} \\ E_{s_2}^{m+1} \\ \vdots \\ E_{s_{N-1}}^{m+1} \\ E_{s_N}^{m+1} \end{pmatrix}$$

$$+\begin{pmatrix} h_0^m & 1 & & & 0 \\ & h_1^m & 1 & & \\ & & \ddots & \ddots & \\ & & & h_{N-2}^m & 1 \\ 0 & & & & h_{N-1}^m \end{pmatrix}\begin{pmatrix} E_{p_0}^{m+1} \\ E_{p_1}^{m+1} \\ \vdots \\ E_{p_{N-2}}^{m+1} \\ E_{p_{N-1}}^{m+1} \end{pmatrix}=\begin{pmatrix} \left(\chi\phi_0^m+\Delta z\bar{Q}_{0_0}^{m+1}\right)E_{s_0}^{m+1}-\frac{a\Delta z}{\Delta t}E_{p_0}^m \\ -\frac{a\Delta z}{\Delta t}E_{p_1}^m \\ \vdots \\ -\frac{a\Delta z}{\Delta t}E_{p_{N-2}}^m \\ -\frac{a\Delta z}{\Delta t}E_{p_{N-1}}^m-E_{p_N}^{m+1} \end{pmatrix}, \text{ i.e.,}$$

$$-\Phi^m\times\mathbf{E}_s^{m+1}+\mathbf{H}^m\times\mathbf{E}_p^{m+1}=\mathbf{V}_1^m,$$

where we set

$$\mathbf{H}^m=\begin{pmatrix} h_0^m & 1 & & & 0 \\ & h_1^m & 1 & & \\ & & \ddots & \ddots & \\ & & & h_{N-2}^m & 1 \\ 0 & & & & h_{N-1}^m \end{pmatrix}, \quad \Phi^m=\begin{pmatrix} 0 & & & & 0 \\ \nu_1^m & & & & \\ & \nu_2^m & & & \\ & \cdots & \cdots & \cdots & \\ 0 & \cdots & & \nu_{N-1}^m & 0 \end{pmatrix}, \text{ and}$$

$$\mathbf{V}_1^m = \begin{pmatrix} \nu_0^m E_{s_0}^{m+1} - \frac{a\Delta z}{\Delta t} E_{p_0}^m \\ -\frac{a\Delta z}{\Delta t} E_{p_1}^m \\ \vdots \\ -\frac{a\Delta z}{\Delta t} E_{p_{N-2}}^m \\ -\frac{a\Delta z}{\Delta t} E_{p_{N-1}}^m - E_{p_N}^{m+1} \end{pmatrix}$$

with $\nu_n^m = \chi\phi_n^m + \Delta z \bar{Q}_{0_n}^{m+1}$. We can also write Eq. (4.9b) in a series from $n = 0$ to $n = N-1$ as:

$$\begin{cases} E_{s_1}^{m+1} - E_{s_0}^{m+1} + \frac{a\Delta z}{\Delta t}\left(E_{s_0}^{m+1} - E_{s_0}^m\right) + b\Delta z E_{s_0}^{m+1} - \Delta z \bar{Q}_{0_0}^{*m+1} E_{p_0}^{m+1} \\ = \chi\left(\psi_0^m E_{p_0}^{m+1} + \left|E_{p_0}^m\right|^2 E_{s_0}^{m+1}\right) \\ E_{s_2}^{m+1} - E_{s_1}^{m+1} + \frac{a\Delta z}{\Delta t}\left(E_{s_1}^{m+1} - E_{s_1}^m\right) + b\Delta z E_{s_1}^{m+1} - \Delta z \bar{Q}_{0_1}^{*m+1} E_{p_1}^{m+1} \\ = \chi\left(\psi_1^m E_{p_1}^{m+1} + \left|E_{p_1}^m\right|^2 E_{s_1}^{m+1}\right) \\ \vdots \\ E_{s_{N-1}}^{m+1} - E_{s_{N-2}}^{m+1} + \frac{a\Delta z}{\Delta t}\left(E_{s_{N-2}}^{m+1} - E_{s_{N-2}}^m\right) + b\Delta z E_{s_{N-2}}^{m+1} - \Delta z \bar{Q}_{0_{N-2}}^{*m+1} E_{p_{N-2}}^{m+1} \\ = \chi\left(\psi_{N-2}^m E_{p_{N-2}}^{m+1} + \left|E_{p_{N-2}}^m\right|^2 E_{s_{N-2}}^{m+1}\right) \\ E_{s_N}^{m+1} - E_{s_{N-1}}^{m+1} + \frac{a\Delta z}{\Delta t}\left(E_{s_{N-1}}^{m+1} - E_{s_{N-1}}^m\right) + b\Delta z E_{s_{N-1}}^{m+1} - \Delta z \bar{Q}_{0_{N-1}}^{*m+1} E_{p_{N-1}}^{m+1} \\ = \chi\left(\psi_{N-1}^m E_{p_{N-1}}^{m+1} + \left|E_{p_{N-1}}^m\right|^2 E_{s_{N-1}}^{m+1}\right) \end{cases}.$$

After some manipulation, we have

$$\begin{cases} -\left(\chi\psi_0^m + \Delta z \bar{Q}_{0_0}^{*m+1}\right) E_{p_0}^{m+1} + E_{s_1}^{m+1} = \frac{a\Delta z}{\Delta t} E_{s_0}^m + \left(1 - \frac{a\Delta z}{\Delta t} - b\Delta z + \chi\left|E_{p_0}^m\right|^2\right) E_{s_0}^{m+1} \\ -\left(\chi\psi_1^m + \Delta z \bar{Q}_{0_1}^{*m+1}\right) E_{p_1}^{m+1} - \left(1 - \frac{a\Delta z}{\Delta t} - b\Delta z + \chi\left|E_{p_1}^m\right|^2\right) E_{s_1}^{m+1} + E_{s_2}^{m+1} = \frac{a\Delta z}{\Delta t} E_{s_1}^m \\ -\left(\chi\psi_2^m + \Delta z \bar{Q}_{0_2}^{*m+1}\right) E_{p_2}^{m+1} - \left(1 - \frac{a\Delta z}{\Delta t} - b\Delta z + \chi\left|E_{p_2}^m\right|^2\right) E_{s_2}^{m+1} + E_{s_3}^{m+1} = \frac{a\Delta z}{\Delta t} E_{s_2}^m \\ \vdots \\ -\left(\chi\psi_{N-2}^m + \Delta z \bar{Q}_{0_{N-2}}^{*m+1}\right) E_{p_{N-2}}^{m+1} - \left(1 - \frac{a\Delta z}{\Delta t} - b\Delta z + \chi\left|E_{p_{N-2}}^m\right|^2\right) E_{s_{N-2}}^{m+1} + E_{s_{N-1}}^{m+1} = \frac{a\Delta z}{\Delta t} E_{s_{N-2}}^m \\ -\left(\chi\psi_{N-1}^m + \Delta z \bar{Q}_{0_{N-1}}^{*m+1}\right) E_{p_{N-1}}^{m+1} - \left(1 - \frac{a\Delta z}{\Delta t} - b\Delta z + \chi\left|E_{p_{N-1}}^m\right|^2\right) E_{s_{N-1}}^{m+1} + E_{s_N}^{m+1} = \frac{a\Delta z}{\Delta t} E_{s_{N-1}}^m \end{cases}.$$

Then, by defining $r_n^m = -\left(1 - \frac{a\Delta z}{\Delta t} - b\Delta z + \chi\left|E_{p_n}^m\right|^2\right)$, we get the corresponding matrix form:

$$
-\begin{pmatrix}
\left(\chi\psi_0^m+\Delta z\bar{Q}_{0_0}^{*m+1}\right) & & & 0 \\
& \left(\chi\psi_1^m+\Delta z\bar{Q}_{0_1}^{*m+1}\right) & & \\
& & \ddots & \\
& & & \left(\chi\psi_{N-2}^m+\Delta z\bar{Q}_{0_{N-2}}^{*m+1}\right) \\
0 & & & \left(\chi\psi_{N-1}^m+\Delta z\bar{Q}_{0_{N-1}}^{*m+1}\right)
\end{pmatrix}
$$

$$
\times\begin{pmatrix} E_{p_0}^{m+1} \\ E_{p_1}^{m+1} \\ \vdots \\ E_{p_{N-2}}^{m+1} \\ E_{p_{N-1}}^{m+1} \end{pmatrix}+\begin{pmatrix}
1 & & & & 0 \\
r_1^m & 1 & & & \\
& r_2^m & \ddots & & \\
& & \ddots & 1 & \\
0 & & & r_{N-1}^m & 1
\end{pmatrix}\begin{pmatrix} E_{s_1}^{m+1} \\ E_{s_2}^{m+1} \\ \vdots \\ E_{s_{N-1}}^{m+1} \\ E_{s_N}^{m+1} \end{pmatrix}=\begin{pmatrix} \frac{a\Delta z}{\Delta t}E_{s_0}^m-r_0^mE_{s_0}^{m+1} \\ \frac{a\Delta z}{\Delta t}E_{s_1}^m \\ \vdots \\ \frac{a\Delta z}{\Delta t}E_{s_{N-2}}^m \\ \frac{a\Delta z}{\Delta t}E_{s_{N-1}}^m \end{pmatrix},
$$

That is,

$$
-\Psi^m\times\mathbf{E}_p^{m+1}+\mathbf{R}^m\times\mathbf{E}_s^{m+1}=\mathbf{V}_2^m,
$$

where we set

$$
\mathbf{R}^m=\begin{pmatrix}
1 & & & & 0 \\
r_1^m & 1 & & & \\
& r_2^m & \ddots & & \\
& & \ddots & 1 & \\
0 & & & r_{N-1}^m & 1
\end{pmatrix}\qquad
\Psi^m=\begin{pmatrix}
\mu_0^m & & & & 0 \\
& \mu_1^m & & & \\
& & \ddots & & \\
& & & \mu_{N-2}^m & \\
0 & & & & \mu_{N-1}^m
\end{pmatrix}
$$

with the definition of $\mu_n^m=\chi\psi_n^m+\Delta z\bar{Q}_{0_n}^{*m+1}$;

$$
\mathbf{V}_2^m=\begin{pmatrix} \frac{a\Delta z}{\Delta t}E_{s_0}^m-r_0^mE_{s_0}^{m+1} \\ \frac{a\Delta z}{\Delta t}E_{s_1}^m \\ \vdots \\ \frac{a\Delta z}{\Delta t}E_{s_{N-2}}^m \\ \frac{a\Delta z}{\Delta t}E_{s_{N-1}}^m \end{pmatrix}.
$$

Thus, in matrix form, Eqs (4.9) become

$$\begin{cases} -\Phi^m \times \mathbf{E}_s^{m+1} + \mathbf{H} \times \mathbf{E}_p^{m+1} = \mathbf{V}_1^m \\ -\Psi^m \times \mathbf{E}_p^{m+1} + \mathbf{R}^m \times \mathbf{E}_s^{m+1} = \mathbf{V}_2^m \end{cases} \tag{4.11}$$

Matrix Ψ^m is already diagonal, which gives us a convenient way to solve the coupled equations (4.11). Multiplying $-(\Psi^m)^{-1}$ on the left to the second equations of Eq. (4.11) yields

$$\mathbf{E}_p^{m+1} = (\Psi^m)^{-1} \times \mathbf{R}^m \times \mathbf{E}_s^{m+1} - (\Psi^m)^{-1} \times \mathbf{V}_2^m \tag{4.12}$$

Substitute this expression into the first equation of (4.11), we then have

$$\begin{gathered} \left[\mathbf{H}^m \times (\Psi^m)^{-1} \times \mathbf{R}^m - \Phi^m\right] \times \mathbf{E}_s^{m+1} = \mathbf{H}^m \times (\Psi^m)^{-1} \times \mathbf{V}_2^m + \mathbf{V}_1^m \\ \Downarrow \\ \mathbf{A}^m \times \mathbf{E}_s^{m+1} = \mathbf{V}^m \\ \Downarrow \\ \mathbf{E}_s^{m+1} = (\mathbf{A}^m)^{-1} \times \mathbf{V}^m, \end{gathered} \tag{4.13}$$

where we define $\mathbf{A}^m = \left[\mathbf{H}^m \times (\Psi^m)^{-1} \times \mathbf{R}^m - \Phi^m\right]$ and $\mathbf{V} = \mathbf{H}^m \times (\Psi^m)^{-1} \times \mathbf{V}_2^m + \mathbf{V}_1^m$. With all the related definitions, the matrix $\mathbf{A}^m$ and vector $\mathbf{V}^m$ can be found as

$$\mathbf{A}^m = \begin{pmatrix} \frac{h_0^m}{\mu_0^m} + \frac{r_1^m}{\mu_1^m} & \frac{1}{\mu_1^m} & 0 & \cdots & & 0 \\ \frac{h_1^m r_1^m}{\mu_1^m} - \nu_1^m & \frac{h_1^m}{\mu_1^m} + \frac{r_2^m}{\mu_2^m} & \frac{1}{\mu_2^m} & & & \vdots \\ & & \cdots & \cdots & \cdots & \\ \vdots & & \cdots & \cdots & \cdots & 0 \\ & & & \frac{h_{N-2}^m r_{N-2}^m}{\mu_{N-2}^m} - \nu_{N-2}^m & \frac{h_{N-2}^m}{\mu_{N-2}^m} + \frac{r_{N-1}^m}{\mu_{N-1}^m} & \frac{1}{\mu_{N-1}^m} \\ 0 & & \cdots & 0 & \frac{h_{N-1}^m r_{N-1}^m}{\mu_{N-1}^m} - \nu_{N-1}^m & \frac{h_{N-1}^m}{\mu_{N-1}^m} \end{pmatrix}$$

$$\mathbf{V}^m = \begin{pmatrix} \frac{h_0^m}{\mu_0^m}\left(\frac{a\Delta z}{\Delta t}E_{s_0}^m - r_0^m E_{s_0}^{m+1}\right) + \frac{a\Delta z}{\Delta t}\frac{E_{s_1}^m}{\mu_1^m} + \nu_0^m E_{s_0}^{m+1} - \frac{a\Delta z}{\Delta t}E_{p_0}^m \\ \frac{a\Delta z}{\Delta t}\left(\frac{h_1^m E_{s_1}^m}{\mu_1^m} + \frac{E_{s_2}^m}{\mu_2^m} - E_{p_1}^m\right) \\ \frac{a\Delta z}{\Delta t}\left(\frac{h_2^m E_{s_2}^m}{\mu_2^m} + \frac{E_{s_3}^m}{\mu_3^m} - E_{p_2}^m\right) \\ \vdots \\ \frac{a\Delta z}{\Delta t}\left(\frac{h_{N-2}^m E_{s_{N-2}}^m}{\mu_{N-2}^m} + \frac{E_{s_{N-1}}^m}{\mu_{N-1}^m} - E_{p_{N-2}}^m\right) \\ \frac{a\Delta z}{\Delta t}\left(\frac{h_{N-1}^m E_{s_{N-1}}^m}{\mu_{N-1}^m} - E_{p_{N-1}}^m\right) - E_{p_N}^{m+1} \end{pmatrix}$$

Therefore, the final solution becomes

$$\begin{cases} \mathbf{E}_s^{m+1} = (\mathbf{A}^m)^{-1} \times \mathbf{V}^m \\ \mathbf{E}_p^{m+1} = (\Psi^m)^{-1} \times \left[\mathbf{R}^m \times \mathbf{E}_s^{m+1} - \mathbf{V}_2^m\right] \end{cases} \tag{4.14}$$

All coefficient matrices and vectors have been calculated numerically using the values of $\mathbf{E}_s^m$ and $\mathbf{E}_p^m$ from the previous time slot by program written in Fortran90.

4.2 Simulation

The simulation based on the previous calculations was programmed in Fortran90, which is powerful and fast in mathematics. Since this implementation is closely related to the real sensing system, some practical concerns should be taken into account. The simulation is programmed in a flexible way so that it can be adapted to other situations with only simple modifications.

4.2.1 Initial and boundary conditions

To obtain E_p and E_s along the whole sensing fiber at some time slot t_{m+1}, the values of E_p and E_s at the previous time t_m must be provided, leading to the initial conditions $E_p(z,0)$, $E_s(z,0)$ of E_p and E_s. E_{p_N} and E_{s_0} do not appear in Eq. (4.10) but actually exist as the boundary conditions of the cw pump and pulsed Stokes beam respectively. The cw pump is injected at $z = L$ and is considered to exist all along the sensing fiber before pulsed Stokes beam is

injected. Thus the initial condition of E_p along the fiber is simply defined by the attenuation as $E_p(z,0) = E_{p_L} \exp\left[-\frac{\alpha}{2}(L-z)\right]$ where E_{p_L} is the incident cw pump intensity and the factor $\frac{1}{2}$ exists because this is the attenuation of the field amplitude instead of the intensity. As explained in Section 3.2.1, the pulsed Stokes wave output from the EOM has a DC component. In reality, when the system is turned on, the EOM outputs an optical signal, i.e. a DC component is already there before the pulse goes into the fiber. So a time delay t_0 (setting of this parameter is discussed in the next section) is required to describe the time difference between the center of the pulse entering the fiber and the DC component starting to enter the fiber at $t = 0$. Thus, the initial condition for the pulsed Stokes field is $E_s(z \neq 0, 0) = 0$. $E_s(z = 0, 0)$ will be defined by the corresponding boundary condition. The boundary condition of the cw pump is as simple as $E_p(L,t) = E_{p_L}$. In the sensing system, although the EOM keeps generating pulses, the repetition rate is set so that only one pulse of the Stokes beam is allowed in the sensing fiber at any one time to avoid confusion from the interaction between the cw pump and other pulses. So in the simulation, one can consider the EOM produces only one pulse, before and after which all are DC components. Accordingly, the boundary condition of the pulsed Stokes field can be given by Eq. 3.3. As an example, for an mth order super Gaussian pulse centered at t_0 created by the EOM with bias set to ϕ_0 and maximum modulated phase difference $\phi_{\max}$ (refer to Section 3.2.2), the boundary condition is

$$\begin{aligned} E_s(0,t) &= \sqrt{\frac{I_{s_{\text{in}}}}{2}}\left(\cos\theta \exp\left\{\mathtt{i}\eta\left[\phi_0 + \phi_{\max} \mathrm{e}^{-\ln 2\left(\frac{t-t_0}{\tau_p/2}\right)^m}\right]\right\}\right. \\ &\quad \left. + \sin\theta \exp\left\{-\mathtt{i}(1-\eta)\left[\phi_0 + \phi_{\max} \mathrm{e}^{-\ln 2\left(\frac{t-t_0}{\tau_p/2}\right)^m}\right]\right\}\right). \end{aligned}$$

4.2.2 Initial noise generation

In solving Eqs. (2.9), an initial thermal noise-induced phonon field Q_0 is taken into account. Hence, the $|Q_0|$ is Rayleigh distributed[51, 52]. Actually, the initial phonon field originates from the thermal vibration of the lattice of the fiber. Consider the two dimensional case; the probability of $|Q_0|$ is

$$P(|Q_0|) \propto |Q_0| \, \mathrm{e}^{-\frac{|Q_0|^2}{k_B T}},$$

where k_B ($1.3806503 \times 10^{-23}$ J/K) is the Boltzmann constant and T is the temperature. Normalization requires the above probability to be

$$P\left(|Q_0|\right) = \frac{2\,|Q_0|}{k_B T} \mathrm{e}^{-\frac{|Q_0|^2}{k_B T}}. \tag{4.15}$$

This is a Rayleigh distribution with width $\sqrt{k_B T/2}$. At this stage we treat this initial phonon field as white noise, that is, totally spatially and temporally uncorrelated. Since phase does not enter the intensity, I assume it is random and uniformly distributed. Such a field can be generated in the following procedure. In general, if x_1, x_2, $\cdots$ are random with a joint probability distribution $p\left(x_1, x_2, \cdots\right) \mathrm{d}x_1 \mathrm{d}x_2 \cdots$, and if y_1, y_2, $\cdots$ are functions of x's, the joint probability distribution of y's is[53]

$$p\left(y_1, y_2, \cdots\right) \mathrm{d}y_1 \mathrm{d}y_2 \cdots = p\left(x_1, x_2, \cdots\right) \left|\frac{\partial\left(x_1, x_2, \cdots\right)}{\partial\left(y_1, y_2, \cdots\right)}\right| \mathrm{d}y_1 \mathrm{d}y_2 \cdots,$$

where $\left|\frac{\partial(x_1, x_2, \cdots)}{\partial(y_1, y_2, \cdots)}\right|$ is the Jacobian determinant. What we need is to generate the Rayleigh distributed phonon field intensities from uniformly distributed random numbers. Then the above equation becomes

$$p\left(|Q_0|\right) \mathrm{d}\,|Q_0| = p\left(x\right) \frac{\mathrm{d}x}{\mathrm{d}\,|Q_0|} \mathrm{d}\,|Q_0|$$

by realizing that $p\left(x\right) = 1$. Hence, by Eq. (4.15) we have

$$\begin{aligned}
\frac{\mathrm{d}x}{\mathrm{d}\,|Q_0|} &= p\left(|Q_0|\right) = \frac{2\,|Q_0|}{k_B T} \mathrm{e}^{-\frac{|Q_0|^2}{k_B T}} \\
&\Longrightarrow \quad x = \int_0^{|Q_0|} \frac{2\,|Q_0|}{k_B T} \mathrm{e}^{-|Q_0|^2/k_B T} \mathrm{d}\,|Q_0| \\
&\Longrightarrow \quad |Q_0| = k_B T \sqrt{-\ln\left(1 - x\right)}.
\end{aligned}$$

With a uniformly distributed random phase φ, $Q_0(z, t)$ is then determined by

$$Q_0(z, t) = |Q_0|\, \mathrm{e}^{\mathrm{i}\varphi}.$$

This noise filed is verified to be indeed Rayleigh distributed and uncorrelated. Since the definition of $\bar{Q}(z,t) = \mathrm{i}g_1 Q(z,t)$ is used to simplify Eqs. (2.8) to Eqs. (2.9), the phonon field noise used in the simulation is:

$$\bar{Q}_0(z,t) = \mathrm{i}g_1 |Q_0| \, \mathrm{e}^{\mathrm{i}\varphi}.$$

Below is the portion of program code of this noise generating procedure in Fortran90.

```
!--Subroutine generating two independent Rayleigh distributed random numbers--
SUBROUTINE Rayleigh_Random(Q, sigma, sc, sameseeds)

COMPLEX(KIND(0.0D0)), DIMENSION(0:Nmax-1), INTENT(OUT) :: &
                      Q            !1-D matrix for the random noise

REAL(8), INTENT(IN), OPTIONAL :: sigma !controlling the max and width.
REAL(8), INTENT(IN), OPTIONAL :: sc    !scale of the noise

LOGICAL, INTENT(IN) :: sameseeds  !flag indicating whether seeds will
      !be the sameas those of previous
        !execution. T = yes, F = no.
INTEGER :: i
REAL(8) :: x1  !uniformly random numbers will be used to generate a
!Rayleigh random numbers
REAL(8), DIMENSION(0:Nmax-1) :: Amp, & !Rayleigh random num array of Amps
    pha    !Uniform random num array of phase
INTEGER :: seed(10)              !seed array

LOGICAL, SAVE :: Iflag = .FALSE. !flag indicating whether the generator
     !is started or not. T = yes, F = no
INTEGER :: Openstatus, InputStatus, OutputStatus

IF (.NOT. Iflag) THEN   !If the generator is not started, then start it
```

```
IF (sameseeds) THEN   !If demand to use the same seeds as those previous

OPEN(UNIT = 15,           &  !Open the file for read
FILE = 'seed.txt',   &  !file stores the seed array
STATUS = 'OLD',      &
ACTION = 'READ',     &
POSITION = 'REWIND', &
IOSTAT = OpenStatus )
IF (Openstatus > 0) STOP 'Cannot open the file'

READ (15, *, IOSTAT=InputStatus) seed
IF (InputStatus > 0) STOP 'Input Error!'

CALL RANDOM_SEED(PUT= seed)  !Initialize the generator with
       !previous seed array.
Iflag = .TRUE.               !set Iflag = ture since the generator
       !now started
ELSE      !If demand to use new different seeds

OPEN(UNIT = 15,            & !open the file for write
FILE = 'seed.txt',    & !file stores the seed array
STATUS = 'REPLACE',   &
ACTION = 'WRITE',     &
POSITION = 'REWIND',  &
IOSTAT = OpenStatus )
IF (Openstatus > 0) STOP 'Cannot open the file'

CALL RANDOM_SEED()     !Initialize the generator with current
      !time and date
```

```
CALL RANDOM_SEED(GET= seed) !Get current seed
CALL RANDOM_SEED(PUT= seed) !Reintialize with this seed array

WRITE (15, *, IOSTAT=OutputStatus) seed  !store the seed array
IF (OutputStatus > 0) STOP 'Output Error!'
Iflag = .TRUE.    !set Iflag = ture cz' the generator is started

END IF

END IF

CLOSE(UNIT= 15)    !close the file

!Get one Rayleigh distributed random arrays represents the Amps
DO i = 0, Nmax-1
CALL RANDOM_NUMBER(x1)   !Get 3 uniformly distributed random nums

!Get corresponding Rayleigh random numbers as the amplitudes
Amp(i) = DSQRT(sigma * DSQRT(- DLOG(1.0d0-x1)))
END DO

CALL RANDOM_NUMBER(pha)  !Generate the array of random phases
pha = pha * 2 * pi           !Range phases from 0 to 2pi

!Get the noise for time j
Q = (0.0d0, 1.0d0) * g1 * CMPLX(amp * COS(pha), amp * SIN(pha), KIND=8)

END SUBROUTINE Rayleigh_Random
!-----------------------------------------------------------------------
```

4.2.3 Parameter setting

In order to compare the simulation results to the experiments, the proper setting of all related physical parameters is important. We consider single mode fibers only. The refractive index is set to be $n = 1.470$ so that the group velocity of light inside the fiber is $v_g = c/n = 0.2041$ m/ns. The input CW pump power in our experiments is about 5 mW, while the peak power of the pulsed Stokes is around 50 mW; our single mode fibers have radii of 5 μm. Thus the input power densities of the two lasers are respectively 6.365529×10^{10} mW/m^2 and 6.365529×10^{11} mW/m^2 (peak power). The attenuation factor is 6.9×10^{-5}/m. The phonon life time is about 10 ns which results in a 500 MHz damping rate. The photon-phonon coupling coefficient g_1 is set to be 100.595 m^{3}ns^{-1}kg^{-1}. The Brillouin gain factor is $g_B = 5 \times 10^{-14}$ m/mW. Room temperature is 295K, at which ν_B for loose single mode fibers is 12795 MHz.

The above parameters are directly taken from the physical properties of the material. Now let us talk about some important parameters relevant to the implementation. As mentioned in previous chapters, a time delay t_0 must be set as the time when the pulse center enters the sensing fiber. The idea is that t_0 must be long enough to ensure that the DC component can at least travel in the fiber for a round trip. This ensures a steady state before the pulse enters, by letting the DC component incident in the fiber before the pulse completely interacts with the cw pump laser. The interaction information at $z = L$ can be carried out by the CW pump at $z = 0$. This is the real situation in experiments, but in the program it can not be too long to increase the execution time. Accordingly, we normally set t_0 to be between $2L/v_g$ and $3L/v_g$. The time for ending the execution should allow the pulse to exit the sensing fiber completely. Experimentally, the time step size is 0.5 ns, since the maximum sampling rate of the digitizer is 2 GHz. We choose to use $\Delta t = 0.1$ ns in the program so that there are a sufficient number of points in a pulse width. Nevertheless, this value is flexible to adapt to different fiber lengths and pulse widths. As a consequence, the spatial interval is simply $\Delta z = v_g \Delta t$.

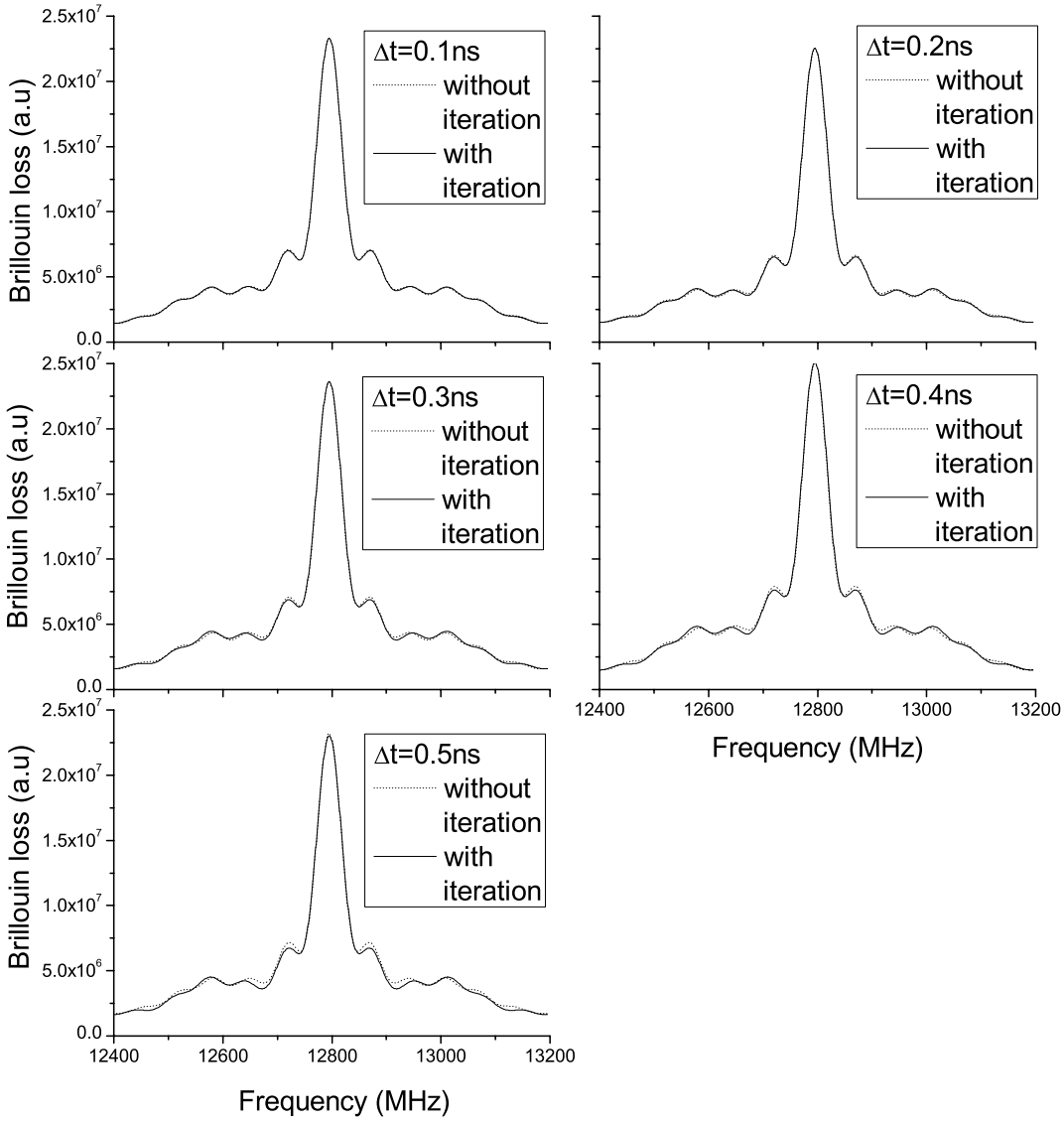

Figure 4.1: Brillouin spectra at the center of a 1m fiber with $\tau_p = 1.5$ns and $R_x = 20$dB comparing the numerical method without iteration and with iteration for respectively (a) $\Delta t = 0.1$ns; (b) $\Delta t = 0.2$ns; (c) $\Delta t = 0.3$ns; (d) $\Delta t = 0.4$ns; (e) $\Delta t = 0.5$ns.

4.3 Improvement on the Numerical method

In Section 4.1, Eqs. (4.9a & 4.9b) are obtained by replacing $\left|E_{s_n}^{m+1}\right|^2$ and $\left|E_{p_n}^{m+1}\right|^2$ with $\left|E_{s_n}^{m}\right|^2$ and $\left|E_{p_n}^{m}\right|^2$ respectively in Eqs. (4.8a & 4.8b), since without this linearization at the first place the numerical method can not proceed. However, this replacement weakens the coupling of the two laser fields and hence the results deviate from the exact solutions. To improve the accuracy of the simulation, we have used an iterative method, as illustrated in the following pseudocode:

For every time index $m+1$

Iteration index I = 1

Obtain $\left(\vec{E}_p^{m+1}\right)_{\mathrm{I}}$ and $\left(\vec{E}_s^{m+1}\right)_{\mathrm{I}}$ by Chu's linearization: $\left|E_{s_n}^{m+1}\right|^2 \approx \left|E_{s_n}^{m}\right|^2$ and $\left|E_{p_n}^{m+1}\right|^2 \approx \left|E_{p_n}^{m}\right|^2$

While the new solutions are not stable, do

I = I + 1

Calculate $\left(\vec{E}_p^{m+1}\right)_{\mathrm{I}}$ and $\left(\vec{E}_s^{m+1}\right)_{\mathrm{I}}$ by letting $\left|E_{s_n}^{m+1}\right|^2 = \left|E_{s_n}^{m+1}\right|_{\mathrm{I}-1}^2$ and $\left|E_{p_n}^{m+1}\right|^2 = \left|E_{p_n}^{m+1}\right|_{\mathrm{I}-1}^2$

End of while loop

End of For loop.

The stability of the solutions is achieved if the field amplitudes are essentially unchanged by an iteration, i.e., $\left|\left(E_{s_n}^{m+1}\right)_{\mathrm{I}} - \left(E_{s_n}^{m+1}\right)_{\mathrm{I}-1}\right| \leq \epsilon_s$ and $\left|\left(E_{p_n}^{m+1}\right)_{\mathrm{I}} - \left(E_{p_n}^{m+1}\right)_{\mathrm{I}-1}\right| \leq \epsilon_p$ for all spatial indices n where ϵ_s and ϵ_p are two small, real-valued numbers. ϵ_s depends on the precision of the calculation and the magnitude of E_s. ϵ_p depends on ϵ_s, since E_p is calculated with E_s by Eq. (4.14). In our case, $|E_s|$ is of the order of 10^6 and double precision computation allows 15 effective digits, so $(\epsilon_s)_{\min} = 1 \times 10^{-9}$. With this, ϵ_p can only be minimized to 0.01 according to simulations, which is still good since $|E_p|$ is of the order of 10^5. ϵ_s also depends on the time interval Δt, because the larger the Δt the coarser the linearization. ϵ_s is found to be 1×10^{-9} when $\Delta t = 0.1$ ns but 1×10^{-8} when $\Delta t \geq 0.3$ns. The maximum number of iterations to reach stability is 4 for $\Delta t = 0.1$ ns.

Fig. 4.1 shows that the difference between the solutions of E_p with and without iterations increases with Δt. The difference between the two methods is more significant for off-resonance frequencies than that for ν_B and frequencies very close to ν_B. This is because the loss of the

cw pump is much greater for $\nu = \nu_B$ than that for $\nu \neq \nu_B$, i.e. $|E_p|$ for $\nu \neq \nu_B$ is much greater than that for $\nu = \nu_B$. Nevertheless, ϵ_s and ϵ_p are limited by $|E_p|_{\max}$. Thus, solutions by the method without iteration are farther from the exact solutions for $\nu \neq \nu_B$ than those for $\nu = \nu_B$. In Chu's paper[1], linearization does not impact his results significantly, since he only simulated the resonant case ($\nu = \nu_B$) for very short fibers (2-25cm) and narrow Δt (0.01-0.05ns). Although there is no visible difference when $\Delta t = 0.1$ ns, as shown in Fig. 4.1(a), this is only one case, by which one cannot guarantee that the difference will be unchanged when changing parameters other than Δt in the simulation. Therefore, it is safer to use the method with iteration.

Chapter 5

Sub-peaks in Brillouin spectra

Pump (cw)-probe (pulsed), Brillouin-based fiber optic sensors have been extensively studied over the past decades, because of their enhanced sensitivity for strain and temperature measurements[26]. In this system, the strain/temperature is measured by the shift in the main Brillouin frequency of the Brillouin loss spectrum as a function of the beat frequency ν of the two counter-propagating lasers. While a single Brillouin peak is usually observed under uniform strain/temperature, multi-peak spectra have also been observed[54] and associated with cross talk effects in non-uniformly strained fibers [55]. These multi-peak Brillouin spectra contain mixed strain/temperature information. Recently, another type of peak, namely sub-peaks, have been observed in the experimental Brillouin spectra for pulse durations of a few ns, even under uniform strain/temperature in fibers, as shown in Fig. 5.1(a)[2]. It is important to study the properties of these sub-peaks because in the field, tests of the structural health monitoring (SHM), the strain and temperature vary from one location to another. If we attribute these sub-peaks to strain/temperature change on civil structures, a false warning signal could be issued. In this thesis, we use the transient coupled wave equations to study the properties and origins of the sub-peaks, enabling us to differentiate these peaks from the strain/temperature peaks. The importance of this study is that it will help us to improve our measurement accuracy at cm spatial resolution, increasing the system capability particularly in SHM applications, where the small stress spot could be detected by subtraction of the initial reference, as the sub-peaks are not functions of strain/temperature or the DC level (the background of the pulsed probe).

There are two origins of the sub-peaks: 1) the periodic damping oscillation (off-resonance oscillation) of the cw pump intensity when the beat frequency ν does not match the Brillouin frequency ν_B of the sensing fiber and 2) the Fourier spectrum of the pulsed probe. The frequency of this off-resonance oscillation is identical to $|\nu - \nu_B|$.

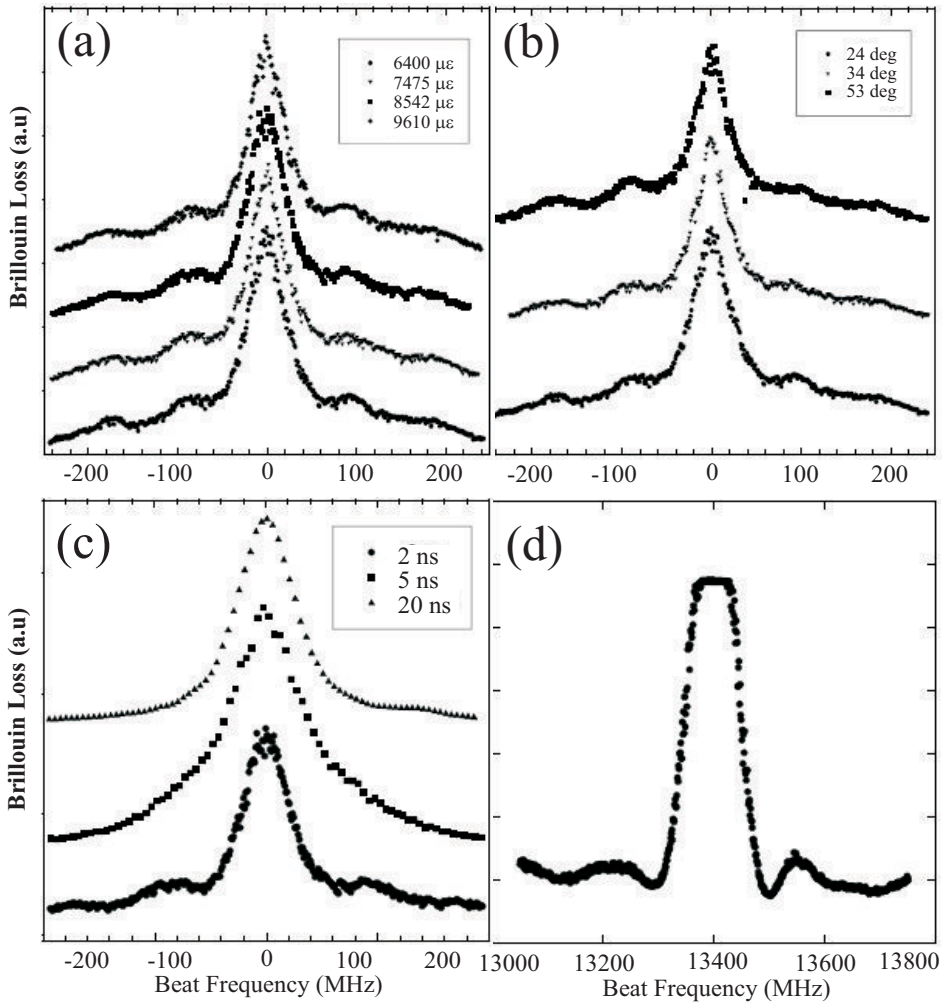

Figure 5.1: (a)Brillouin spectra taken at different strain. (b) Brillouin spectra taken at different temperature. (c) Brillouin spectra taken at pulse widths of 2, 5 and 20 ns. (d) Brillouin spectra taken with a 10 ns pulse and increased receiver sensitivity; the flat top is due to electrical chop off. (Thanks A. Brown for these figures[2].)

Since a push-pull Mach-Zehnder EOM is used in this chapter, θ and η are assumed to be $\pi/4$ and 0.5 respectively for the pulsed probe field in Eq. (3.3). A Brillouin spectrum is obtained by plotting the Brillouin loss versus the scanned beat frequencies (ν) at a fixed temporal interval

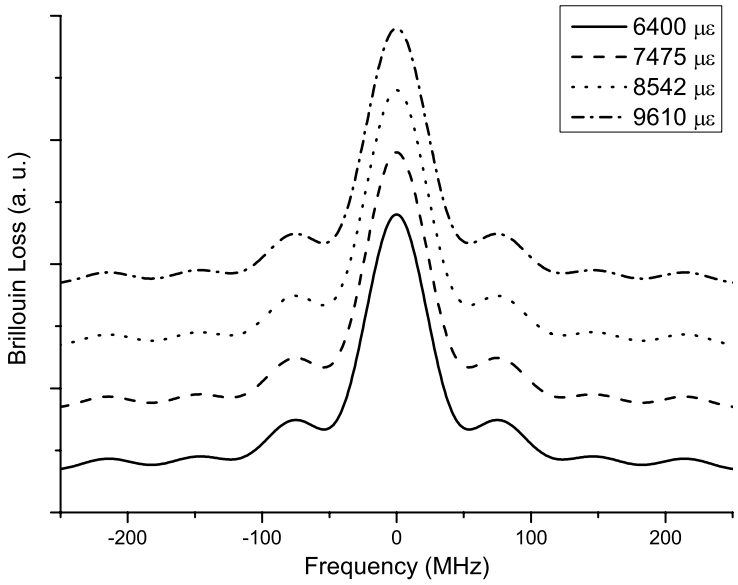

Figure 5.2: Simulated Brillouin spectra taken at different strain. All spectra are shifted to zero central frequency for comparison.

in the time domain, while a Brillouin time domain is taken at a fixed beat frequency.

Compared to Fig. 5.1(a), Fig. 5.2 shows that the positions of the sub-peaks are independent of the strain on the fiber and hence we can exclude the possibility that this material property being a reason for change. Actually, the strain and temperature change only the Brillouin frequency linearly by the relations $\Delta\nu_B = c_\varepsilon \Delta\varepsilon$ and $\Delta\nu_B = c_T \Delta T$ respectively[23]. Hence, the strain/temperature change can be simulated by a corresponding shift in the main Brillouin frequency.

5.1 First origin: Fourier transform of the pulse

Eq. (2.9c) shows that the Brillouin spectrum is a convolution of the gain profile and the Fourier spectrum of the pulsed probe. Or equivalently, since a spectrum is obtained by looking at the frequency domain at a fixed position in the Brillouin time domain, the interaction between the cw pump and pulsed Stokes at a spatial position turns the cw pump intensity at that position into a pulse in the time domain, as shown in Fig. 5.3. This indicates that the Brillouin spectrum will have sub-peaks from the Fourier transform of the pulse. To verify this, the pulsed Stokes

beam can be considered as a pure pulse in order to get rid of impacts from the DC component. Figs. 5.4 shows the Fourier transform of a 20the-order super Gaussian pulse with FWHM = 6 ns. One can see three peaks within 700 MHz on each side of the central peak.

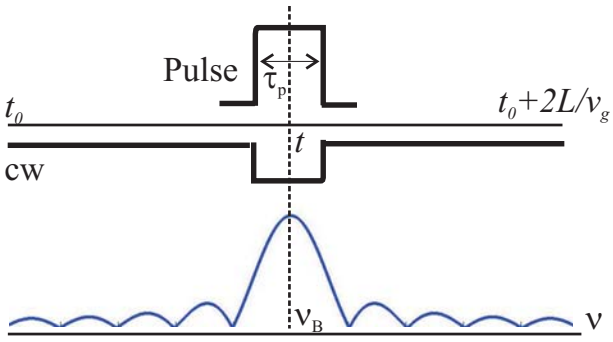

Figure 5.3: Fourier spectrum of the instantaneous pulse.

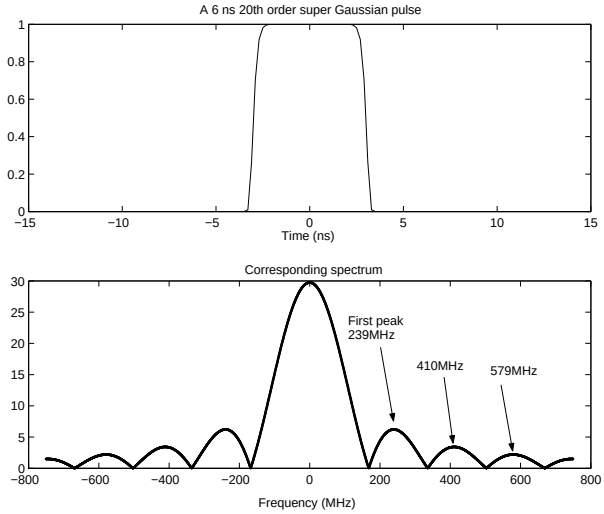

Figure 5.4: Fourier spectrum of a 6 ns, 20th order Super Gaussian pulse.

Fig. 5.5(a) illustrates the Brillouin spectra at the centers of fibers of lengths 2, 4 and 8 meters respectively when using the same pulse. One is able to identify the correspondence of the sub-peaks in the Brillouin spectra to those in Fig. 5.4. One also finds that the positions of these sub-peaks are not sensitive to the fiber length. This is true because the fiber length is not involved in this mechanism. The interesting thing is that the position of each sub-peak in Fig.

5.5(a) is closer to the central peak than that of its counterpart in Fig. 5.4. This is due to the impact of the gain profile $g(\nu)$ in that the Brillouin spectrum is a convolution of the gain profile $g(v)$ and the Fourier transform of the pulse. $g(\nu)$ can be obtained analytically in the steady state[43, 56]. Unfortunately, in this general case, the exact form of the convolution cannot be found, since the model is not analytically solvable. However, this shift of the peaks is related to the pulse width. As an illustration, in Fig. 5.5(b) we plot the effect of pulse width on the difference between the first sub-peak positions in the Fourier spectrum and the corresponding Brillouin spectra.

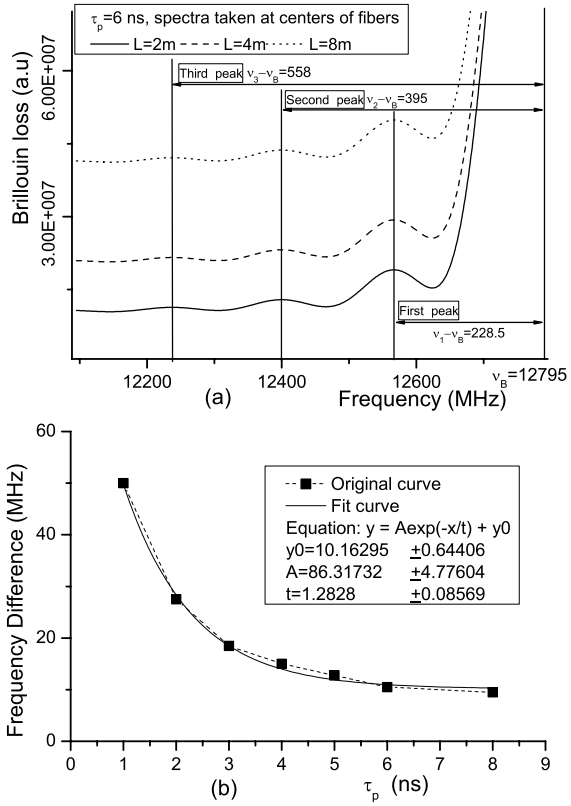

Figure 5.5: (a) compares the Brillouin spectra of fibers 2, 4 and 8 meters long using the same pulse. (b) illustrates the relation between pulse width and the difference between positions of the first side peak in Brillouin spectrum and of that in the Fourier spectrum of the pulse.

Now that we have shown how sub-peaks originate from the Fourier transform of the pulse, they should be subject to not only the pulse width but also the pulse shape. In the simplest case where a pure Gaussian pulse is used, there are no sub-peaks at all in the Brillouin spectra,

since the Fourier transform of a pure Gaussian pulse in the time domain is still a pure Gaussian pulse in the frequency domain. This is shown in Fig. 5.6(a). Fig. 5.6(b), which compares the spectra of 4the through 10the order super Gaussian pulses with the same FWHM as above, tells us that as the order of the pulses decreases, positions of the sub-peaks shift closer and closer to the central peak and the heights of the peaks decline. This is consistent with the mechanism of the Fourier transform. Although the Fourier spectrum of the pulse results in sub-peaks in the Brillouin spectra, most of the sub-peaks should not come directly from this reason. Because the pulse widths used in experiments are normally around 2 ns. Sub-peaks in these cases are very far away from the central peak and are out of our frequency scanning range. However, in Fig. 5.1(d) where a 10 ns pulse is applied, the positions of the sub-peaks match well with the peaks in the Fourier spectrum of such a pulse. We conclude therefore that these sub-peaks are due, at least partly, to the Fourier spectrum of the pulse.

Using the same conditions as above, when changing the time t or equivalently the spatial position z where the Brillouin spectrum is taken, one is not supposed to see any shift of the positions of the sub-peaks. However, exceptions can occur when $t_0 < t < t_0 + \tau_p/2$ and $t_0 + 2Ln/c - \tau_p/2 < t < t_0 + 2Ln/c$ since in either case only a partial pulse interacts with the cw pump beam; hence the Fourier sub-peaks generated in the Brillouin spectra are farther from the main Brillouin peak than those in the Brillouin spectra taken at time $t_0 + \tau_p/2 < t < t_0 + 2Ln/c - \tau_p/2$. Taking the case when $t_0 < t < t_0 + \tau_p/2$ as an example, as t increases in this region, the instantaneous pulse becomes wider and wider from $\tau_p/2$ to τ_p. Thus the Fourier sub-peaks in a Brillouin spectrum at some time t in this region become closer to the central peak than that in another spectrum taken at time $t_1 > t$ in this region.

Consider a Stokes beam having no pulsed part, i.e., it is a cw wave as well. The Brillouin spectrum is shown in Fig. 5.7, where one sees some small peaks very close to the central peak. It is obvious that these peaks do not come from the Fourier transform. But where do they come from? The next section will uncover the origin. In our setup of the Brillouin sensor, an Electro-optic Modulator (EOM) is used to generate a light beam composed of both a pulsed and a DC components. Therefore, sub-peaks could originate from a combination of several factors.

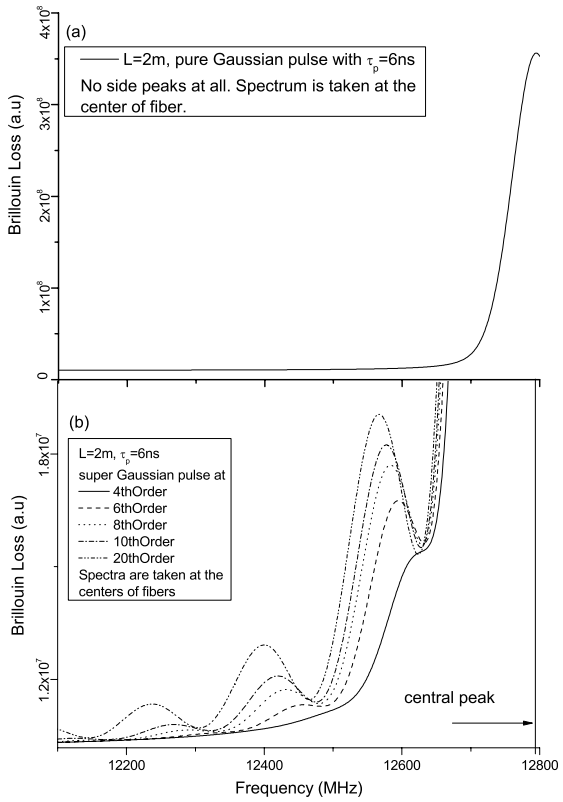

Figure 5.6: (a) is the Brillouin spectrum obtained when using a pure Gaussian pulse and no side peaks at all. (b) compares the Brillouin spectra when using super Gaussian pulses at different orders but the same FWHM.

5.2 Second origin: Off-resonance oscillation

As mentioned in the introduction and indicated in Eqs. (2.9), the cw pump and pulsed Stokes beams interact through an induced phonon field inside the fiber, which has the same frequency as the beat frequency of the two lasers. The phonon field at any position should behave in a similar way to the loss signal of the cw pump at the same position. That is, the spectra of the phonon field at $z = 0$ should also have sub-peaks at the same positions as those of their counterparts in the Brillouin spectra, since the cw pump is detected at $z = 0$. Now from Eq. (2.9c) one can easily write down the general solution of this phonon field $\bar{Q}$ as

$$\bar{Q}\,(z,t) = \frac{1}{2}\Gamma_1 g_B \mathsf{e}^{-\Gamma t} \int_0^t E_p(z,t') E_s^*(z,t') \mathsf{e}^{\Gamma t'} \mathsf{d}t',$$

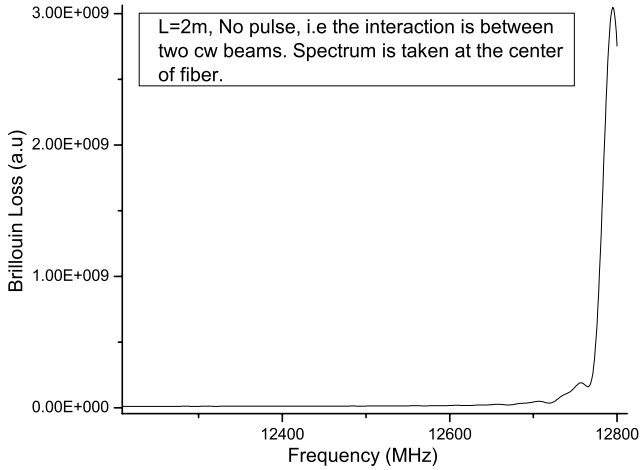

Figure 5.7: Calculated Brillouin spectrum when the Stokes beam is also a cw wave.

where the initial noise phonon field is neglected for qualitative analysis. By setting $z = 0$ in the above equation one obtains

$$\bar{Q}(0,t) = \frac{1}{2}\Gamma_1 g_B \mathsf{e}^{-\Gamma t} \int_0^t E_p(0,t') E_s^*(0,t') \mathsf{e}^{\Gamma t'} \mathsf{d}t'. \tag{5.1}$$

$E_s^*(0,t)$ is given by Eq. (3.2) and let $\theta \approx \pi/4$ and $\eta \approx 0.5$ since the our EOM has a maximum extinction ratio of 28dB. Thus we have

$$E_s(0,t) = \sqrt{I_{s_{\text{in}}}} \cos \frac{\phi(t)}{2}, \tag{5.2}$$

with $\phi(t) = \phi_0 + \phi_{\max} \times \textit{pulse shape}$. Taking the setting in Section 3.2.2 where $\phi_0 = \pi + \Delta\phi$ and $\phi_{\max} = \pi/2$ and considering a positive pulse shape function $f(t, t_0, \tau_p) \leq 1$; denoting a symmetric pulse with width τ_p centered at t_0 (e.g., $f(t, t_0, \tau_p) = \exp\{-\ln 2 [2(t - t_0)/\tau_p]^m\}$ is a m-th order super Gaussian pulse), Eq. (5.2) becomes

$$E_s(0,t) = -\sqrt{I_{s_{\text{in}}}} \sin \left\{ \frac{\Delta\phi}{2} + \frac{\pi}{4} f(t, t_0, \tau_p) \right\}.$$

For super Gaussian pulses (the most common case in experiments), since $f\left(t,t_0,\tau_p\right)=0$ when $|t-t_0|\gg\tau_p/2$ the above equation can be approximated as

$$\begin{aligned} E_s(0,t) &\approx -\sqrt{I_{s_{\text{in}}}}\left[\sin\frac{\Delta\phi}{2}+\frac{\sqrt{2}}{2}\left[\cos\frac{\Delta\phi}{2}-\left(\sqrt{2}-1\right)\sin\frac{\Delta\phi}{2}\right]f\left(t,t_0,\tau_p\right)\right] \\ &= E_{DC}+E_{S_0}f\left(t,t_0,\tau_p\right), \end{aligned} \tag{5.3}$$

where

$$\begin{aligned} E_{\mathtt{DC}}\left(t\right) &= -\sqrt{I_{s_{\text{in}}}}\sin\frac{\Delta\phi}{2} \\ E_{S_0}\left(t\right) &= -\sqrt{I_{s_{\text{in}}}}\left[\cos\frac{\Delta\phi}{2}-\left(\sqrt{2}-1\right)\sin\frac{\Delta\phi}{2}\right] \end{aligned} \tag{5.4}$$

can be considered as the fields of the DC and pulse components of the pulsed Stokes laser beam. Notice that for square pulses, the approximation sign in the above equation should be replaced by an equal sign. Plugging Eq. (5.3) into Eq. (5.1) and normalizing Eq. (5.1) yields the intensity of the acoustic field:

$$\begin{aligned} &\left|\bar{Q}\left(0,t\right)\right|^2= \\ &\frac{1}{4}\Gamma_1^2g_B^2\mathtt{e}^{-2\Gamma_1 t}\left\{\underbrace{\left|E_{\mathtt{DC}}\right|^2\left|\int_0^t E_p(0,t')\mathtt{e}^{\Gamma t'}\mathtt{d}t'\right|^2}_{\texttt{Term 1}}+\right. \\ &\underbrace{2\Re\left[E_{\mathtt{DC}}^*E_{S_0}\int_0^t E_p(0,t')\mathtt{e}^{\Gamma t'}\mathtt{d}t'\int_0^t E_p^*(0,t')\mathtt{e}^{\Gamma^* t'}f\left(t,t_0,\tau_p\right)\mathtt{d}t'\right]}_{\texttt{Term 2}} \\ &\left.\underbrace{+\left|E_{S_0}\right|^2\left|\int_0^t E_p(0,t')\mathtt{e}^{\Gamma t'}f\left(t,t_0,\tau_p\right)\mathtt{d}t'\right|^2}_{\texttt{Term 3}}\right\}. \end{aligned} \tag{5.5}$$

There are three terms in Eq. (5.5). Before studying them individually, recall that $\Gamma=\Gamma_1+\mathrm{i}\Gamma_2$, $\Gamma_1=\frac{1}{2\tau}$ and $\Gamma_2=2\pi\left(\nu-\nu_B\right)$. Then it is obvious that when $\nu\neq\nu_B$, i.e. when the beat frequency of the two laser beams do not match the Brillouin frequency, all three terms oscillate in the time domain of the phonon field and hence in the loss signal of the cw pump beam. Together

with the coefficient $\frac{1}{4}\Gamma_1^2 g_B^2 \mathsf{e}^{-2\Gamma_1 t}$, it should be a damped oscillation. If this damped oscillation does exist, its frequency, hereafter called the off-resonance frequency, should be identical to $|\nu - \nu_B|$. However, the three terms may not play their important roles simultaneously. In the usual case when the pulsed Stokes beam has both DC and pulse components, Term 2 and Term 3 are significant only within a small temporal region $(t_0 - \tau_p/2, t_0 + \tau_p/2)$ (call it region A) since $f(t, t_0, \tau_p)$ vanishes rapidly out of this region. Out of region A, only Term 1 is finite. Thus in order to analyze the effects purely from Term 1, we should only consider the data after $t_0 + \tau_p/2$ and before $t_0 + 2Ln/c$, since the latter is the time when the center of pulse exits the fiber. In fact, one should better consider the region between $(t_0 + \tau_p/2, t_0 + 2Ln/c - \tau_p/2)$ (call it region B) because within this region the pulse is totally inside the fiber and boundary effects can be neglected. The only caution is, one may lose the interaction information in regions $(t_0, t_0 + \tau_p/2)$ and $(t_0 + 2Ln/c - \tau_p/2, t_0 + 2Ln/c)$. This is one of the reasons why in reality we use very short pulses. So the widths of regions A and B, namely w_A and w_B are about τ_p and $2Ln/c - \tau_p$ respectively; nevertheless, their precise values may vary a bit depending on the order of the super Gaussian pulse.

Fig. 5.8 is an illustration of the effective regions of the three terms and the off-resonance oscillation originating only from Term 1. In Fig. 5.8(a), we compare the time domains at frequencies 12395 MHz, 12775 MHz and 12795 MHz (ν_B) respectively. In this case, region A is $(14, 16)$ ns and region B is $(16, 23.8)$ ns. One can see that the cw pump starts to deplete long before $t_0 - \tau_p/2$ because of the existence of the DC component, which also interacts with the cw pump beam. To view the off-resonance oscillation, we magnify region B of the time domain at $\nu = 12395$ MHz, since this frequency is far enough from the central frequency that full periods of oscillations can be seen in this region. One can see clearly that the expected off-resonance oscillations do appear and have a period of 2.5 ns which exactly matches $\nu - \nu_B = 400$ MHz. One does not find such oscillation in the time domain at 12775 MHz because the corresponding oscillation period, 50 ns is too big to be seen in region B which is only 7.8 ns wide. A spectrum is obtained by taking the Brillouin loss signal of the cw pump power at the same fixed time interval in the time domain of every scanned beat frequency, so the off-resonance oscillation should cause ripples in the spectrum so obtained. Peaks of these ripples belong to a new kind of sub-peak other than those from the Fourier transform discussed in the last section. Fig. 5.9

shows that this argument is indeed true. Fig. 5.9(a) presents the spectrum at $t = 21$ ns, which corresponds to a position close to the fiber center. It is convenient to choose the sub-peak at $\nu = 12585$ MHz, because this frequency is far enough from ν_B to produce visible periods in its time domain. Fig. 5.9(b) compares the time domain at 7 frequencies within the neighborhood of 12585 MHz. At $t = 21$ ns, among the intensities of all the 7 frequencies, the one at 12585 MHz is the minimum, representing the strongest depletion in the cw pump power and hence results in the sub-peak at this frequency in the spectrum at 21 ns.

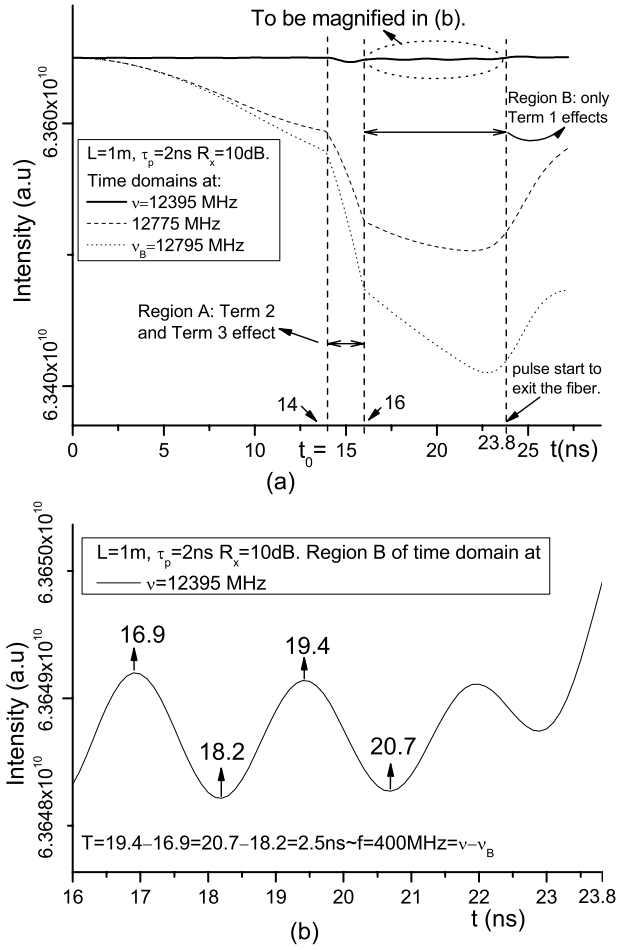

Figure 5.8: (a) shows the time domain of a 1m fiber for $\tau_p = 2$ns, $R_x = 10$dB and at beat frequencies of 12395 MHz, 12775 MHz and 12795 MHz. (b) is the magnification of region B in (a) at the off-resonance frequency of 12395 MHz.

We now switch to Term 3. To avoid the impacts of Term 1 and Term 2, consider the pulsed

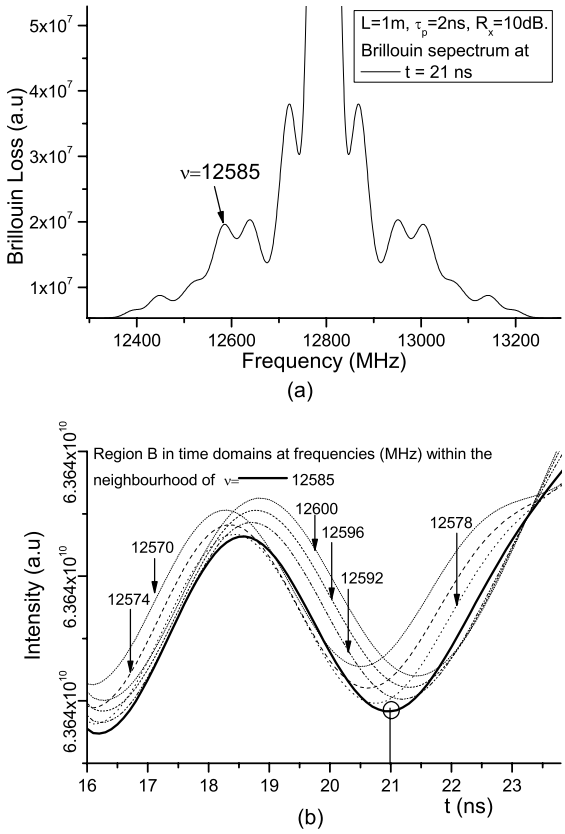

Figure 5.9: (a) picks out a side peak at 12585 MHz in the spectrum at $t = 21$ ns. (b) shows that this side peak is indeed generated by the off-resonance oscillation in the time domain at frequencies within the neighbourhood of 12585 MHz.

probe beam to be a pure pulse, i.e. without a DC component. Then, by Eq. (5.5), Term 1 and Term 2 are set to 0 since $E_{\mathtt{DC}} \equiv 0$ in this case. Therefore one expects to see a number of off-resonance oscillations in region A but not region B. We again choose to simulate with the same parameters used in dealing with Term 1 except that $R_x = \infty$ indicating $E_{\mathtt{DC}} \equiv 0$. Since $\tau_p = 2$ ns, in order to see full periods of oscillations in region A, we need to choose a frequency sufficiently far from the Brillouin frequency, say 11795 MHz. Fig. 5.10(a) compares the time domains at 11795 and 12795 MHz. The cw pump beam does not deplete before $t_0 - \tau_p/2$ due to the absence of a DC component from the pulsed Stokes beam. As a magnification of regions A and B in Fig. 5.10(a), Fig. 5.10(b) shows that there is indeed no significant oscillation in

regions B and the oscillation frequency in region A exactly matches the corresponding frequency difference $\nu - \nu_B$. This reinforces our analysis in the last paragraph, in that Term 3 has no impact in region B and hence region B is only affected by Term 1. There is no doubt that off-resonance oscillations in region A can also produce sub-peaks in the Brillouin spectra at times within region B by the same argument as in dealing with Term 1. Nevertheless, when using very short pulses, region A is sufficiently narrow so that only the oscillations from off-resonance frequencies far from the Brillouin frequency can substantially appear. In addition, the depletion in cw pump beam at this far frequency is very small, so that the relative heights of the sub-peaks are too small to be seen in experimentally obtained spectra in region A.

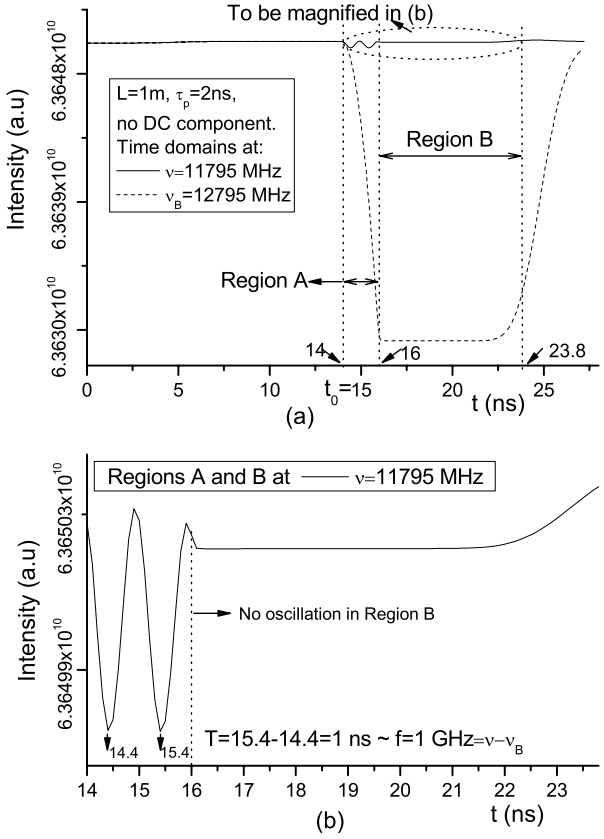

Figure 5.10: (a) shows the time domain of a 1m fiber for $\tau_p = 2$ns, $R_x = \infty$ and at beat frequencies of 11795 MHz and 12795 MHz. (b) shows regions A and B at 11795 MHz.

Obviously, the effect of Term 2 is also largely limited in region A, similarly to Term 3. However, Term 2 does not contribute to region A alone, instead it always goes with Term 3.

Fortunately, according to basic trigonometric algebra, since the two integrals in Term 2 involve off-resonance oscillations at the same frequency as that of Term 3, the final resultant oscillation frequency should be the same as that from Term 1 and Term 3. The only apparent difference is that the amplitude of the oscillation in this case should be stronger than those in previous cases. Fig. 5.11 compares the time domains at 11795 MHz with $R_x = 10$ dB and no DC component respectively. One can see in this figure that the oscillation frequency in region A with $R_x = 10$ dB, which is the same as that in region A with no DC component, is exactly the frequency difference $\nu - \nu_B = 1$ GHz. Also, the amplitude of the former is higher as predicted. In region B, the DC component produces oscillations at the same frequency.

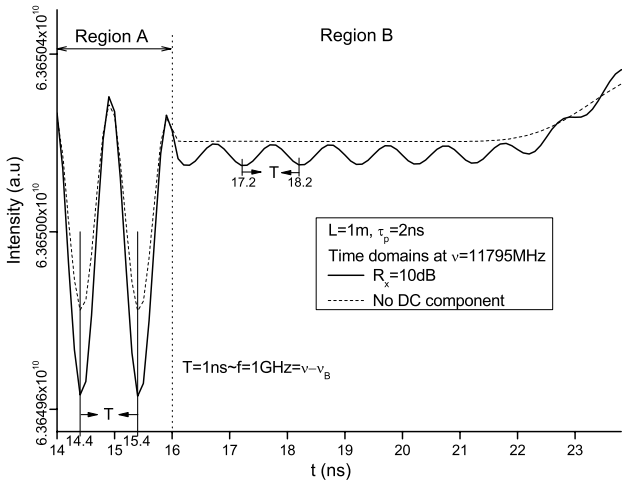

Figure 5.11: Regions A and B at 11795 MHz for respectively 10dB extinction ratio and no DC component.

5.3 Features of sub-peaks

At this stage, one may wonder about the special features of the sub-peaks from these two origins. Applications of their features will probably be found by further studies. In Section 5.1, we already discussed positions and heights of the sub-peaks from the Fourier transform by illustrating the impacts of the pulse width and shape. In this section, properties of sub-peaks from the off-resonance oscillation are considered. For proper pulse widths and the range of

frequency scanning, competition between the two mechanisms of sub-peak formulation occurs.

5.3.1 Frequency region excluding the sub-peaks.

One may ask if the off-resonance oscillation always generates sub-peaks in the spectra. The answer is no. It is the crossing of the oscillations in time domains at different frequencies and amplitudes which leads to the ripples in the Brillouin spectra. However, this crossing does not always happen. We consider region A for a pulsed Stokes beam without a DC component to explain why. Fig. 5.12 compares the intensity curves at four frequencies starting from 12295 MHz in region A. One can see in this figure that the four intensity curves do not cross, on the contrary they are perfectly ordered. Actually, intensity curves at frequencies higher than 12295 MHz never intersect in region A so that the ripples and hence the sub-peaks cannot appear in the frequency range from 12295 to 12795 MHz and the range from 12795 to 13295 MHz as well by symmetry. The key to this phenomenon is the frequency of 12295 MHz, which differs from the Brillouin frequency by 500 MHz. This difference indicates that the period of off-resonance oscillation in any time domain at frequencies higher than 12295 MHz is always greater than 2 ns, such that region A can only hold no more than one period of off-resonance oscillation and this period must be a valley since approximately a new period of oscillation always starts at the beginning of region A and the cw pump is depleting. In this situation, intensity curves are definitely perfectly ordered because the higher the frequency, the larger the oscillation period and the less the depletion. Thus in general, sub-peaks do not show up in the frequency range $(\nu_B - 1/w_A, \nu_B + 1/w_A)$ in spectra taken at temporal positions within region A.

With a reasonable modification, this analysis can be extended to the whole temporal length of the fiber when a DC component is present. Although we expect similar phenomenon to happen in region B, the connection of regions A and B can also result in crossing among the intensity curves. Besides, when the fiber length is fixed, the widths of regions A and B are still a function of the pulse widths and shapes. These factors imply that even if sub-peaks disappear in the spectra taken at temporal points in region A, they can still appear in the spectra taken within region B. Therefore, a stronger condition is needed to exclude the sub-peaks in some range in a spectrum taken at any position along the fiber. The best case is when region A or

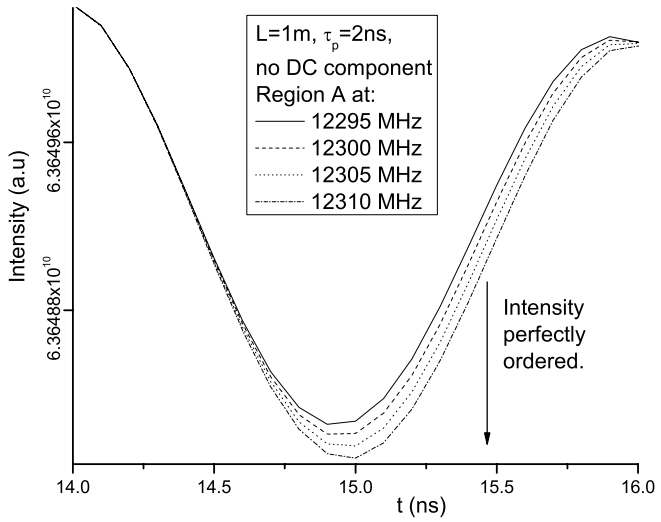

Figure 5.12: No intersecting happens in region A at frequencies after 12295 MHz.

B alone occupies the whole time domain. In such a situation, the same condition as in the last paragraph can be applied. The worst case is when regions A and B each occupy half of the time domain respectively. Then, regarding the transition between these two regions, a reasonable modified condition is that the time domain of the whole fiber (between t_0 and $t_0 + 2Ln/c$) at frequencies within a range $(\nu_B - \Delta\nu, \nu_B + \Delta\nu)$ can hold no more than a half period of the oscillation. Sub-peaks vanish in this frequency range in any spectrum taken along the fiber. It follows that the relation between fiber length and frequency range is

$$4Ln/c = 1/\Delta\nu. \tag{5.6}$$

For example, Eq.(5.6) determines $\Delta\nu = 51$ MHz for a 1 m fiber. Fig.5.13 verifies this statement in that intensity curves at frequencies lower than 12744 MHz still intersect but the curves at frequencies higher than 12744 MHz never intersect and hence generate no sub-peaks between 12744 and 12846 MHz in the Brillouin spectra.

One may worry about the sub-peaks caused by the Fourier spectrum of the cw pump beam. However, Eq. (5.6) tells us that the longer the fiber the smaller the $\Delta\nu$. Furthermore, the Fourier peaks are not related to the fiber length and it even takes a 30 ns pulse to produce the first order Fourier peak around 50 MHz from the central peak. In experiments however only

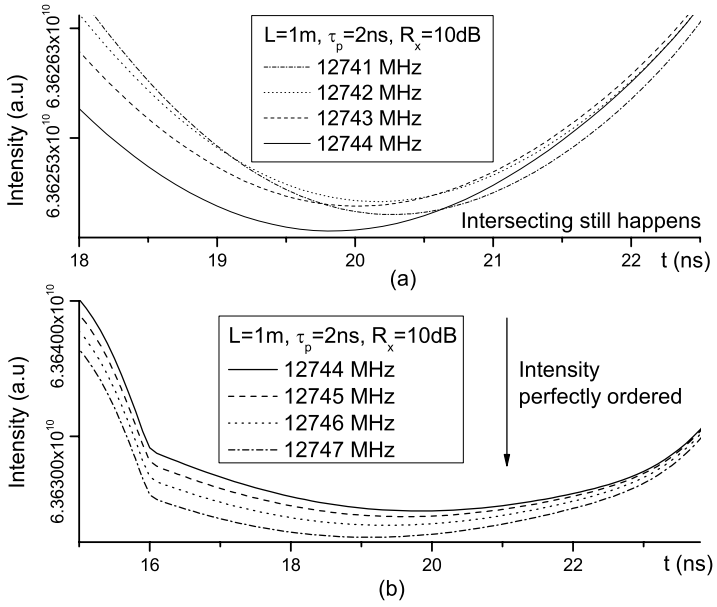

Figure 5.13: (a) shows that intersecting still happens among the time domains at frequencies before 12744 MHz. (b) illustrates the perfectly odered intensities of time domains at frequencies greater than 12744 MHz.

short pulses are used. In addition, a sub-peak may be absorbed into the central Brillouin peak and becomes invisible because the central peak has a certain width, but this can only widen the range $\Delta\nu$. Therefore, in practise Eq. (5.6) can be considered as a lower limit for all kinds of sub-peaks regardless of the pulse width.

5.3.2 Effect of the position inside the fiber where the Brillouin spectrum is taken.

Suppose the peak positions can be identified by equating the partial derivative of Eq. (5.5) with respect to ν to 0. It is apparent that the final equation will couple t and $(\nu - \nu_B)$ together, i.e. the solution for ν must be related to t which is the position where the Brillouin spectrum is taken. It is not good to allow t to change across region A and region B since region A involves the impact of the pulse width. So we only consider very short pulses to narrow region A and take the Brillouin spectra at a number of ascendingly sorted t's in region B. Upon this, what will happen? Because of the one to one correspondence between t and z mentioned in the

introduction, Eq. (5.6) can be generalized by replacing its left hand side by $2t$ which gives

$$2t = 1/\Delta\nu, \qquad t_0 < t < 2Ln/c. \tag{5.7}$$

This means in a fixed range of frequency, the number of sub-peaks should increase in Brillouin spectra taken consecutively at ascendingly ordered t's. Equivalently, if one always names the sub-peak closest to the central peak the first sub-peak and names the remaining of the sub-peaks as they are ordered, one should see that the positions of all the peaks shifts to the central peak as t increases but they can never enter the region determined by Eq. (5.6).

5.3.3 Impact of the DC component.

The magnitude of the DC component plays only the role of coefficients of the terms in Eq. (5.5), so the amount of the DC component in the pulsed Stokes beam, i.e. the extinction ratio R_x should not impact the positions of the sub-peaks in Brillouin spectra taken at the same temporal position but with different extinction ratios. However, this extinction ratio has effects on the height of the sub-peaks. It is more appropriate to analyze the relative height of the sub-peaks to the central peak. This relative height is defined as $h_i = 10\lg(y/y_i)$, where y is the absolute height of the main peak, while y_i is the absolute height of i-th sub-peak in the spectrum. The variation of the extinction ratio changes the relative amount of the DC component and hence impacts the total interaction between the pulsed Stokes and cw pump lasers that determines the height of the central Brillouin peak. On the other hand, R_x affects the off-resonance oscillations via their amplitudes but not their frequencies. However sub-peaks come from the crossing among the oscillating intensity curves in the time domain and the interaction between the two lasers is already much weaker at off-resonance frequencies than that at ν_B, so the impact of R_x on the absolute height of sub-peaks is much smaller than on the central Brillouin peak. Therefore, in the Brillouin spectrum taken at some fixed temporal interval, as R_x increases (i.e. less DC component), when pulse width and fiber length are fixed, the relative heights increase (i.e. h_i's decrease). To verify these conjectures, two considerations must be taken: the Brillouin spectra should be taken at a temporal interval within region B to avoid interference from the pulse and short pulses should be used so that the Fourier peaks are

far from the main peak. As an example, Fig. 5.14(a) shows that the positions of the sub-peaks do not change with R_x, and (b) illustrates that the relative heights of the sub-peaks indeed grow (i.e., h_i decreases) with the increase of R_x by taking the data of the first and second sub-peaks from (a). One may notice in Fig. 5.14(a), that the sub-peaks in the spectrum when $R_x = 30$ dB (i.e. very small DC component) are almost flattened and can hardly be considered as peaks. This is because when the amount of DC component is very small, off-resonance oscillations in region B governed by the DC component are too weak to generate very significant ripples in the spectra. This is also why in Fig. 5.14(b), the second sub-peak does not appear when $R_x = 30$ dB and actually only the first sub-peak is detectable in this case. More generally, when $R_x = \infty$ which means no DC component, there is no significant oscillation in region B, as shown in Fig. 5.11 and hence no sub-peaks at all in the Brillouin spectrum taken in region B.

5.3.4 Impact of the pulse width.

For every time domain of the cw pump beam for some fixed beat frequency, the pulse width only affects the w_A and w_B. If the pulse width gets wider, region A is also wider and more periods of oscillation can be seen in region A. Thus if we exam in time domains for a range of consecutive frequencies, more crossings of the intensity curves can happen in region A due to the increase of w_A with the increase of pulse width. Hence, the pulse width should have no impact on the peak positions in the spectra taken at temporal points always existing in region A during the change of pulse width. Recall our approximation in Eq. (5.5), only Term 1 contributes to region B. This is to say, although the pulse width affects the size of region B, sub-peak positions do not change in the Brillouin spectra taken at temporal positions which always belong to region B regardless of the change of pulse width. But an exception must be noted: when the temporal positions are too close to region A, sub-peak positions may be influenced by the pulse width because although $f(t', t_0, \tau_p)$ in Terms 2 and 3 vanishes rapidly it does not become exactly zero at $t_0 + \tau_p/2$ and has a little longer effect depending on the order m. Fig. 5.15(a) compares eight Brillouin spectra from a 1 meter fiber for pulse widths from 0.5 through 4 ns respectively. They are taken at 16.2 ns, which belongs to region B when

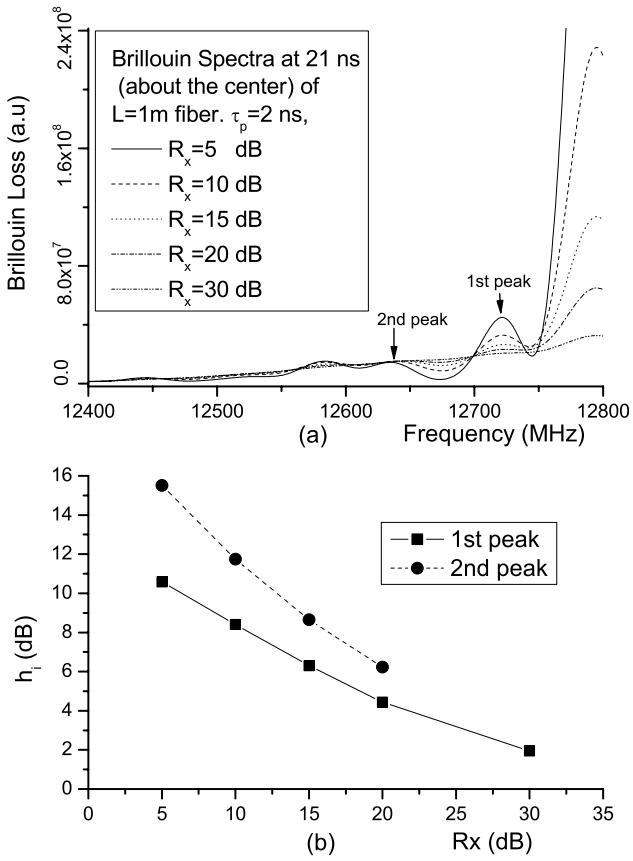

Figure 5.14: (a) shows that positions of the side peaks are not subject to the extinction ratio. (b) illustrates the relation between R_x and h_i by taking the numerical values from (a).

$\tau_p \leq 2.2$ ns and to region A when $\tau_p > 2.2$ ns. As expected, one can see in this figure, the first sub-peak position shifts a bit to the right when the pulse width changes from 0.5 ns to 2.0 ns since 16.2 ns is too close to region A although it is still in region B. Nonetheless, when the pulse width changes from 2.5 to 4.0 ns, the sub-peak positions do not change any more because 16.2 ns becomes a point in region A. As a comparison, Fig. 5.15(b) verifies that in the Brillouin spectra taken at temporal points far from region A (in this case 21 ns), sub-peak positions are not affected by the change of pulse width, and the relative heights of the sub-peaks increase as the pulse width increases.

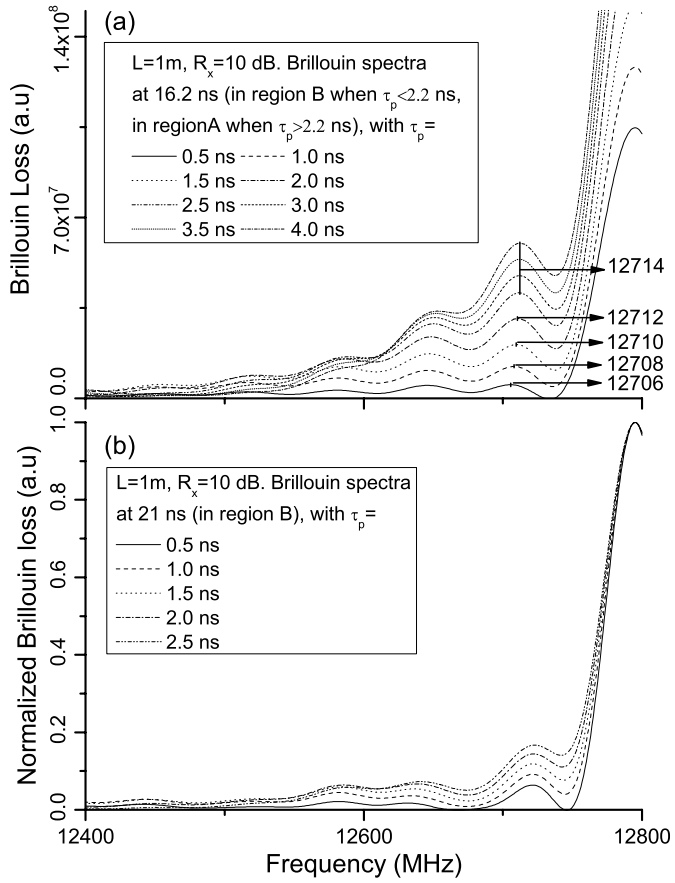

Figure 5.15: (a) Brillouin spectra for $\tau_p = 0.5$, 1, 1.5, 2, 2.5, 3, 3.5 and 4 ns. (b) Normalized Brillouin spectra for $\tau_p = 0.5$, 1, 1.5, 2 and 2.5 ns.

5.3.5 Combined effect of the off-resonance oscillation and the Fourier transform.

Now, let us think about the situation where the two mechanisms of generating sub-peaks, i.e. Fourier transform of the pulse and off-resonance oscillation compete with each other. In previous discussions, short pulses and a narrow frequency range are chosen so that the Fourier peaks are not involved. Now we widen the pulse width or increase the scanning frequency range to visualize the simultaneous contributions of the two origins of sub-peaks. As indicated by Eq. (5.6), the longer the fiber, the more sub-peaks caused by off-resonance oscillation can be seen in a fixed frequency range. Then it is natural to simulate a longer fiber so that the effects are clearer. To do so, a 2 meter fiber is simulated with a pulsed Stokes laser beam consisting

of a 5 ns pulse and 15 dB DC component. Fig. 5.16 shows the Brillouin spectrum taken at 40 ns (in region B since $t_0 = 30$ ns is chosen in this case.). In this figure, the combined effect is clear in that small peaks from the off-resonance oscillations sit on the sub-peaks caused by the Fourier transform of the pulse.

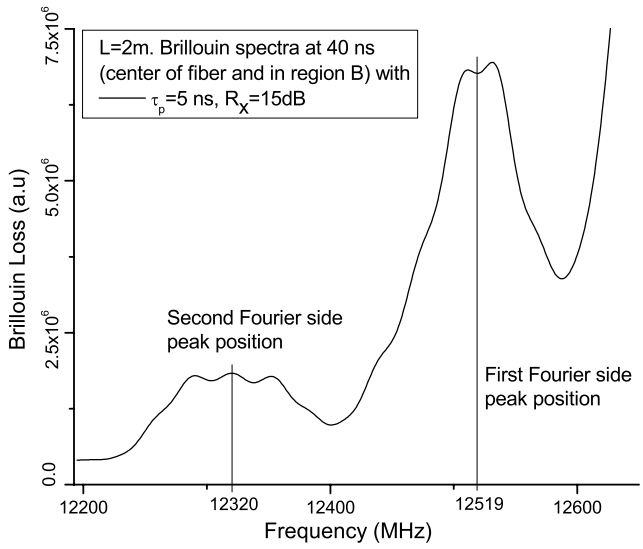

Figure 5.16: Shows the competition between the Fourier peaks and side peaks caused by off-resonance oscillation; positions of the first two side peaks caused by the Fourier transform are also indicated.

5.4 Distinguishing the strain/temperature peaks from sub-peaks

In health monitoring of civil structures, it is important to distinguish the peaks caused by non-uniform strain/temperature along the fiber from the sub-peaks. Fortunately, for long fibers ($\geq$ 4m), the sub-peaks are buried in noise because the increase of the main peak height is much faster than that of the sub-peaks. In other words, the sub-peak is not a big issue in field tests with long fibers. Fig. 6.2 illustrates such a situation.

Nevertheless, for short fibers, sub-peaks are much more substantial. Here We present a possible way of eliminating the impact of sub-peaks. Since we know sub-peaks are not related

to strain/temperature along the sensing fiber, it is possible to choose the Brillouin spectrum of the fiber under uniform strain/temperature as the reference and subtract it from the newly obtained Brillouin spectrum (with non-uniform strain/temperature) to get rid of the sub-peaks. Fig. 5.17 is such an example. Fig. 5.17(a) shows two normalized Brillouin spectra at the center of a 1m fiber, 1ns pulse with 20dB DC component. The dotted curve represents the case when the whole fiber is loose with a uniform Brillouin frequency 12795 MHz. The solid curve is the spectrum when there is a 3 cm uniformly strained region so that the corresponding Brillouin frequency becomes 12845 MHz. The major difference in these two curves is that the sub-peak around 12845 MHz is higher in the solid case than in the dotted one due to the interaction between the pulse and cw pump at the center of the 3 cm region. Now if the dotted curve is subtracted from the solid curve, the curve in Fig 5.17(b) is then obtained. In this figure, a peak is occurs at 12845MHz representing the strain information in the 3cm region. In any Brillouin spectrum, there is only one peak, which characterizes the real strain/temperature information at the position where the Brillouin spectrum is obtained, from the interaction between the pulse and cw pump, so after subtracting the reference spectrum all peaks from the cross talk between DC component and the cw pump become zero or buried in the fluctuations, so that only one significant peak remains. Therefore, the remaining main peak is the one due to real strain/temperature at that position of the fiber.

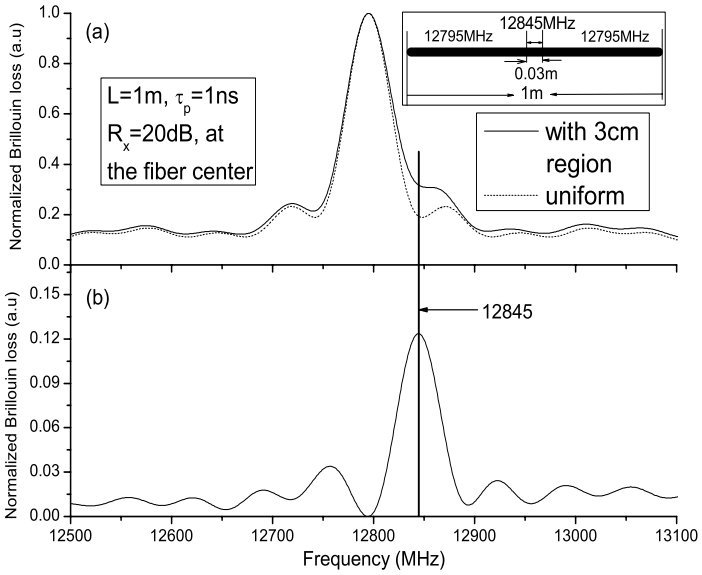

Figure 5.17: (a) Brillouin spectra at the center of a 1m fiber for 1ns pulse with 20dB DC component respectively when the fiber is loose with $\nu_B = 12795$MHz and when it has a 3cm strained region with $\nu_B = 12845$MHz. (b) The spectrum obtained by subtracting the spectrum in the loose case from that in the strained case. Tiny ripples in (b) are fluctuations.

Chapter 6

Impact of the optical phase on the distributed Brillouin sensor

The pump-probe based distributed Brillouin sensors have been extensively studied over the past decade, because this system provides such enhanced sensitivity to strain and temperature combined with significant advantages in sensing length and spatial resolution (a few meters) that no other type of distributed sensor can compete [22, 23, 26]. Although Further improvements in spatial resolution can be achieved by using a short pulse, the Brillouin loss spectrum is broadened and the amplitude of the spectral density decreases significantly when the pulse width decreases below the phonon lifetime of about 10ns. Since this makes measurement of Brillouin frequency shifts difficult, a 1 m spatial resolution was regarded as a limit[22, 23]. Recently, we have demonstrated centimeter spatial resolution combined with 10-20$\mu\varepsilon$ resolution with a Brillouin loss system on a pipeline structures and optical ground wires[20, 21]. However, little work has been done to the theoretical study of the Brillouin loss/gain spectrum shape and line width at centimeter spatial resolution, and prediction of the minimum detectable strain/temperature length. In this chapter, phase modulation (PM) is taken into account in the power and phase imbalance between two arms of an electro-optic modulator (EOM) for the probe signals consisting of the pulse and a DC component in the Brillouin loss spectrum using three coupled wave equations for the phonon and photon fields. For ideal amplitude modulation (AM), the power ratio between the two arms of an interferometer is 100%. However,

in real devices, a ratio between 95-98% can only be achieved due to power imbalance. As a result, it gives combined AM and PM. Due to this feature, the Brillouin loss spectrum is Lorentzian dominated in shape, and the Brillouin spectrum does not change much between the 20th order super Gaussian and pure Gaussian pulses. The broad background is suppressed with increased sensing length. This feature is important in detecting multiple Brillouin peaks with low power density due to the short stress/temperature length (< spatial resolution). Therefore, the minimum detectable stress/temperature length can be reduced to 1/3 of the spatial resolution, i.e. a 3cm strain length for a 1ns pulse width.

6.1 Impact of the optical phase on the Brillouin loss spectrum

According to the extinction ratio defined in Eq. (3.6), Fig. 6.1 shows the parametric relation between $\Delta\phi$ and A_2/A_1 ($\tan\theta$) at R_x values of 15, 20 and 28.8dB. As we see at $A_2/A_1 = 0.95$, $(R_x)_{\max} = 28.8$dB. If we want to get a high extinction ration, $\Delta\phi$ should be around 0 and A_2/A_1 should be around 1, corresponding to $\theta = \pi/4$. When $A_2 = A_1$, the EOM operates as AM. If $A_1 \neq A_2$, the EOM provides combined AM and PM, which is the common case for a push-pull Mach Zehnder based EOMs. Hence, we must consider PM in our Brillouin loss spectrum. In this case η in Eq. (3.3) is set to 0.5 since η has a similar but much weaker effect (this will be explained in the next section) than that of A_2/A_1.

Fig. 6.2 shows the Brillouin spectrum for a 1m (Fig. 6.2(a)) and 4m (Fig. 6.2(b)) fiber at $A_2/A_1 = 0.95$ with 1.5ns pulse length, for $R_x = 15$ and 20dB and a zero DC component which is achieved when $A_2 = A_1$. Because of the DC and pulse combination in the probe, the Brillouin loss spectrum has two parts: the narrow Lorentzian part on the top and a broadened Lorentzian like form (convolution of the pulse and Lorentzian spectrum) as background. When the fiber length is increased, the sub-peaks are suppressed significantly and the Brillouin loss spectrum is dominated by a narrow Lorentzian, even for 1-2ns pulses. Note that the DC component is very important, as the Brillouin loss spectrum without the DC component gives the lowest power density over a broad frequency range. This corresponds to poor SNR, poor strain/temperature

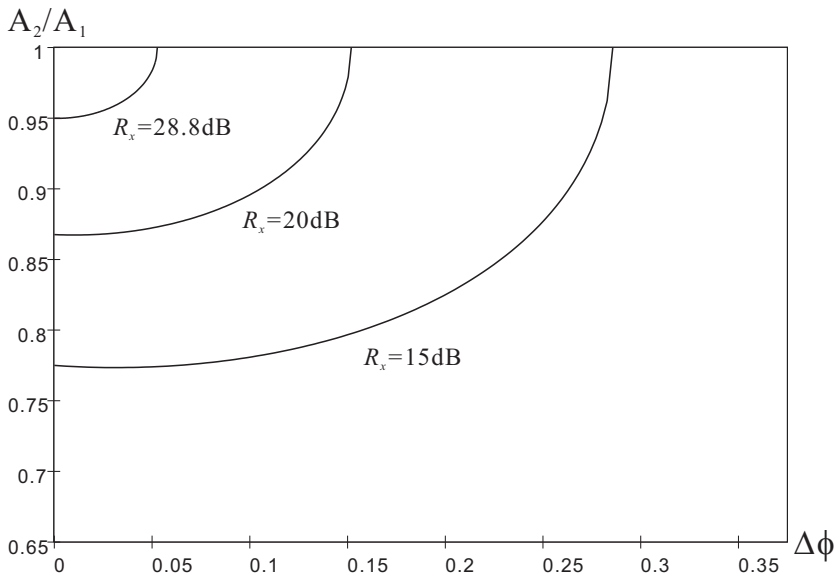

Figure 6.1: Equal extinction ratio curves for the relation between A_2/A_1 and $\Delta\phi$

accuracy and spatial resolution. Another feature of the DC component of the probe signal is that the broad background spectrum varies with R_x for the same pulse width, not as commonly believed to represent the pulse contribution only. The same rule applies to the top part of the spectrum (above the spectrum without DC); this part also includes pulse information. The reason is that the DC component makes the phonon field coherent instead of random. This means we can detect the small Lorentzian peak to find short temperature/strain lengths instead of fitting the peak of the broad background spectrum.

There are a few sub-peaks located on both sides of the main Brillouin peak, but with different heights. If $A_2 = A_1$, those peaks will have equal height. The location of these peaks is not affected by the ratio of A_2/A_1. As demonstrated in Chapter 5, these sub-peaks are caused by off-resonance oscillations between pump and probe signals and the spectrum convolution of the pulse and Lorentzian. The height of the sub-peaks is lower at longer fiber lengths.

Fig. 6.3 is a comparison between super-Gaussian and Gaussian pulses for the Brillouin loss spectrum at $R_x = 20$dB and $A_2/A_1 = 0.95$. The Brillouin loss spectrum for a super Gaussian pulse has a lower power level around the main peak, but high power level at the edges, while for a Gaussian pulses it has a lower power level at the edges and a higher power level around the

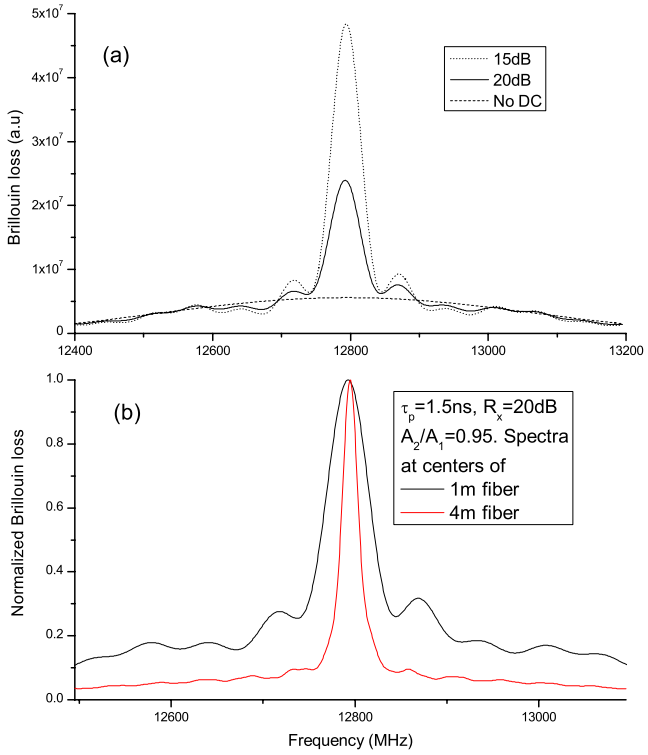

Figure 6.2: (a) Brillouin spectra at the center of a 1m fiber for a 1.5ns pulse with respectively 15, 20 and ∞ extinction ratios. (b) Brillouin spectra at the centers of a 1m and a 4m fiber for a 1.5ns pulse and $R_x = 20$dB.

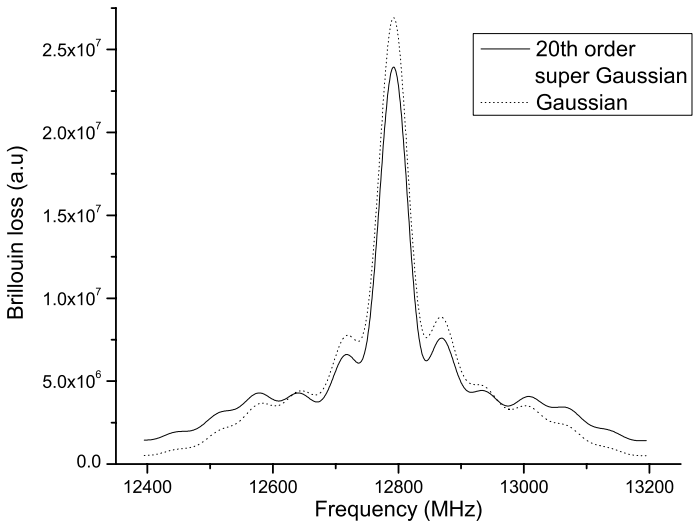

Figure 6.3: Brillouin spectra at the center of a 1m fiber for $\tau_p = 1.5$ns with $R_x = 20$dB in the shapes of Gaussian and 20th order super Gaussian.

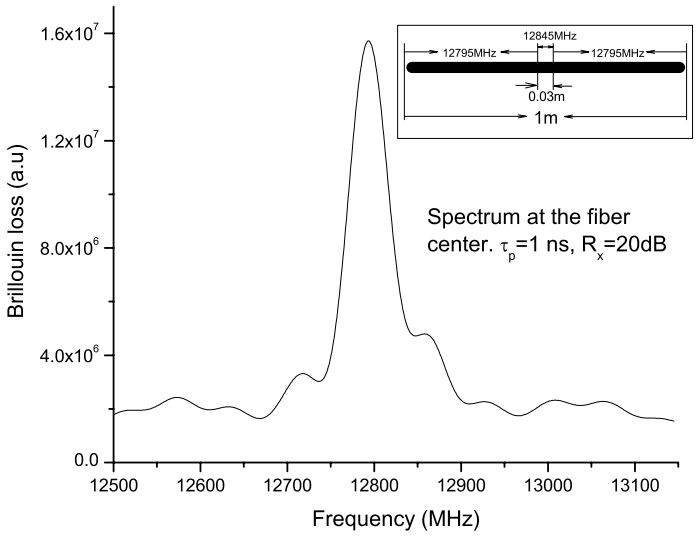

Figure 6.4: Brillouin spectrum taken at the center of a 1m fiber with a frequency shifted (˜50MHz) region of 3cm in the middle.

main peaks. This results in a difficulty in identifying small stress/temperature spots near the stress free fibers or around a room temperature conditions. Apparently, super Gaussian pulse shapes work better for multi-Brillouin peak detection due to better suppression of the broad background spectrum. To prove this point, we calculated the Brillouin loss spectrum for 3cm stress/temperature lengths with a frequency shift of ˜50MHz relative to a loose fiber as shown in Fig. 6.4. The spectrum is observed at the middle of the 3cm, located in the middle of a 1m fiber. In the experiment we can run the reference spectrum (no stress and room temperature) as background and subtract the Brillouin spectrum at varying temperature/strains from the reference, so that the sub-peak impact can be reduced. In this way (as shown in Section 5.4) we can get multi-peak detection at very small stress levels and even shorter fiber lengths.

Fig. 6.5 is the experimental result for the Brillouin spectrum in comparison to the calculated Brillouin spectrum as shown in Fig.6.2(a) at the same condition. The shape and bandwidth (fitted with a Lorentzian spectrum) match very well (except the sub-peaks) between the two figures: FWHM of 46, 58, and 952 MHz for R_x = 15dB, 20 dB and zero DC component for Fig. 6.2 with 46 and 56 MHz for R_x = 15 and 20 dB for Fig. 6.5.

In conclusion, a combination of AM and PM of the probe signal for Brillouin loss/gain

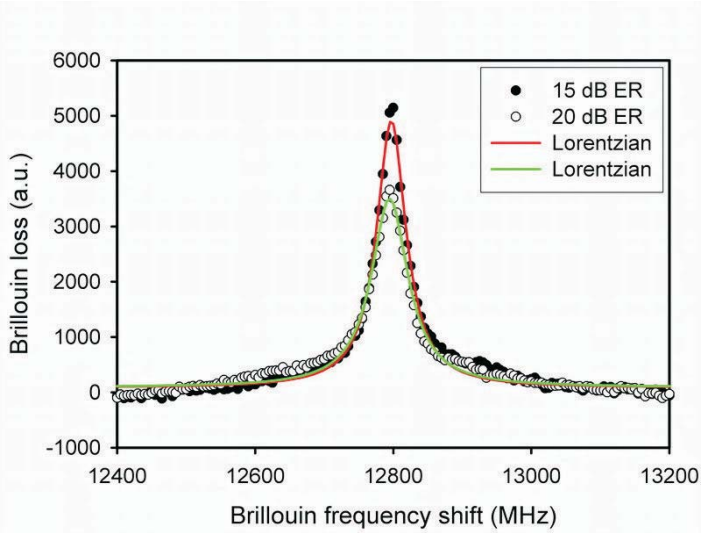

Figure 6.5: Experimentally obtained Brillouin spectra at the center of a 2m fiber for $\tau_p = 1.5$ns, and $R_x = 15$dB and 20dB.

spectra is proposed for the first time. The interaction between pulse/DC and pump contributes to both the top Lorentzian part and the broad background in the Brillouin loss spectrum. By fitting the multiple Brillouin peaks we can identify a small temperature/stress length of 1/3 of pulse length. This explains our enhanced performance of the Brillouin gain/loss based distributed sensor in cm spatial resolution results, combined with high strain/temperature resolution.

6.2 Asymmetric Brillouin spectra and resonance frequency shift

Recall that in Chapter 5, all the simulated Brillouin profiles are symmetric, while those in the last section are not as seen in Fig. 6.2. Furthermore, the resonance frequency is shifted a little as seen in the figures of the last section. The reason is that A_2/A_1 was set to 1 in Chapter 5 but 0.95 in the last section. The power imbalance ($A_2/A_1 \neq 1$) in the two arms of the EOM, which is true in reality, introduces PM together with the AM. This PM has an impact on the Brillouin spectra. Actually, the imbalance of the voltage induced phase between the two arms,

i.e. η, also has impact when it is not equal to 0.5. This phenomenon is very important in field tests of strain/temperature on civil structures, since a shift of the resonance frequency will make the real strain/temperature information to be over or under estimated.

6.2.1 Impact from $A_2/A_1 \neq 1$: the power imbalance

To see the impact only from A_2/A_1, η in Eq. (3.3) is set to 0.5; and we first assume $A_2/A_1 \leq 1$ ($\theta \leq \pi/4$); hence we have

$$\begin{aligned} E_{\text{out}} &= A_{\text{out}} \left[\cos\theta \mathrm{e}^{\mathrm{i}\phi(t)/2} + \sin\theta \mathrm{e}^{-\mathrm{i}\phi(t)/2}\right] \\ &= A_{\text{out}} \left[\sin\theta \mathrm{e}^{\mathrm{i}\phi(t)/2} + \sin\theta \mathrm{e}^{-\mathrm{i}\phi(t)/2} + (\cos\theta - \sin\theta)\, \mathrm{e}^{\mathrm{i}\phi(t)/2}\right] \\ &= A_{\text{out}} \left[2\sin\theta\cos\frac{\phi(t)}{2} + \sqrt{2}\cos\left(\theta + \frac{\pi}{4}\right) \mathrm{e}^{\mathrm{i}\phi(t)/2}\right]. \end{aligned} \tag{6.1}$$

Clearly the first term in the parenthesis of the above equation denotes the AM, while the second term denotes the simultaneous PM. Since θ is very close to $\pi/4$, the PM part is small. Substituting Eq. (6.1) into Eq. (5.1) yields

$$\begin{aligned} \bar{Q}(0,t) &= \frac{1}{2}\Gamma_1 g_B \mathrm{e}^{-\Gamma t} A_{\text{out}} \left\{2\sin\theta \int_0^t E_p(0,t')\cos\frac{\phi(t')}{2}\mathrm{e}^{\Gamma t'}\mathrm{d}t' \right. \\ &\quad \left. + \sqrt{2}\cos\left(\theta + \frac{\pi}{4}\right) \int_0^t E_p(0,t')\mathrm{e}^{\Gamma t' - \mathrm{i}\phi(t')/2}\mathrm{d}t'\right\} \\ &= \frac{1}{2}\Gamma_1 g_B \mathrm{e}^{-\Gamma t} A_{\text{out}} \left\{2\sin\theta \int_0^t E_p(0,t')\cos\frac{\phi(t')}{2}\mathrm{e}^{\Gamma t'}\mathrm{d}t' \right. \\ &\quad \left. - \sqrt{2}\cos\left(\theta + \frac{\pi}{4}\right) \mathrm{e}^{-\mathrm{i}\Delta\phi/2} \int_0^t E_p(0,t')\mathrm{e}^{\Gamma_1 t'}\mathrm{e}^{\mathrm{i}[2\pi(\nu-\nu_B)t' - \pi f(t',t_0,\tau_p)/4]}\mathrm{d}t'\right\} \end{aligned} \tag{6.2}$$

The last line in Eq. (6.2) is obtained by recognizing that $\phi(t) = \pi + \Delta\phi + \pi f(t, t_0, \tau_p)/2$ as defined in Section 3.2.2. The first integral in Eq. (6.2) is resonant when $\nu = \nu_B$ but the second integral is not. In the second integral, with $f(t', t_0, \tau_p) \geq 0$, the oscillation term does not vanish when $\nu = \nu_B$ but when

$$\nu - \nu_B = \frac{1}{8t'} f(t', t_0, \tau_p).$$

Furthermore, the time t where the Brillouin spectrum is taken is always the center of the pulse, i.e. $f(t, t_0, \tau_p) = 1$; hence the above equation becomes

$$\nu - \nu_B = \frac{1}{8t} \tag{6.3}$$

which is a function of t only, with t varying from t_0 to $t_0 + 2Ln/c$. Taking a 1m fiber for a 1.5ns pulse width, 20dB DC component and $A_2/A_1 = 0.95$ as an example, then $t_0 = 15$ns. We now choose $t = 20$ns, which is about the center of the fiber, so that $\nu - \nu_B = 6.25$MHz. Fig. 6.6(a) shows that there is indeed a central frequency shift when $A_2/A_1 = 0.95$. However, it is not 6.25MHz but 3MHz. This is because the first integral in Eq. (6.2) is still resonant when $\nu = \nu_B$. The final resonance frequency is a weighted average of the two resonance frequencies; but the weight of the second integral is small since $\cos\left(\theta + \frac{\pi}{4}\right)$ is very small when $A_2/A_1 = 0.95$. Therefore, the final average cannot reach 6.25MHz. If a smaller value of A_2/A_1 is chosen, say 0.87 (to keep $R_x = 20$dB), $\cos\left(\theta + \frac{\pi}{4}\right)$ is then greater and will result in a shift closer to 6.25MHz. This is verified in Fig. 6.6(b), which shows a 5.5MHz frequency shift.

The asymmetric spectra in Figs. 6.6 also originate from the phase chirp introduced when $A_2 \neq A_1$. This asymmetry depends on time as well. For example, Fig. 6.6 shows that at $t = 20$ ns the sub-peaks on the lower frequency ($< \nu_B$) side are higher than those on the higher frequency side, while Fig. 6.7 illustrates the opposite Besides, the resonance frequency shift is 4MHz in Fig. 6.7, which is greater than that at $t = 20$ns due to Eq. 6.3. As discussed in Section 5.4, since the impact of the sub-peaks can almost be eliminated, the asymmetry of the sub-peaks is not a serious problem in reconstructing the strain/temperature information.

The previous discussion assumed that $A_2/A_1 \leq 1$. If $A_2/A_1 \geq 1$ and $\sin\theta \geq \cos\theta$, then Eq. (6.1) can be rewritten as

$$\begin{aligned} E_{\text{out}} &= A_{\text{out}}\left[\cos\theta \mathrm{e}^{\mathrm{i}\phi(t)/2} + \sin\theta \mathrm{e}^{-\mathrm{i}\phi(t)/2}\right] \\ &= A_{\text{out}}\left[\cos\theta \mathrm{e}^{\mathrm{i}\phi(t)/2} + \cos\theta \mathrm{e}^{-\mathrm{i}\phi(t)/2} + (\sin\theta - \cos\theta)\,\mathrm{e}^{-\mathrm{i}\phi(t)/2}\right] \\ &= A_{\text{out}}\left[2\cos\theta\cos\frac{\phi(t)}{2} + \sqrt{2}\sin\left(\theta - \frac{\pi}{4}\right)\mathrm{e}^{-\mathrm{i}\phi(t)/2}\right]. \end{aligned} \tag{6.4}$$

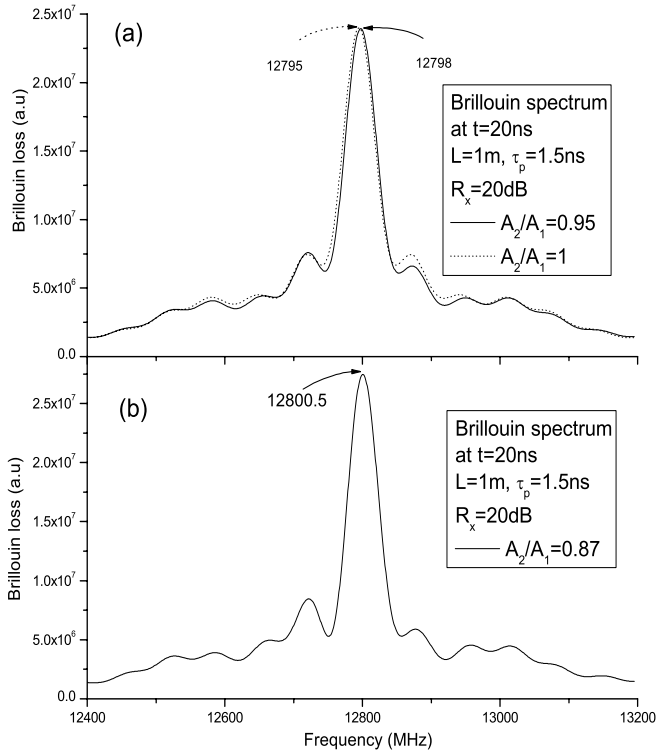

Figure 6.6: (a) Brillouin spectra taken at 20ns when $A_2/A_1 = 0.95$ and 1 for a 1m fiber with $\tau_p = 1.5$ns and $R_x = 20$dB. (b) Brillouin spectrum taken at 20ns for the same fiber and pulse parameters but when $A_2/A_1 = 0.87$.

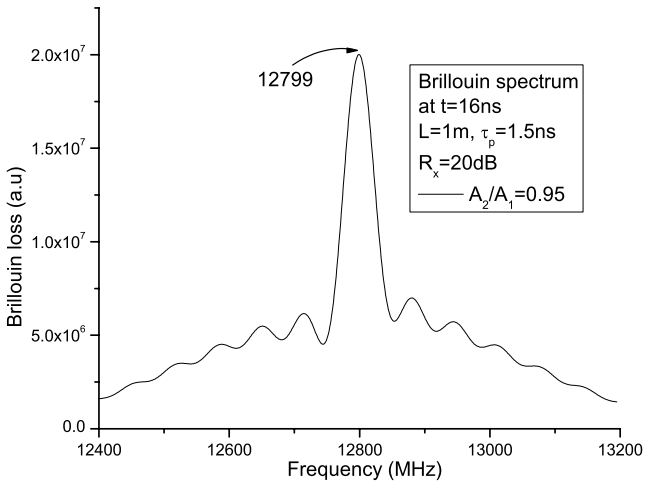

Figure 6.7: Brillouin spectrum taken at 16ns for the same fiber and pulse parameters as above and $A_2/A_1 = 0.95$.

Eq. (6.2) becomes

$$\begin{aligned}\bar{Q}\left(0,t\right) &= \frac{1}{2}\Gamma_1 g_B \mathrm{e}^{-\Gamma t} A_{\mathrm{out}} \left\{ 2\cos\theta \int_0^t E_p(0,t') \cos\frac{\phi\left(t'\right)}{2} \mathrm{e}^{\Gamma t'} \mathrm{d}t' \right. \\ &\left. \mathrm{i}\sqrt{2}\sin\left(\theta - \frac{\pi}{4}\right) \mathrm{e}^{\mathrm{i}\Delta\phi/2} \int_0^t E_p(0,t') \mathrm{e}^{\Gamma_1 t'} \mathrm{e}^{\mathrm{i}[2\pi(\nu-\nu_B)t' + \pi f(t',t_0,\tau_p)/4]} \mathrm{d}t' \right\}.\end{aligned}$$

By the same argument as in the case when $A_2/A_1 \leq 1$, it is apparent that the resonance of the second integral in the above equation occurs when $\nu < \nu_B$, i.e., when $\nu_B - \nu = 1/8t$. Fig. 6.8 illustrates such a situation.

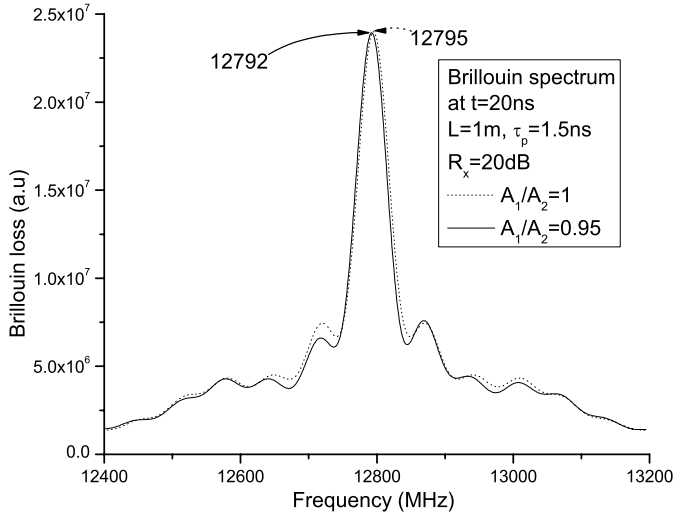

Figure 6.8: Brillouin spectra at 20ns when $A_1/A_2 = 0.95$ and 1.0 for the same fiber and pulse parameters as above.

6.2.2 Impact of $\eta \neq 0.5$: the phase imbalance

Unbalanced amplitudes are not the only factor introducing a residual phase to the output pulse of the EOM. As indicated in Eq. (3.3), the parameter η, which denotes the distribution of the induced phases between the two arms of the EOM, results in a residual phase as well when it is not equal to 0.5. To see the impact of η only, A_2/A_1 in Eq. (3.3) is set to 1. Then we have

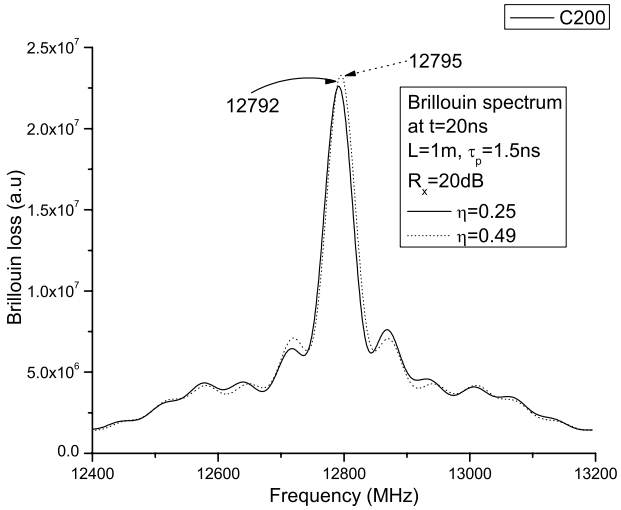

Figure 6.9: Brillouin spectra taken at 20ns when $\eta = 0.25$ and 0.49 for the same fiber and pulse parameters as above.

$$\begin{aligned} E_{\text{out}} &= A_{\text{out}} \left[\cos\theta \mathrm{e}^{\mathrm{i}\eta\phi(t)} + \sin\theta \mathrm{e}^{-\mathrm{i}(1-\eta)\phi(t)}\right] \\ &= A_{\text{out}} \left[\mathrm{e}^{\mathrm{i}\phi(t)/2} + \mathrm{e}^{-\mathrm{i}\phi(t)/2}\right] \mathrm{e}^{\mathrm{i}(2\eta-1)\phi(t)/2} \\ &= 2A_{\text{out}} \cos\frac{\phi\left(t\right)}{2} \mathrm{e}^{\mathrm{i}(2\eta-1)\phi(t)/2}. \end{aligned} \tag{6.5}$$

This is a production of both AM and PM, instead of a summation as in the previous case. Substituting Eq. (6.5) into Eq. (5.1) gives

$$\begin{aligned} \bar{Q}\left(0,t\right) &= \Gamma_1 g_B \mathrm{e}^{-\Gamma t} A_{\text{out}} \int_0^t E_p(0,t') \cos\frac{\phi\left(t'\right)}{2} \mathrm{e}^{\Gamma t'} \mathrm{e}^{-\mathrm{i}(2\eta-1)\phi(t')/2} \mathrm{d}t' \\ &= -\Gamma_1 g_B \mathrm{e}^{-\Gamma t} A_{\text{out}} \mathrm{e}^{\mathrm{i}(2\eta-1)(\pi+\Delta\phi)/2} \times \\ &\quad \int_0^t E_p(0,t') \cos\frac{\phi\left(t'\right)}{2} \mathrm{e}^{\Gamma_1 t'} \mathrm{e}^{\mathrm{i}[2\pi(\nu-\nu_B)t' - (2\eta-1)\pi f(t',t_0,\tau_p)/4]} \mathrm{d}t', \end{aligned} \tag{6.6}$$

which shows that the resonant states depends on η and that the corresponding resonance frequency shifts to the higher frequency side when $0 \leq \eta < 0.5$ and to the lower side when $0.5 < \eta \leq 1$. The shift is described by the following equation:

$$\nu - \nu_B = \frac{2\eta - 1}{8t} \tag{6.7}$$

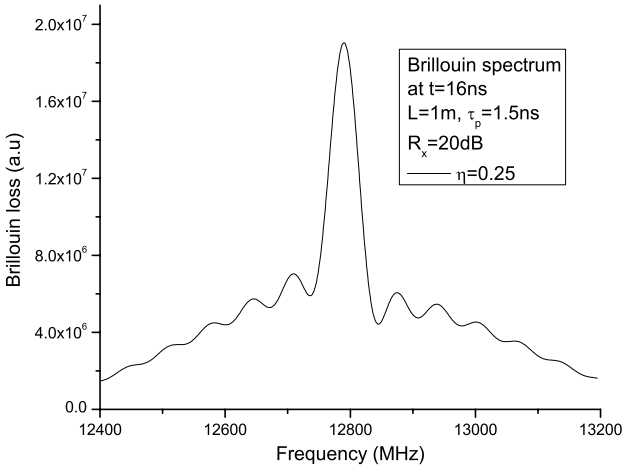

Figure 6.10: Brillouin spectrum taken at 16ns when $\eta = 0.25$ for the same fiber and pulse parameters as above.

Nevertheless, for a push-pull MZ-EOM, $\eta \approx 0.5$ so that $(2\eta - 1) \approx 0$, i.e. the impact of η is much weaker than that of A_2/A_1. For example, when $\eta = 0.49$, $(2\eta - 1) = -0.02$, which is 50 times weaker than when $A_2 \neq A_1$ according to Eq. (6.3). Fig. 6.9 shows that when $\eta = 0.49$ the impact is invisible while when $\eta = 0.25$ the resonance frequency shifts about 3MHz to be 12792MHz according to Eq. (6.7). The asymmetry of the Brillouin spectrum also depends on the time, as shown in Fig. 6.10 by comparing to Fig. 6.9.

In general, when both the unbalanced amplitude and the unbalanced phase distributions are considered, the output field of the EOM is

$$\begin{aligned} E_{\text{out}} &= A_{\text{out}} \left[\cos\theta \mathrm{e}^{\mathrm{i}\eta\phi(t)} + \sin\theta \mathrm{e}^{-\mathrm{i}(1-\eta)\phi(t)}\right] \\ &= A_{\text{out}} \left[\cos\theta \mathrm{e}^{\mathrm{i}\phi(t)/2} + \sin\theta \mathrm{e}^{-\mathrm{i}\phi(t)/2}\right] \mathrm{e}^{\mathrm{i}(2\eta-1)\phi(t)/2} \\ &= A_{\text{out}} \left[2\sin\theta\cos\frac{\phi(t)}{2} + \sqrt{2}\cos\left(\theta + \frac{\pi}{4}\right) \mathrm{e}^{\mathrm{i}\phi(t)/2}\right] \mathrm{e}^{\mathrm{i}(2\eta-1)\phi(t)/2}. \end{aligned}$$

This is a combination of PM and AM by both multiplication and addition. Based on previous discussions, for common push-pull EOM's the unbalanced amplitudes dominates the impact of the residual phase chirp in the Brillouin spectra. The impact of an unbalanced phase distribution between the two arms becomes significant in the case when only one of the two arms of the EOM is modulated.

Chapter 7

Conclusions, Further discussions & future work

7.1 Highlights and originality of my work

Through this thesis, my work can be summarized in the following.

- Adopted and improved a numerical method (introduced by Chu *et al.*[1]) to solve the 3-wave coupled transient model for distributed fiber sensing based on Brillouin loss. Simulated our sensor based on these numeric solutions to study the Brillouin loss spectra obtained in various situations. Improved Chu's numerical method by iteration.

- For the first time, studied the sub-peaks in the Brillouin loss profiles through simulations and an analytical approximation. Demonstrated, for the first time, two origins of the sub-peaks. First predicted the off-resonance oscillation denoting the oscillation of the detected cw pump intensity in time domain when the beat frequency ν of the two counter-propagating laser beams do not match the Brillouin frequency ν_B of the sensing fiber. This type of oscillation as the dominating origin of sub-peaks has the frequency $|\nu - \nu_B|$. The other origin is the Fourier spectrum of the pulsed probe beam. Characterized the sub-peaks in that 1) positions of sub-peaks due to the off-resonance oscillation do not change with the amount of DC component and the pulse width of the pulsed probe beam

but their relative heights do as well as with pulse shape; 2) the positions of the sub-peaks due to the probe Fourier spectrum vary with both pulse width and pulse shape but not with the fiber length and the amount of DC component, while their relative heights change with all these factors; 3) the competition between the two origins becomes substantial for long pulse widths (> 3 ns) by placing the sub-peaks caused by off-resonance oscillation on the top of those caused by the probe Fourier spectrum. Demonstrated a possible way of eliminating the sub-peaks in Brillouin spectrum analysis by subtracting the Brillouin spectrum with new strain/temperature information from the reference Brillouin spectrum obtained for loose fiber and reference temperature.

- For the first time, proposed a model of the pulsed probe field with a time dependent phase (varying from a minimum value to a maximum as the shape of the pulse), and a combination of phase modulation (PM) and amplitude modulation (AM) due to imperfectly balanced field amplitudes and voltage induced phase in the two modulation arms of the EOM. With this model, the calculated Brillouin spectra match well with the experimental spectra. This provides theoretical support for the centimeter spatial resolution with Brillouin loss spectrum bandwidth (˜50MHz) and high SNR (˜37dB) of our sensor. The broad background spectrum varies with R_x for the same pulse width, not as commonly believed to represent the pulse contribution only. The same rule applies to the top part of the spectrum (above the spectrum without DC); this part also includes pulse information. The reason is that the DC makes the phonon field coherent instead of random,.which results in shorter minimum detectable stress/temperature length. Predicted another two possible impacts of the optical phase of the probe beam on the Brillouin profile: an asymmetric Brillouin spectrum and the central Brillouin frequency shift.

- Proposed in the next section several possible future directions in theoretical studies in the distributed fiber sensing based on Brillouin loss.

7.2 Further discussions and future work

In spite of the work that has been done, there are still many interesting points that deserve intensive future study. Here, I present several possibilities.

7.2.1 3-wave transient model including polarization

Distributed fiber sensors based on Brillouin loss are polarization dependent in that the interaction between the two counter-propagating laser beams is maximum when they are polarized in the same direction and minimum when their polarization states are perpendicular. In the most usual cases where single mode fibers are used as the sensing fiber, polarization states of the two counter-propagating laser beams are random along the fibers due to the fluctuations of the fiber birefringence. An average over the polarization effects at each scanned beat frequency must be done. This is why in Figs. 3.1 and **??**, a polarization controller is employed to periodically scramble the polarization state of the cw pump beam. Nevertheless, the 3-wave transient model in Eqs. (2.9) assumes that the two laser beams are already polarized in the same direction. This actually over estimates the interaction. From this point of view, it is very practical to include the polarization states in the 3-wave model. To do so, E_p and E_s in Eqs. (2.9) can be replaced by two vectors $\vec{E}_p = \left(E_{p_x}, E_{p_y}\right)$ and $\vec{E}_s = \left(E_{s_x}, E_{s_y}\right)$ respectively. Although high order polarization mode dispersion (PMD) can be neglected for τ_p of the order of nanoseconds since its value is 0.1 ps/km at 1550 nm and even less at 1310 nm. The effect on the polarization states due to the dependence of birefringence on z should be taken into account. Therefore, the following coupled equations are obtained:

$$\begin{aligned}
\left(\frac{\partial}{\partial z} - \frac{1}{v_g}\frac{\partial}{\partial t} - \frac{1}{2}\alpha + \mathrm{i}\vec{\beta}\left(z\right)\cdot\vec{\sigma}\right)\vec{E}_p &= \bar{Q}\vec{E}_s \\
\left(\frac{\partial}{\partial z} + \frac{1}{v_g}\frac{\partial}{\partial t} + \frac{1}{2}\alpha - \mathrm{i}\vec{\beta}\left(z\right)\cdot\vec{\sigma}\right)\vec{E}_s &= \bar{Q}^*\vec{E}_p \\
\left(\frac{\partial}{\partial t} + \Gamma\right)\bar{Q} &= \frac{1}{2}\Gamma_1 g_B\left(E_{p_x}E_{s_x}^* + E_{p_y}E_{s_y}^*\right),
\end{aligned}$$

where $\mathrm{i}\vec{\beta}\left(z\right)\cdot\vec{\sigma} = \mathrm{i}\sum_{j=x,y,z}\beta_j\sigma_j$ accounts for the change of polarization states. The σ_i's are the 2-D Pauli matrices and $\beta_j\left(z\right)$'s are real valued functions of z for the varying birefringence. For

single mode fibers $i\vec{\beta}(z)\cdot\vec{\sigma}$ is then a random Hermitian traceless matrix[57] and $\left|\vec{\beta}\right| = 1/L_B(z)$, where $L_B(z)$ is the local beat length of the fiber. These equations show that whatever the initial polarization states of the two lasers beams, they become coupled as soon as entering the sensing fiber. Once the polarization states are included, should the effects such as chromatic dispersion (CD) and polarization dependent loss/gain (PDL/G) also be considered? The answer is no for fiber sensing because of the following: 1) the chromatic dispersion length L_D is defined as $\tau_p^2/|\beta_2|$ where τ_p (< 2 ns in sensing) is the pulse width and β_2 is the GVD parameter (0 for 1310 nm and 20 ps^2/km for 1550 nm), so L_D is 50000 km at 1550 nm and ∞ at 1310 nm and are too long to be considered in fiber sensing; 2) PDL/G is significant in optic components but not in fibers.

Simulations can be done based on this new model by randomly or specifically choosing polarization states for the two laser beams and then doing an average on a number of simulations with different initial polarization states. This work is a candidate for future research.

7.2.2 Spatially and temporally correlated initial noise phonon field

Recall that in solving Eqs. (2.9), an initial phonon field originating from thermal noise was introduced as the initial condition in Eq. (4.1). In the present study, this initial phonon field is treated as white noise with Rayleigh distributed random intensity and uniformly distributed random phase as described in Section 4.2.2 , i.e. temporally and spatially uncorrelated since the phonon field is assumed to be non-propagating. Nevertheless, there could be some spatial or/and temporal correlation, since the phonon field does propagate within the phonon life time. Therefore, although the exact correlation function needs more specific study, a possibility can be obtained as in Eq. (7.1) by realizing that it is spatially and temporally short-term correlated.

$$\begin{aligned} C_{\bar{Q}_0}(z-z', t-t') &= \left\langle \bar{Q}_0(z,t)\, \bar{Q}^*(z',t') \right\rangle \\ &= A(\lambda,\tau) \exp\left(-\frac{-|z-z'|}{\lambda} - \frac{|t-t'|}{\tau} \right), \end{aligned} \tag{7.1}$$

where τ is the phonon life time characterizing the correlation time, λ is the correlation length by assuming the spatial correlation decays exponentially as well, $A(\lambda,\tau)$ is a function to be

determined ensuring the correlation function collapses to the common temporal/spatial correlation function when position/time is fixed. Note that the intensity of this noise phonon field is still required to be Rayleigh distributed. This is the key to obtain $A(\lambda, \tau)$.

Future simulations can utilize Eq. (7.1) to study deeper into the impact of the initial noise phonon field. Possible methods of generating such colored noise as in Eq. (7.1) can be referred to Taulsen *et al.*[58], Billah *et al.*[59] and Manella *et al.*[60].

7.2.3 Impact of the time delay on the sub-peaks

In simulations based on the 3-wave model, a time delay t_0 is used as the time when the pulse center enters the sensing fiber. This t_0 is set to be longer than the round trip time of the light along the sensing fiber for two reasons: 1) allow the interaction between DC component and the cw pump beam at $z = L$ to transmit to $z = 0$ so that the simulation becomes steady; 2) in reality, the t_0 is the inverse of the pulse generating repetition rate which cannot be too high since only one pulse is allowed inside the sensing fiber and cannot be too low to increase the measurement time. For example, in simulating a 1m fiber, $t_0 = 15$ns which is longer than the round trip time (9.8 ns). The interesting thing is that, when t_0 is set to 50ns for a 1m fiber, the Brillouin spectrum with sub-peaks has a change as shown in Fig. 7.1. Sub-peaks in the case of $t_0 = 50$ ns are much smaller and compact than those when $t_0 = 15$ns. This can be explained by Eq. (5.7) and discussed in Section 5.3.2. There exist ripples in a wider frequency range, such as the two peak-like shapes around 12600MHz and 13200MHz respectively. They are also found to be caused by the off-resonance oscillation. As indicated by our further study, it seems that the Brillouin spectrum will not change any more when t_0 is greater than some value (˜100 ns for simulation conditions as in shown in Fig. 7.1).

7.2.4 Real time data analysis

So far, the data analysis of the test results from the distributed Brillouin sensors are not done in real time. Strain/temperature information along the sensing fiber is obtained through intensive data processing after the test. A sensing system with real time data analysis is highly desirable, since detecting and hence fixing problems on civil structures promptly are very important.

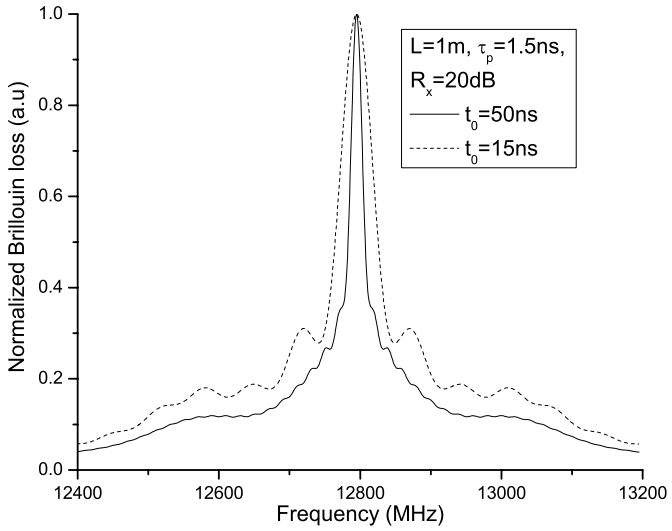

Figure 7.1: Brillouin spectra at the center of a 1m fiber for $\tau_p = 1.5$ns and $R_x = 20$dB when $t_0 = 15$ns and 50ns.

Nevertheless, fulfilling this goal is very difficult in reconstructing the strain/temperature distribution from the Brillouin loss profiles along the sensing fiber since in real situations single-peak Brillouin spectra are uncommon. Instead, multi-peak Brillouin profiles are usually obtained due to 1) the cross talk (via DC component of the pulsed probe beam) effect in non-uniform strained fibers [55], 2) special fibers with complex structures [61, 20] resulting in simultaneous strain and temperature information, and 3) sub-peaks described in Chapter 5. A general peak fitting technique is then highly desirable. To be as close as possible to this goal is an intriguing task.

Bibliography

[1] R. Chu, M. Kanefsky, and J. Falk, "Numerical Study of Transient Stimulated Brillouin Scattering," J. Appl. Phys. **71**, 4653–4658 (1992).

[2] A. W. Brown, "Development of a Brillouin Scattering Based Distributed Fibre Optic Strain Sensor," Ph.D. thesis, The University of New Brunswick (2000).

[3] Hikariai, "Optical Isolators," http://www.fdk.co.jp/laboratory/hikariai-e.html.

[4] H. D. Simonsen, R. Paetsch, and J. R. Dunphy, in *Proc. 1st European Conf. On Smart Structures and Materials*, B. Culshaw, P. T. Gardiner, and A. MacDonach, eds., p. 73 (Institute of Physics, Bristol, 1992).

[5] T. Liu, G. F. Fernando, Y. J. Rao, D. A. Jackson, L. Zhang, and I. Bennion, in *Proc. SPIE, Vol. 2895*, p. 249 (SPIE-The International Society for Optical Engineering, Bellingham, WA, 1996, 1996).

[6] F. M. Haran, J. K. Rew, and P. D. Foote, in *Proc. SPIE, Vol. 3330*, p. 220 (SPIE-The International Society for Optical Engineering, Bellingham, WA, 1998).

[7] R. L. Idriss, M. B. Kodindouma, A. D. Kersey, and M. A. Davis, "Multiplexed Bragg Grating Optical Fiber Sensors for Damage Evaluation in Highway Bridges," Smart Mater Structure **7**, 209–216 (1998).

[8] B. P. Arjyal, C. Galiotis, S. L. Ogin, and R. D. Whattingham, J. Mater. Sci. **33**, 2745 (1998).

[9] T. Horiguchi and M. Tateda, "Optical-Fiber-Attenuation Investigation Using Stimulated Brillouin Scattering Between a Pulse and a Continuous Wave," Optics Letters **14**, 408–410 (1989).

[10] T. Kurashima, T. Horiguchi, and M. Tateda, "Thermal Effects on the Brillouin Frequency Shift in Jacketed Optical Silica Fibers," Applied Optics **29**, 2219–2222 (1990).

[11] X. Bao, D. J. Webb, and D. A. Jackson, "32-Km Distributed Temperature Sensor Based on Brillouin Loss In an Optical Fiber," Optics Letters **18**(18), 1561 (1993).

[12] T. R. Parker, M. Farhadiroushan, V. A. Handerek, and A. J. Rogers, "Temperature and Strain Dependance of the Power Level and Frequency of Spontaneous Brillouin Scattering in Optical Fibers," Optics Letters **22**, 787–789 (1997).

[13] "SHM System Specifications," Product specifications (2004).

[14] W. Du, X. Tao, and H.-Y. Tam, "Fiber Bragg Grating Cavity Sensor for Simultaneous Measurement of Strain and Temperature," IEEE Photonics Technology Letters **11**(1), 105 (1999).

[15] M. K. Barnoski and S. M. Jensen, "Fiber Waeguides: A Novel Technique for Investigating Attenuation Characteristics," Appl. Opt. **15**(9), 2112–2115 (1976).

[16] T. R. Parker, M. Farhadiroushan, V. A. Handerek, and A. J. Rogers, "A Fully Distributed Simultaneous Strain and Temperature Sensor Using Spontaneous Brillouin Backscatter," IEEE Photon. Technol. **9**(7), 979 (1997).

[17] T. Kurashima, T. Horiguchi, and M. Tateda, "Distributed-Temperature Sensing Using Stimulated Brillouin Scattering in Optical Silica Fibers," Optics Letters **15**, 1038–1040 (1990).

[18] X. Bao, D. J. Webb, and D. A. Jackson, "22-Km Distributed Temperature Sensor Using Brillouin Gain in an Optical Fiber," Optics Letters **18**, 552–554 (1993).

[19] X. Bao, D. J. Webb, and D. A. Jackson, "32-Km Distributed Temperature Sensor Based on Brillouin Loss in an Optical Fiber," Optics Letters **18**, 1561–1563 (1993).

[20] L. Zou, G. A. Ferrier, S. Afshaarvahid, Q. Yu, L. Chen, and X. Bao, "Distributed Brillouin Scattering Sensor for Discrimination of Wall Thinning Defects in Steel Pipe under Internal Pressure," Appl. Optics **43**, 1583 (2004).

[21] L. Zou, F. Ravet, L. Chen, and X. Bao, "Distributed Brillouin Scattering Sensor for Structural Healthy Monitoring of Optical Ground Wire," (SPIE, 2004).

[22] A. Fellay, L. Thévenaz, M. Facchini, M. Niklès, and P. Robert, "Distributed Sensing Using Stimulated Brillouin Scattering: Towards Ultimate Resolution," OSA Technical Digest Series **16**, 324–327 (1997).

[23] T. Horiguchi, K. Shimizu, T. Kurashima, M. Tateda, and Y. Koyamada, "Development of a Distributed Sensing Technique Using Brillouin Scattering," J. Lightwave Technol. **13**(7), 1296 (1995).

[24] T. Horiguchi, T. Kurashima, and M. Tateda, "Tensile Strain Dependence of Brillouin Frequency Shift in Silica Optical Fibers," IEEE Photonics Technology Letters **1**, 107–108 (1989).

[25] T. Horiguchi and M. Tateda, "BOTDA-Nondestructive Measurement of Single-Mode Optical Fiber Attenuation Characteristics Using Brillouin Interaction: Theory," J. Lightwave Technol. **7**(8), 1170–1176 (1989).

[26] X. Bao, J. Dhliwayo, N. Heron, D. J. Webb, and D. A. Jackson, "Experimental and Theoretical Studies on a Distributed Temperature Sensor Based on Brillouin Scattering," J. of Lightwave Technol. **13**, 1340 (1995).

[27] G. P. Agrawal, *Nonlinear Fiber Optics*, 3rd ed. (Academic Press, San Diego, California, USA, 2001).

[28] A. C. Newell and J. V. Moloney, *Nonlinear Optics* (Addison Wesley, 1992).

[29] C. D. Cantrell, "Nonlinear Optics," Lecture notes (1999).

[30] R. W. Boyd, *Nonlinear Optics* (Academic Press, San Diego, California 92101-4495, 1992).

[31] Corning, "SMF-28 CPC6 Single-Mode Optical Fiber Product Information," Tech. rep., Corning Inc., N. Y. (1998).

[32] J. Smith, "Characterization of the Brillouin Loss Spectrum for Simultaneous Distributed Sensing of Strain and Temperature," Master's thesis, The University of New Brunswick (1999).

[33] D. Culverhouse, F. Farahi, C. N. Pannell, and D. A. Jackson, "Potential of Stimulated Brillouin Scattering as Sensing Mechanism for Distributed Temperature Sensors," Electronics Letters **25**, 913–915 (1989).

[34] R. G. Smith, "Optical Power Handling Capacity of Low Loss Optical Fibres as Determined by Stimulated Raman and Brillouin Scattering," Appl. Opt. **11**, 2489–2494 (1972).

[35] G. P. Agrawal, *Fiber-Optic Communication Systems*, 3rd ed. (Wiley Inter-Science, 2002).

[36] N. A. Olsson and J. P. V. der Ziel, "Cancellation of Fiber Los by Semiconductor Laser Pumped Brillouin Amplification at 1.5 Um," Phys. Lett. **48**(20), 1329–1330 (1986).

[37] G. C. Valley, "A Review of Stimulated Brillouin Scattering Excited with a Broad-Band Pump Laser," IEEE Journal of Quantum Electronics **22**, 704–705 (1986).

[38] H. Li and K. Ogusu, "Dynamic Behavior of Stimulated Brillouin Scattering in a Single-Mode Optical Fiber," Jpn. J. Appl. Physics **38**(11), 6309–6315 (1999).

[39] C. C. Chow and A. Bers, "Chaotic Stimulated Brillouin Scattering in a Finite-Length Medium," Physical Review A **47**(6), 5144 (1993).

[40] V. Lecoeuche, S. Randoux, B. Segard, and J. Zemmouri, "Dynamics of a Brillouin Fiber Ring Laser: Off-Resonant Case," Physical Review A **53**(4), 2822 (1996).

[41] S. Rae, I. Bennion, and M. J. Cardwell, "New Numerical Model of Stimulated Brillouin Scattering in Optical Fibres with Nonuniformity," Optics Communications **123**, 611–616 (1996).

[42] W. Lu, A. Johnstone, and R. G. Harrison, "Deterministic Dynamics of Stimulated Scattering Phenomena with External Feedback," Physical Review A **46**(7), 4114 (1992).

[43] L. Chen and X. Bao, "Analytical and Numerical Solutions for Steady State Stimulated Brillouin Scattering in a Single-Mode Fiber," Optics Communications **152**, 65–70 (1998).

[44] G. D. VanWiggeren and R. Roy, "Transmission of Linearly Polarized Light Through a Single-Mode Fiber with Random Fluctuations of Birefringence," Applied Optics **38**(18), 3888 (1999).

[45] G. L. Li and P. K. L. Yu, "Optical Intensity Modulators for Digital and Analog Applications," Journal of Lightwave Technology **21**(9), 2010–2030 (2003).

[46] A. Yariv, *Optical Electronics in Modern Communications* (Oxfor, 198 Madison Ave., New York, NY 10016-4314, 1997).

[47] S. Cheng and Z. Wang, eds., *General Physics*, vol. 3, 5th ed. (Higher Education (China), 1999).

[48] T. Mizumoto, H. Yokoi, and N. Shinjo, "Wafe Bonding and its Application to Integrated Optical Isolator," (2000).

[49] C. A. Hall and T. A. Porshing, *Numerical Analysis of Partial Differential Equations* (Prentice Hall, Englewood Cliffs, NJ, 1990).

[50] J. W. Thomas, *Numerical Partial Differential Equations: Finite Difference Methods* (Springer-Verlag, 1995).

[51] B. Oliver, "Thermal and Quantum Noise," in *Proc. IRE.*, vol. 53, pp. 53: 436–454 (Institute Of Radio Engineers, 1965).

[52] M. Gupta, *Electrical Noise: Fundamentals and Sources* (IEEE Press, 1977).

[53] W. H. Press, B. P. Flannery, S. A. Teukolsky, and W. T. Vetterling, *Numerical Recipes in* (Cambridge University Press, 1988).

[54] X. Bao, D. J. Webb, and D. A. Jackson, "Temperature Non-Uniformity in Distributed Temperature Sensors," Electron. Letters **29**(11), 976 (1993).

[55] S. A. V., G. A. Ferrier, X. Bao, and L. Chen, "Effect of the Finite Extinction Ratio of an Electro-Optic Modulator on the Performance of Distributed Probe-Pump Brillouin Sensor Systems," Optics Letters **28**(16), 1418–1420 (2003).

[56] R. W. Boyd, K. Rzazewski, and P. Narum, "Noise Initiation of Stimulated Brillouin Scattering," Phys. Rev. A **42**, 5514–5521 (1990).

[57] Y. Chung, V. V. Lebedev, and S. S. Vergeles, "Interaction of Solitons Through Radiation in Optical Fibers with Randomly Varying Birefringence," Optics Letters **29**(11), 1245 (2004).

[58] A. Traulsen, K. Lippert, and U. Behn, "Generation of Spatiotemporal Correlated Noise in 1+1 Dimensions," Phys. Rev. E **69**(026116), 1–9 (2004).

[59] K. Y. R. Billah and M. Shinozuka, "Numerical Method for Colored-Noise Generation and its Application to a Bistable System," Phys. Rev. A **42**(12), 7492 (1990).

[60] R. Mannella and V. Palleschi, "Comment on "Numerical Method for Colored-Noise Generation and its Application to a Bistable System"," Phys. Rev. A **46**(12), 8028 (1992).

[61] C. Lee, P. Chiang, and S. Chi, "Utilization of a Dispersion-Shift Fiber for Simultaneous Measurement of Distributed Strain and Temperature Through Brillouin Frequency Shift," IEEE Photonics Technol. Lett. **13**, 1094 (2001).

Appendix A

Curriculum Vitae, publications and conferences

A.1 Curriculum Vitae

- M.Sc. at Engineering (majored in Computer Science), University of Pennsylvania, received in 2002.
- B. Engineering (majored in Computer Science), South China University of Technology, received in 1998.
- B. Economics (majored in International Trade), South China University of Technology, received in 1998.

A.2 Refereed Publications

- **Yidun Wan**, Shahraam Afshar Vahid, Lufan Zou, Liang Chen and Xiaoyi Bao, "Sub-peaks in Brillouin Loss Spectra of the Distributed Fiber-Optic Sensors", Optics Letters, Vol. 30 Issue 10 Page 1099, May 2005.
- Xiaoyi Bao, **Yidun Wan**, Lufan Zou and Liang Chen, "Impact of the Optical Phase on the Distributed Brillouin Fiber Sensor at Centimeter Spatial Resolution", Optics Letters,

Vol. 30 Issue 8 Page 827, April 2005.

- Lufan Zou, Xiaoyi Bao, **Yidun Wan** and Liang Chen, "Coherent Probe-Pump based Brillouin Sensor for centimeter crack detection", Volume 30, Issue 4, pp. 370-372, February 2005.

A.3 Conference Papers and Presentations

- **Yidun Wan**, Shahraam Afshar Vahid, Lufan Zou, Liang Chen and Xiaoyi Bao, "Simulation of distributed optical fiber probe-pump Brillouin sensor", Photonics North 2004, Ottawa, Canada, part of Proceedings of SPIE vol. 5579.

- Ou Chen, **Yidun Wan**, Lufan Zou, Guilin Wu, Dan Falk, Liang Chen and Xiaoyi Bao, ""Development of the Offset Locking Based Distributed Sensor", Photonics North 2004, Ottawa, Canada, part of Proceedings of SPIE vol. 5579.

- Lufan Zou, **Yidun Wan**, Xiao Bao and Liang Chen, "Centimeter Spatial Resolution of Distributed Optical Fiber Sensor For Structural Healthy Monitoring", Photonics North 2004, Ottawa, Canada, part of Proceedings of SPIE vol. 5579.

- Xiaoyi Bao, **Yidun Wan**, Lufan Zou, and Liang Chen, "The effect of optical phase on the Brillouin spectrum in the distributed sensor system", OFS-17 conference, accepted, December 2004

- **Yidun Wan**, oral presentation: "A New Low Cost Distributed Fiber-Optic Sensing System based on two 1550 nm DFB Lasers", 9^{th} Annual Conference of ISIS Canada, Halifax, Canada, April 2004.

- **Yidun Wan**, oral presentation: "Simulation of distributed optical fiber probe-pump Brillouin sensor", Photonics North 2004, Ottawa, Canada.

A.4 Posters

- **Yidun Wan**, Ou Chen, Qinrong Yu, Shahraam Afshar and Xiaoyi Bao, "A Distributed Fiber Optics Sensor System for Health Monitoring", 9^{th} Annual Conference of ISIS Canada, Halifax, Canada, April 2004.